Physik Department

Modeling the Allosteric Mechanism of Spastin

Dissertation

von

Doan Tuong-Van Le

München 2013

Technische Universität München

TECHNISCHE UNIVERSITÄT MÜNCHEN

Lehrstuhl für Biophysik E22

Modeling the Allosteric Mechanism of Spastin

Doan Tuong-Van Le

Für meine Eltern

Contents

List of Figures

List of Tables

Zusammenfassung

Spastin, ein ubiquitär exprimiertes AAA-Protein, schneidet Mikrotubuli unter Verwendung der aus ATP-Hydrolyse gewonnenen Energie. Mutationen im Genom *SPAST* (oder *SPG4*), welches Spastin kodiert, sind die häufigsten Gründe für die neurodegenerative Erbkrankheit HSP. Patienten sind bezüglich des Genes heterozygot und exprimieren sowohl defekte (Mutante) als auch intakte (Wildtyp) Proteine. Diese organisieren sich in gemischten Oligomeren, in denen Mutanten einen dominant-negativen Effekt auf Wildtype ausüben. Dies führt zu der Frage, wie sich diese beiden Spezies kooperativ beeinflussen. Eine Vielzahl experimenteller Ansätze deutet darauf hin, dass sich Spastin zu ringförmigen Hexameren zusammensetzt. Da jedoch nur Monomere sowie Dimere nachgewiesen werden konnten, legt dies ein sehr dynamisches Verhalten des Proteins nahe. In der vorliegenden Arbeit wird (A) der Oligomerisierungsprozess sowie (B) das inhibierende Verhalten von mutiertem Spastin untersucht.

Um einen tieferen Einblick in diese dynamischen Prozesse zu erhalten, wurde eine Simulation der Hexamerisierung basierend auf den Gillespie-Algorithmus erarbeitet. Diese untersucht zwei unterschiedliche Oligomerisierungspfade, welche die minimal mögliche Anzahl von distinkten Reaktionen erfordern. Beide Pfade gehen davon aus, dass zuerst eine Dimerisierung, anschließend eine Tri- beziehungsweise Tetramerisierung und zuletzt eine Hexamerisierung erfolgt. Entsprechend wurden sie als 1-2-3-6 und 1-2-4-6 Oligomerisierungspfad bezeichnet. Sie konnten die bereits bekannten experimentellen Daten der konzentrationsabhängigen ATP-Aktivität von Spastin widerspiegeln. Die Qualität der Experimente ließ eine eindeutige Zuordnung des Pfades von Spastin jedoch nicht zu.

Veröffentlichte Beobachtungen der Inhibition von Spastin durch seine Mutanten konnten durch ein angenähertes Nachbarschaftsmodell erklärt und gefittet werden, nach dem sich zwei orientierte Hexameruntereinheiten beeinflussen. Damit wird Spastin jedoch auf zwei kooperative Untereinheiten reduziert. Physikalisch ist jedoch ein Hexamer die aktive Form und eine mathematische Beschreibung der Hexamerisierung benötigt das Lösen eines

gekoppelten, nicht-linearen Gleichungssystems. Daher wurde die Simulation um die Implementierung von Mutanten sowie um drei postulierte Inhibitionsmustern erweitert, welche die Kooperativität des Enzyms beschreiben. Diese nehmen an, dass eine Mutante (1) alle Wildtype, (2) seine zwei Nachbarn, oder (3) einen orientierten Nachbarn beeinflusst. Die drei Muster inhibieren unterschiedlich stark, wobei sich Muster 1 am stärksten und Muster 3 am schwächsten auswirkt. Vergleiche mit experimentellen Daten zeigen, dass mutiertes Spastin seine beiden Nachbarn inhibiert. Zudem wurden zwei Fitfunktionen entwickelt, um Experiment und Simulation zu beschreiben. Das nicht-kompetitive Fitmodell zeigt die größte quantitative sowie qualitative Übereinstimmung mit beiden Datensätzen.

Um die einzelnen Oligomerisierungsschritte quantitativ zu charakterisieren, wurden FCS-Messungen durchgeführt. Es wurden Hinweise auf die Oligomerisierung durch Zugabe von ATP gefunden. Eine Unterscheidung in die Zwischenstufen konnte jedoch nicht erfolgen, da die Diffusionskoeffizienten nicht genügend voneinander abweichen. Vergleiche mit bereits veröffentlichten Werten, die durch analytische Ultrazentrifugation bestimmt wurden, deuten darauf hin, dass der geringste gemessene Diffusionskoeffizient dem eines Hexamers entspricht.

Des Weiteren wurde die Inhibition durch MAPs sowie ihre Wechselwirkung mit Mikrotubuli untersucht. Im ATPase Test konnte kein signifikanter Einfluss auf die katalytische Aktivität von Spastin festgestellt werden. Im Motilitätstest wurde nachgewiesen, dass die Geschwindigkeit der Kinesinchimäre reduziert wird. Ebenso nimmt die Anzahl der an Kinesin bindenden Mikrotubuli ab. Mittels Kraft-Ausdehnungsmessungen am AFM wurde die Wechselwirkung zwischen Mikrotubuli und MAPs in der Größenordnung von $1\,\mathrm{nN}$ abgeschätzt. Die Kraft zwischen MAPs und Anti-β-tubulin Antikörper, mittels welcher Mikrotubuli an silanisiertes Glas gebunden wurde, liegt ebenfalls in diesem Bereich. Durch Erhöhung der Salzkonzentration des Puffers wurde die Kraft zwischen MAPs und Mikrotubuli erhöht, die zwischen MAPs und Antikörper wird jedoch nicht beeinflusst. Diese Salzabhängigkeit deutet auf eine ionisch Wechselwirkung zwischen MAPs und Mikrotubuli hin.

Die in dieser Arbeit präsentierten Ergebnisse zeigen, wie maßgebend die Definition eines Oligomerisierungsprozesses sowie die Formulierung eines Inhibitionsmusters sind, um den dominant-negativen Effekt von Mutante auf Wildtypenzym auf molekularer Ebene zu beschreiben. Die hier präsentierten Muster können auch auf andere kooperative AAA Proteine, wie ClpX, angewandt werden.

Summary

Spastin, an ubiquitous AAA protein, has the ability to sever microtubules at the expense of energy obtained from ATP hydrolysis. Mutations in the human gene *SPAST* (or *SPG4*), which encodes spastin, most frequently lead to a hereditary neurodegenerative disorder called HSP. Patients are heterozygous for this gene, implying that they express both the defective (mutated) and the functional (wild type) protein. These proteins form mixed oligomers with a dominant-negative effect of the mutants on the wild types. The question arises, how these two species co-assemble and behave allostericly. Previous experiments indicate that spastin is active as a ring-shaped hexamer. However, no higher oligomeric form than dimers of wild type spastin could be detected, suggesting a highly dynamic oligomerization process of spastin. Furthermore, it has been shown that the addition of mutant spastin leads to a decrease of the activity of the wild type enzyme. In this work (A) the assembly and (B) the inhibitory behavior of spastin were investigated.

To further the understanding of the oligomerization process a simulation of spastin hexamerization based on the Gillespie algorithm was developed. It studies two distinct possible assembly pathways, which require the least amount of different reactions. Both pathways assume that after dimerization either trimerization or tetramerization occurs, before these intermediates form hexamers. Therefore they were termed 1-2-3-6 and 1-2-4-6 assembly pathway respectively. It could be shown that both reflected the experimental data on the ATP-dependence of the activity of spastin very well. However, the quality of the experimental data did not permit identification of the assembly pathway of spastin.

Previously reported observations of the inhibitory effect of mutant on wild type spastin could be explained and fitted very well by an approximated model, which is based on the interaction of only two subunits incorporated into a hexamer. This nearest-neighbor inhibition scheme assumes that the relative orientation of subunits is important for deducing the inhibitory pattern, but reduces spastin to two cooperative subunits. Physically the active form of this enzyme is assumed to be a hexamer, and the mathematical description

of this system comprised of mutants, wild types, and four intermediates would result in a large set of coupled, non-linear differential equations. To overcome this, the simulation was extended by the incorporation of mutants and by postulating three different inhibition schemes describing the cooperative behavior of mutant and wild type enzyme. It was assumed that one mutant inhibits either (1) all wild types, (2) both its neighbors, or (3) one directed neighbor in the hexamer. It could be shown that all three scenarios resulted in different outcomes, where scheme 1 showed the strongest, and scheme 3 the weakest inhibitory effect. Comparison to the experimental data suggests that a spastin mutant effects both its direct neighbors. In addition two fitting formulas for inhibition were developed and tested on experimental and simulated data. A non-competitive fit model represents both data sets very well, quantitatively as well as qualitatively.

The oligomerization process was studied experimentally using FCS as this method is sensitive to different diffusion constants, which the intermediate oligomers exhibit due to their size differences. The measurements imply that the addition of ATP leads to higher order oligomers than observed in its absence, but no clear distinction between the species could be made as the differences in the diffusion constants are small. Comparisons with published data from analytical centrifugation indicate that the smallest measured diffusion coefficients were in accordance to hexamers.

Finally the inhibitory effect of MAPs and their interactions with microtubules were studied. In ATPase activity assays no significant influence on the catalytic activity of spastin could be measured. Gliding assays using a chimeric kinesin displayed a decrease in the gliding velocity as well as a reduction of the number of bound microtubules. The interaction force between MAPs and microtubules, obtained from force-distance measurements using AFM, was estimated to be in the order of $1\,\mathrm{nN}$. However, interactions between MAPs and anti-β Tubulin antibodies, with which microtubules were attached to the silanized glass, were in the same force regime. By increasing the salt concentration of the assay buffer, the interaction force between MAPs and microtubules was increased, whereas the force between MAPs and antibodies remained unaffected. The salt dependency suggests that the interaction between MAPs and microtubules is of ionic nature.

The results of this thesis show that the definition of an assembly pathway as well as the clear formulation of an inhibition scheme are important for studying the dominant-negative effect of mutant on wild type enzyme on a molecular level. The inhibitory scheme presented here can also be applied to other AAA proteins which show cooperativity, e.g. ClpX.

Chapter 1

Introduction

1.1 Motivation

Spastin is an ubiquitous protein that belongs to the family of AAA ATPases (ATPases associated with various cellular activities) and has the ability to sever microtubules, filamentous structures which form a part of the cellular skeleton. To this end chemical energy obtained by the hydrolyzation of ATP (adenosine triphosphate) is used to perform mechanical work. AAA ATPases, which assemble into oligomers, are involved in numerous cellular processes like protein degradation, DNA replication, and membrane fusion. Mutations in the human gene *SPAST* (or *SPG4*), which encodes spastin, most frequently lead to a hereditary neurodegenerative disorder called HSP (hereditary spastic paraplegia), which typically manifests itself in progressive weakness of the lower limbs. In some cases changing a single amino acid is sufficient to cause this disorder as listed in the *Online Mendelian Inheritance in Man* (`http://omim.org/entry/604277?search=spastin&highlight=spastin`). It is likely that the mutated, disease causing variant is co-expressed with the intact, wild type allele. This indicates a strong dominant-negative effect of the mutated on the intact protein. *In vivo* and *in vitro* studies on *SPG10*, a gene encoding the kinesin-1 type microtubule motor protein KIF5A, whose mutations also cause HSP, support this notion (Ebbing et al., 2008, Karle et al., 2012).

1.1.1 Expression of proteins from two alleles

As already indicated, AAA proteins are often catalytically active as oligomeric complexes, which are formed by the assembly of multiple interacting subunits (typically monomers).

The majority of eukaryotes has two copies of the genome in each cell, each inherited by one parent. The expression levels of the two alleles are similar for most of the human genes, in particular no expression was found which is specific to one allele (Pastinen, 2010). Hence these oligomers contain protein expressed from both alleles. If both are very similar and functional, this has no consequences on the organism. However, some pathological cases revealed that the malfunctional gene produces defective proteins and has a dominant-negative effect on the product of the intact allele. The reasons underlying this pattern are various, such as aggregation of the mutated protein, haploinsufficiency, and a negative effect of the mutant on the wild type protein. This work focuses on the latter, where the mutant forms mixed oligomers with the wild type protein and inhibits its proper function.

1.1.2   Enzyme oligomerization

Both HSP inducing enzymes presented here assemble into oligomers in order to become active: KIF5A dimerizes, spastin forms a hexamer. As explained above these oligomers can consist of mutant (defect) and wild type (intact) subunits. To gain a deeper understanding of how they cause HSP, the interplay of these two species of the same enzyme needs to be elucidated.

In the case of kinesin KIF5A the dimers are stable, which means that the timescale of disassembly and reassembly is much larger than their catalytic step. The possible combinations of wild type and mutant in the dimer follow a binomial distribution, assuming the levels of proteins expressed from both genes are similar. Hence the ratio of wt-wt to wt-mut to mut-mut is 1:2:1. The cooperativity of the kinesin motors on each other has been studied well, and the allosteric effect could be shown to occur in several kinesin mutants (Rice et al., 1999, Ebbing et al., 2008).

Spastin, however, is more complex as it assembles into a hexamer, which is in addition highly dynamic, i.e. assembly and disassembly occur on a slower timescale than the catalytic step. Therefore more detailed and complex considerations have to be made considering the orientation of single subunits within the hexamer, the assembly and disassembly rates of intermediates, and the allosteric effect of mutant on wild type spastin.

1.1.2.1   Orientation in and symmetry of the hexamer

A hexamer composed of two different types of subunits, i.e. mutant and wild type, can assemble into 64 different hexamric configurations, which can be subdivided into 14 species

due to the rotational symmetry of a ring. The hexamers are not axial symmetric as they have an upper and lower site (Roll-Mecak and Vale, 2008). Even though the number of incorporated mutants in a hexamer can still be computed using a binomial distribution, this approach neglects the different orientation of wild type and mutant with respect to each other: there are configurations of hexamers containing two mutants, four configurations containing three mutants, and three configurations containing four mutants.

The necessity to consider the orientation of subunits also arises from comparison with other AAA ATPases, which suggest that interactions between two neighboring subunits are important. Especially the arginine residue R499C intruding into the neighboring ATP binding pocket is supposed to be essential for the catalytic step (Ogura et al., 2004, Zhang and Wigley, 2008, Hodson et al., 2012). Reports from patients suffering from HSP substantiate the importance of this arginine finger. (Svenson et al., 2001, Evans et al., 2005). As the arginine finger is oriented within the monomer, the orientations of the mutant and wild type subunits need to be known.

1.1.2.2 Kinetic rates

Kinesin is a stable dimer and therefore its assembly and disassembly rates are negligible. Furthermore, all known mutations do not affect these rates as they are only in the cargo-interacting and catalytic domain, whereas no mutations in the neck domain, which couples the two motors, are known (Jiang et al., 1997, Ebbing et al., 2008, Crimella et al., 2011). GroEL, another well studied heptamer, also displays a catalytic step which is longer than the kinetic rates of the protein (Saibil et al., 2013).

Spastin, on the other hand, is a highly dynamic oligomer. It can be found mostly as monomers, whereas hexamers display a very short lifetime (White et al., 2007, Roll-Mecak and Vale, 2008, Eckert et al., 2012a). Only hydrolyzation defective mutant of human spastin (which has a mutation in the Walker B motif in the ATP-binding site, E442Q) forms hexamers, which are stable enough to be observed in analytical ultracentrifugation, gel filtration, SAXS, and cross-linking experiments (White et al., 2007, Roll-Mecak and Vale, 2008, Eckert et al., 2012a).

In addition, an artificial dimeric spastin construct, consisting of two monomers fused to a coiled coil, displayed the same turnover as the wild type spastin, which is activated by the addition of microtubules (Eckert et al., 2012b). In the absence of microtubules the turnover rate $k_{\mathrm{cat},-\mathrm{Mt}} \approx 1\,\mathrm{s}^{-1}$, which is increased by the addition of microtubules to $k_{\mathrm{cat},+\mathrm{Mt}} \approx 4\,\mathrm{s}^{-1}$. Furthermore, studies using electron microscopy revealed that microtubules stimulate the

oligomerization process and also stabilize oligomers (Eckert et al., 2012b).

These considerations suggest that the oligomerization process of spastin and its catalytic behavior are associated with each other. As spastin can form mixed hexamers, the kinetic rates must be distinguished, as assembly and disassembly rates for the reactions of wild type and mutant subunits can differ.

1.1.2.3 Allosteric effects

Spastin is an allosteric enzyme, resulting from a cooperative mechanism. It has been shown that the addition of the (quasi) non-hydrolyzable ATP analogue ATPγS to a constant concentration of ATP, as well as the titration of mutant spastin to a constant concentration of wild type spastin result in a reduction of the turnover rate of the wild type enzyme. This can only be explained if wild type and mutant monomers form mixed hexamers and at least two of these subunits influence each other. When considering a hexamer the interactions can be even more complex. Systematic inhibition schemes need to be developed to study and predict allosteric effects of mutant subunits on wild type subunits incorporated in a mixed hexamer.

Even though Kinesin and GroEL display allosteric behavior as well, these enzymes are easier to describe as they function as dimers. Kinesin per se is a dimer. GroEL is a complex, consisting of two heptamers. Mutation studies in GroEL were only performed by mutating a whole ring, not single subunits of the oligomer (Yifrach and Horovitz, 1995).

1.1.3 Purpose and outline of this study

The main aim of this work is to further the understanding of the dominant-negative effect of defective genes on intact ones, and hence their enzyme product. The arguments above hint at a complex interplay of the oligomerization process and the catalytic function of spastin. Furthermore dominant-negative effects of mutant subunits on wild type subunits incorporated in mixed hexamers are difficult to predict. Various models on allosteric behavior have been proposed, such as by Adair et al. (1925), Hill (1952), Monod et al. (1963), Koshland et al. (1966). However, they only regard the allosteric coupling by inhibitors, but not by mutants of the same protein. Even though several similar studies on the effect of mutants on wild type enzymes in oligomers were performed for other AAA ATPases, where allosteric behavior was observed, only few addressed this problem conceptionally and systematically (Joshi et al., 2004, Hersch et al., 2005, Martin et al., 2005, Werbeck

et al., 2008, Hoskins et al., 2009, Stotz et al., 2011). However, a model describing each of these individual observations has not been developed so far (Abbondanzieri and Zhuang, 2009).

A mathematical description of the assembly of oligomers using assembly and disassembly rates results in a set of coupled, non-linear equations, which cannot be solved analytically. These complex systems can either be studied using numerical computations of these coupled equations, or by performing simulations to describe the evolution of the system. D'Orsogna et al. (2012), Yvinec et al. (2012) showed that the numerical approach can be inaccurate if finite ensembles may assemble into oligomers of limited size in such a numerical calculation.

Here a simulation based on the Gillespie algorithm was performed. The first part of this study aims at elucidating the process of assembly of spastin monomers into a hexamer. To this end simulations were performed using wild type subunits only, where two different assembly pathways were proposed and investigated. The kinetic rates were optimized, such that simulated and experimental data showed a comparable value of the maximal turnover rate at high protein concentrations. In a next step the inhibitory effect of mutant enzyme on the catalytic activity of wild type enzyme and their inhibitory pattern were studied. Mutants were allowed to incorporate into mixed hexamer together with wild types. Herein their respective rates (which could depended on the relative orientation of the species) were allowed to vary. Three different inhibition schemes were developed to simulate the observed reduction of the turnover rate of the wild type enzyme. Fit models of textbooks were extended in such a way that inhibited wild type subunits showed a slower turnover rate than the catalytically functional subunits. This value could differ from zero. Finally, the simulation was applied to experimental data.

A further part of this thesis was the study of the effect of microtubule associated proteins (MAPs). They bind to microtubules and reduce the possible binding sites for spastin and hence function as an inhibitor. Their effect on the severing property of spastin and on the gliding velocity of kinesin were studied *in vitro*. The study was extended by investigating the interaction force between MAPs and microtubules using atomic force microscopy.

This thesis is outlined as follows: in chapter (1.2) basic concepts and background information are presented. Short overviews on HSP, AAA ATPases with focus on spastin, microtubules and their associated proteins are given. Furthermore, the basic principles of inhibition and cooperativity are presented, including classical models to explain the latter.

In chapter (2) the experimental protocols and measurement procedures are introduced.

The biochemical methods for purifying the required proteins are given. Furthermore, the biochemical reaction of a coupled enzymatic assay is outlined. This is followed by a description of the microscopical methods used in the course of this work. Finally, the Gillespie algorithm, which is the groundwork of the simulation presented here, is introduced, followed by the mathematical description of the fit functions applied to the data.

In chapter (3) the assembly pathway of hexameric enzymes, in particular of spastin, is studied. Experimental data obtained by fluorescence correlation spectroscopy measurements are presented. This is followed by the development of two alternative assembly pathways for the hexamerization process, termed 1-2-3-6 and 1-2-4-6 assembly pathway respectively. Simulations were performed in which the concentration of the protein is increased. Finally, the simulation is applied to experimental data.

In chapter (4) the inhibitory effect of mutant on the turnover rate of wild type enzyme is examined. The first attempt is to simplify the allosteric coupling of an oligomer to the interaction of only two subunits of the hexamer. The simulation developed in chapter (3) is extended by the incorporation of mutant enzyme. The reaction rates are allowed to differ, depending on the interacting partners. Three inhibition schemes were developed to test and predict the allosteric effect of mutants on the wild type subunits in the mixed hexamer. The catalytic activity is calculated per incorporated wild type subunit, not per hexamer. Two fit functions, which were extended from textbook formulas, were applied to the simulated data using the different inhibition schemes. It was further examined if a one-to-one relation between fit function and inhibition scheme could be found. Finally, the simulation was applied to experimental data to elucidate the inhibitory pattern of spastin.

In chapter (5) the effect of MAPs on spastin and kinesin is studied. To this end experiments using an ATPase activity assay and a gliding assay were performed respectively. To further insight into the interaction between MAPs and microtubules force-distance measurements were recorded using atomic force microscopy.

In chapter (6) the results of chapters (3) to (5) are discussed and interpreted. Further experiments are proposed which should help to get a deeper insight into the assembly and inhibitory mechanism of spastin and further the understanding of the dominant-negative effect in oligomers causing HSP.

1.2 Background knowledge

1.2.1 Hereditary spastic paraplegia - HSP

Hereditary spastic paraplegia, first described by Strümpell (1880), is a heterogeneous group of rare, genetic, inherited diseases. Their main clinical feature is the degradation of long axons in the corticospinal tracts, which leads to weakness and progressive spasticity in the lower limbs (McDermott, 2000). HSP can be classified into the pure and the complex (or complicated) form: while in the case of pure HSP the symptoms are mainly limited to the lower limbs, the complicated form shows accessory neurological symptoms as mental retardation, muscle wasting, and epilepsy (Reid, 1999). The first symptoms of HSP can occur in the age of infancy or as late as the eighth decade of life (Blair et al., 2007). About 80% of HSP is an inherited autosomal dominant form, but also autosomal recessive and X-linked inheritance patterns were found (Fink et al., 1996, Blair et al., 2007). More than 40 gene loci have been identified as being related to HSP (Klebe et al., 2006). The proteins encoded by said loci are involved in various cellular processes such as protein folding, cell adhesion, and neural transport. For example, several mutations in gene *SPG10*, which encodes KIF5A, a kinesin-1[1] type microtubule motor protein which functions as a dimer, are known to occur in families suffering from HSP. The motor function of KIF5A is deactivated, suggesting a dominant-negative effect induced by intact and defect gene product. However, Crosby and Proukakis (2002) suggest that these diverse mechanisms lead to anomalies in cellular transporting processes. So far no specific treatment is known which could prevent, slow down, or reverse the disease and hence it can only be treated symptomatically.

One of the most well known causes for HSP are mutations in the gene *SPAST*, the DNA sequence encoding the protein spastin. These mutations lead to 40% of the autosomal dominant HSP (Hazan et al., 1999, Fonknechten et al., 2000). About 120 different mutations of this gene are known: point mutations[2] at splicing sites[3], missense or nonsense mutations[4], insertions, and deletions[5] (Fonknechten et al., 2000). Depending on

---

[1]Kinesins are devided into 14 families as described by Lawrence et al. (2004).

[2]Mutation caused by the change of one singe nucliotide, or the deletion of one base pair in the DNA or RNA.

[3]Splicing is a modification of the pre-mRNA to the mature mRNA in eukaryotic cells. During this process introns are removed and the remaining exons are joined. The splice site seperates introns and exons.

[4]A mutation of nucliotide resulting in another amino acid, or a stop codon respectively.

[5]Insertions and deletions of nucleotides or even amino acids.

the specific mutation, this can lead to frameshifts[6], premature termination of translation, instable mRNAs, instable proteins, or expression of stable but mutated proteins. This leads to the conclusion that for proteins, which are expressed in heterozygotic forms, the pathological effect observed in patients suffering from HSP can either result in a reduced concentration of functional wild type enzyme within the cell (haploinsufficiency) or from a dominant-negative effect of a defective mutant on the proper function of the wild type protein.

1.2.2   AAA Proteins

Proteins of the AAA (**A**TPases **a**ssociated with various cellular **a**ctivities) family are found in all organisms and were first described by Erdmann et al. (1991). They are Mg^{2+} dependent ATPases which use the energy obtained from the hydrolysis of adenosine triphosphate (ATP) to perform molecular remodeling events. They hence execute different functions within the cell, such as membrane fusion (e.g NSF), unfolding of proteins (e.g ClpB), degradation of proteins (e.g. ClpP), transportation along microtubules (e.g. dynein), and severing of microtubules (e.g. spastin) (Latterich and Patel, 1998, White and Lauring, 2007, Snider et al., 2008). The unifying property of these various enzymes is their conserved sequence of 200 - 250 amino acids, which is responsible for ATP binding and hydrolysis. This so-called ATPase domain is located at their C-terminus and includes the Walker A P-loop, Walker B motif, sensor-1 and sensor-2 motifs, and arginine finger (Vale, 2000, White and Lauring, 2007). In addition they have a flexible N-linker at the AAA domain, which may transduce the energy obtained from ATP hydrolysis and the resulting conformational change to the rest of the protein (Smith et al., 2004, White and Lauring, 2007). AAA ATPases can either contain one or two AAA motifs, which are termed D1 and D2 respectively, from which at least one domain is conserved (Latterich and Patel, 1998). The diverse functions are likely encoded in the N-terminal domain of the protein, as AAA proteins typically show little sequence similarity there. It is also considered to be the primary substrate recognition site of the proteins (Lupas and Martin, 2002).

Members of the AAA family are catalytically active as oligomers, mostly as hexamers (Vale, 2000, Iyer et al., 2004, Hanson and Whiteheart, 2005, Snider et al., 2008). According to Vale (2000) the AAA domains assemble into hexameric rings, which are likely to

---

[6]Nucleotides are inserted or deleted, leading to a change in the grouping of three bases, which form a codon encoding specific amino acids. This results in a translation into a protein which differs from the original one.

undergo a conformational change during the cycle of ATP hydrolysis. That in turn might induce a force onto the substrate bound to the AAA protein, and the enzyme can fulfill its purpose. Also the binding of ATP might have a function in the formation and stabilization of the formed oligomer (White and Lauring, 2007). Residues of neighboring monomers incorporated in an oligomer form the ATP-binding pocket, leading to the assumption that the binding of ATP can regulate the oligomerization process of the enzymes. Furthermore, this oligomerization process could enable cooperative hydrolysis of ATP, which has been reported for some members of the AAA family (Hattendorf and Lindquist, 2002, DeLaBarre et al., 2006, White and Lauring, 2007). However, the stability of the formed oligomer can vary, from stable hexamers (e.g. ClpB) to a highly dynamic hexamer (e.g. spastin).

The pore of the hexamer, which is lined by the so-called pore loops (which are also residues in the AAA domain), seems to be a crucial part of AAA proteins and to be important for both protein binding and cellular function of the enzymes. Zolkiewski (2006) showed that some AAA ATPases can pull their binding substrate through their central pore and hence unfold it.

Members of the AAA family can be divided into three groups, depending on their function: non-destructive recycling, quality control, and microtubule associated enzymes, which are described below (White and Lauring, 2007).

1.2.2.1 Recycling

Many members of the AAA family are able to remove their substrate from stable protein complexes, while leaving it intact. The substrate is not unfolded completely and hence can be refolded to fulfill its function, i.e. it is recycled for further use. One representative of this group of AAA ATPases is NSF (N-ethylmaleimide sensitive fusion protein), which is an important element regarding vesicular transport (Block et al., 1988). It regulates the concentration of free SNAREs (soluble N-ethylmaleimide-sensitive-factor attachment receptor) by disassembling them from complexes, which are formed through fusion of a vesicle and its target membrane (Ungermann et al., 1998, Jahn et al., 2003, Whiteheart and Matveeva, 2004).

A further example is VSP4 that can be found at the multivesicular body, which is a sorting pathway and regulates the proteins at the surface of eukaryotic cells. Late in these reactions, when the selection of the cargo is accomplished, VSP4 is involved as it is essential for the recognition and disassembly of the endosomal sorting complex required for transport (ESCRT) (Azmi et al., 2006).

1.2.2.2   Controlling

Several AAA ATPases regulate the unfolding, refolding and proteolysis of proteins, which are targeted or corrupted. The chaperone ClpB locates polypeptides from aggregates and unfolds them. By doing so the peptide can be refolded by further cochaperones (Goloubinoff et al., 1999, Bösl et al., 2006). The protease ClpP together with ClpA or ClpX forms a ring shaped proteasome. The specific substrate is targeted and identified by ClpA or ClpX, translocated through their central pore, and then unfolded and degraded by ClpP (Hoskins et al., 1998, Kim et al., 2000, Smith et al., 2006).

1.2.2.3   Interacting with microtubules

AAA ATPases interacting with microtubules can be divided into two main groups: motor and severing proteins. Dynein, a motor protein which is directed to the minus-ends of microtubules, carries various cargoes along the microtubule and is involved in numerous cellular processes (Schroer et al., 1989, Corthesy-Theulaz et al., 1992, Li et al., 1993). Three enzymes, which sever microtubules by inducing internal breaks, are known: katanin, spastin, and fidgetin (McNally and Vale, 1993, Evans et al., 2005, Roll-Mecak and McNally, 2010). As described by Hartman et al. (1998), McNally et al. (2006) katanin severs microtubules in the mitotic spindle and also in the meiotic spindle in *Caenorhabditis elegans*. Mutations of the human spastin gene can lead to HSP. However, the molecular mechanisms through which these enzymes interact with and sever microtubules are still not elucidated. These enzymes could either translocate and unfold tubulin like the proteins of the Clp family, or by inducing a conformational change during their ATPase cycle they could remove a tubulin hetero-dimer out of the lattice of the intact microtubule.

1.2.3   Spastin

Spastin is an enzyme belonging to the family of AAA ATPases. It interacts with microtubules and is involved in various cellular processes.

1.2.3.1   Structural organization

The longest isoform of human AAA ATPase spastin is encoded in 616 amino acids and is divided into an N-terminal domain (aa 1 – 342), which interacts with the substrate, and a C-terminal domain with the AAA domain (aa 343 – 616), as depicted in figure (1.2). According to Salinas et al. (2007) the N-terminus contains an atlastin binding domain

(a) model of hexameric assembly

(b) different faces and sites of spastin
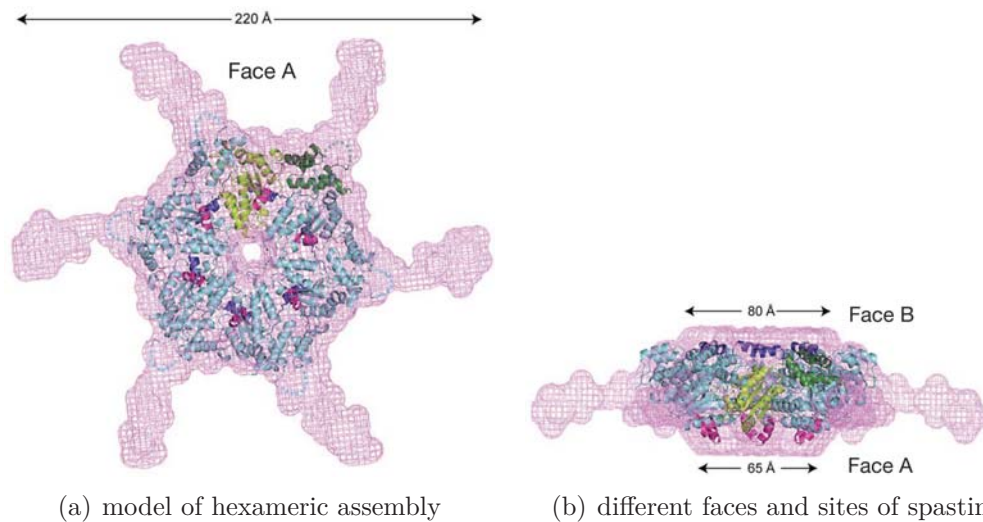
Figure 1.1: Model of a hexameric spastin deduced from scattering experiments (Roll-Mecak and Vale, 2008).
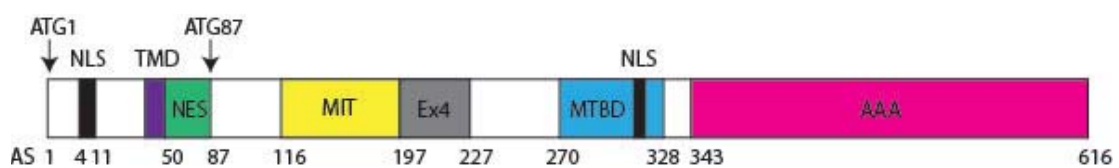
Figure 1.2: Structural organization of spastin: the 616 amino acids are subdivided in an N-terminal domain (aa 1 – 342) and a C-terminal domain with the AAA domain (aa 343 – 616). The N-terminal domain contains different subdomains: an atlastin binding domain, a microtubule interacting and trafficking domain (MIT), a microtubule binding domain (MTBD), two functional nuclear localization signals (NLS), two nuclear export signals (NES), and a putative transmembrane domain (TMD) (Salinas et al., 2007).

(Evans et al., 2006), a microtubule interacting and trafficking domain - MIT (Ciccarelli et al., 2003), a microtubule binding domain - MTBD (White et al., 2007), two functional nuclear localization signals - NLS (Beetz et al., 2004), two nuclear export signals - NES (Claudiani et al., 2005), and a putative transmembrane domain - TMD, which might built intermembrane hairpins (Blackstone et al., 2011). As the sequence of spastin contains two start codons ATG and due to alternative splicing (mostly at exon4) different isoforms of spastin have been reported by Salinas et al. (2005). The concentration and location of the isoforms depend on the tissue and the state of development of the studied organism.

For the studies presented in this work $\Delta 227$ (deletion of aa 1 - 227) human spastin was used, i.e. the different isoforms of spastin are not important in the course of this work.

1.2.3.2   Function

The different locations and isoforms of spastin suggest that spastin is involved in various cellular processes. Spastin has been localized at the central spindle, the spindle pole, and the midbody during cell division (Errico et al., 2004). In neurons spastin is mainly found at the distal axon and at regions related with growth such as sites of branch formation and growth cones (Errico et al., 2004, Solowska et al., 2008). Two main functions of spastin have been studied in more detail in the literature: the intracellular transport, and the interaction with microtubules (and their severing).

Intracellular transport

The first indication of spastin being involved in intracellular transport was given by the identification of the MIT domain in the DNA sequence by Ciccarelli et al. (2003), which shows homologies to proteins associated with endosomal trafficking. Molon et al. (2004) showed that mutated spastin leads to a disruption of exocytic and endocytic pathways within non-pathologic tissue. Furthermore, several interacting partners of spastin could be found: CHMP1B, a protein associated with the transport protein ESCRT-III (Reid et al., 2005), and Retikulon1 (RTN1), which participates in intracellular transport and interacts with spastin via the MIT domain (Mannan et al., 2006). Atlastin, a Golgi-localized integral membrane protein GTPase, is a further interacting partner of spastin and mutations of atlastin can also lead to HSP (Sanderson et al., 2006, Evans et al., 2006).

Microtubule severing

Evans et al. (2005) showed that spastin severs microtubules, both *in vivo* and *in vitro*, by inducing internal fractures. This process only takes place in the presence of ATP, where the Walker A and Walker B motives of the AAA domain bind and hydrolyze ATP respectively (Hartman and Vale, 1999, Roll-Mecak and Vale, 2008). The hexamerization process of spastin is induced by binding of ATP, while hydrolyzation leads to disassembly of the oligomer (Hartman et al., 1998, Hartman and Vale, 1999). The crystal structure of spastin was solved for monomers by Roll-Mecak and Vale (2008), from which asymmetric faces of the hexamer could be deduced (Face A and B of the hexamer, see figure 1.1), further suggesting that Face A interacts with the microtubules. The hexamers can bind via their pore loop to the C-terminus of β-tubulin, and hydrolyzation pulls the substrate through the pore, leading to processes resulting in the release of tubulin (White et al., 2007, Roll-Mecak and Vale, 2008).

However, the exact process is yet unknown. Possible procedures could be the unfolding of tubulin, or a local weakening of interaction between the tubulin dimers incorporated in the microtubule, leading to their release (Roll-Mecak and Vale, 2008). The latter option is very likely as it has been shown that severed microtubules are able to re-polymerize (Roll-Mecak and McNally, 2010). The energy needed to destabilize the microtubules by successively pulling at the C-terminus of the tubulin is lower than the energy required to break the lateral and longitudinal binding of tubulin simultaniously (Roll-Mecak and McNally, 2010).

However, several processes of severing are still unknown, like the exact binding process of spastin to its substrate, the orientation of the hexamer on the microtubule (flat or vertical like a wheel), and the mechanism of spastin locating the spot on the microtubule at which severing actually occurs.

1.2.4 Microtubules

Microtubules are ubiquitous components of the cytoskeleton, which give the cell structure, stability, and motility. Furthermore they are involved in intracellular transport and cell division. To this end they have to be both stable and dynamic at the same time.

The polymerization of dimeric α-β-tubulin[7] leads to the formation of linear protofila-

---

[7]A tubulin dimer consists of two different proteins, termed α- and β- tubulin respectively. α-tubulin binds GTP, which is hydrolyzed by β-tubulin.

(a) polymerization   (b) dynamic instability
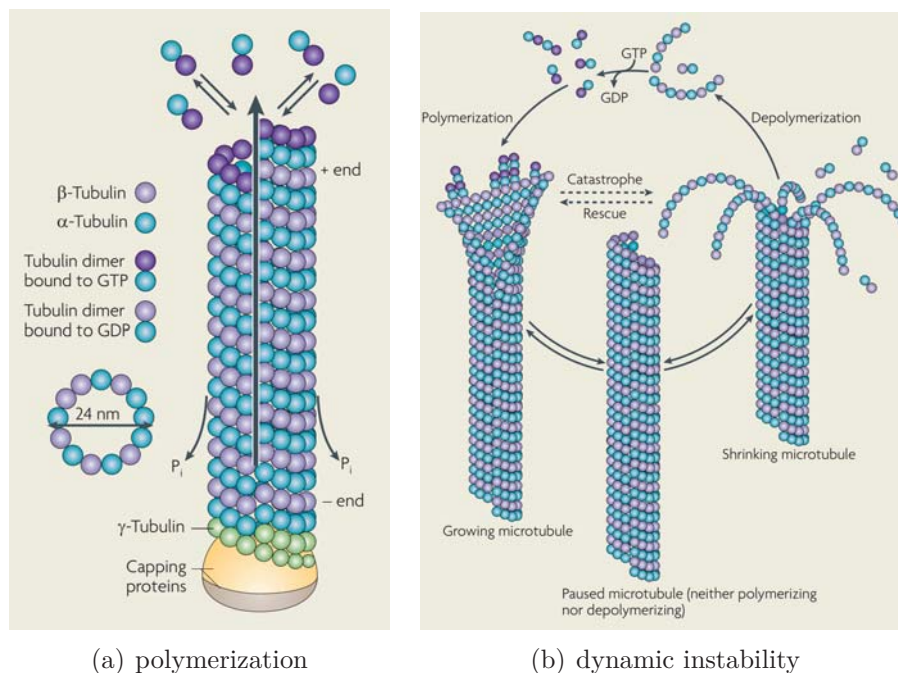
Figure 1.3: Microtubules: panel (a) shows the polymerization process, and panel (b) the dynamical instability of microtubules (Conde and Caceres, 2009).

ments, of which $10 - 15$ (in mammalian cells usually 13) assemble in parallel into a polar, hollow, cylindric microtubule with an inner diameter of about $24\,nm$ as depicted in figure (1.3(a)) (Desai and Mitchison, 1997, Nogales et al., 1998, Conde and Caceres, 2009). For polymerization to occur, guanosine triphosphate (GTP) needs to be hydrolyzed to guanosine diphosphate (GDP) (Erickson and O'Brien, 1992). The energy obtained by this hydrolysis is converted into binding energy of the filament. Free tubulin dimers have a low GTP turnover rate, which is increased when tubulin is incorporated into the filament. The GDP is not released from the filament but stays bound to the tubulin dimer. The growth rate of microtubules differs at the ends, due to their polarity: at the α-tubulin end (minus-end) growth is slow (depending on the concentration and temperature it might also shrink), whereas at the β-tubulin end (plus-end) growth is fast. Hence microtubules are growing at their plus-end and a cap of GTP-bound tubulin is built, which stabilizes the structure. At the same time GDP-bound dimers dissociate at the minus-end, leading to shrinkage of this microtubule end.

However, when the stabilizing GTP-cap is lost, i.e. the hydrolyzation rate is approximately the polymerization rate, the microtubule disassembles rapidly as GDP-tubulin has a high dissociation rate. This sudden change between growing and shrinking is termed

"catastrophe" as shown in figure (1.3(b)). However, the GDP-tubulin can start binding GTP-tubulin, and hence build a new GTP-cap. This is termed "rescue". The interplay of polymerization and depolymerization of microtubules is called dynamical instability (Mitchison and Kirschner, 1984).

1.2.5 Microtubule associated proteins - MAPs

One natural stabilizer of microtubules is the family of microtubule associated proteins - MAPs. They can bind to polymerized and depolymerized tubulin and can dissociate from the microtuble during its shrinking phase. MAPs are divided into two categories: Type I (MAP1) and Type II (MAP2, MAP4, tau). Traditionally, studies on MAPs were performed on MAPs found in brain as they are a side product of the purification of microtubules from brain, but several MAPs can also be recombinantly produced in *E. coli.*

The best known MAPs are the neuronal proteins MAP2 and tau. Both proteins posses a homology in the C-terminus that was shown to bind to microtubules (Mandelkow and Mandelkow, 1995). Depending on the isoform, MAP2 and tau both have three to four binding sites, also called microtubule repeats (Dehmelt and Halpain, 2004). MAP2 can be found mainly in dendrites, while tau protein is typically localized in axons. In solution tau is largely unfolded, and when interacting with microtubules tau remains mobile and mostly disordered (Marx et al., 2006).

1.2.6 Inhibition

When inhibitors bind to enzymes the activity of the enzyme is decreased, slowed down or even prevented. Inhibition can be both reversible and irreversible. Two classes of enzyme inhibitors will be introduced in the following: competitive and non-competitive inhibitors.

1.2.6.1 Competitive inhibition

In competitive inhibition, substrate and inhibitor have to compete for the same binding site as they both cannot bind to the enzyme at the same time, as can be seen in figure (1.4(a)). If sufficient substrate is available, the inhibition can be overcome. This means that the maximal turnover velocity v_{max} is constant, but K_{m}, the necessary concentration of substrate to reach half v_{max}, will increase.
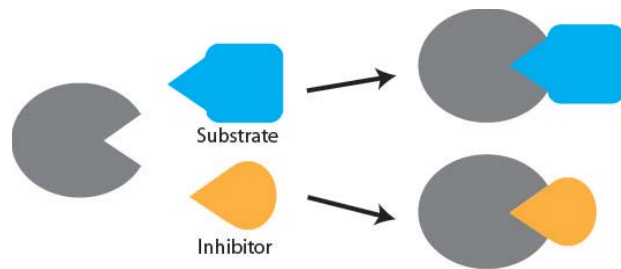
(a) Competitive inhibition
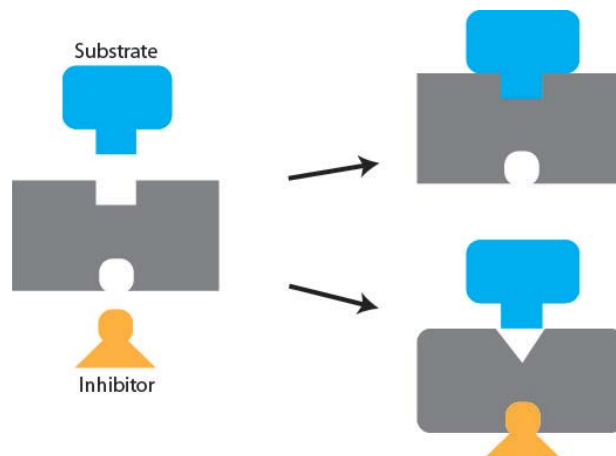
(b) Non-competitive inhibition

Figure 1.4: Competitive and non-competitive inhibition: panel (a) schematically shows the competitive inhibition, where inhibitor and substrate compete for the same binding site. Panel (b) sketches non-competitive inhibition, where the binding of the inhibitor leads to a conformational change of the enzyme.

1.2.6.2 Non-competitive inhibition

Non-competitive inhibition allows the simultaneous binding of inhibitor and substrate as they have two distinct binding sites[8]. In the case that the inhibitor binds, a conformational change of the enzyme and its active site is induced, which makes the binding of substrates more difficult or even impossible (see figure 1.4(b)). The inhibitor can bind to the enzyme or the enzyme-substrate complex, hence reducing the amount of enzyme undergoing catalysis, which in turn results in a lower maximal turnover velocity v_{max}. K_{m}[9] will not be affected by non-competitive inhibition. Increasing the substrate concentration will not reduce the inhibitory effect in this case.

1.2.7 Cooperativity and allostery

The binding of ligands, which can be substrate, inhibitors, activators, or other subunits, can lead to conformational changes of the enzyme or enzyme complex. This can have an effect on the interaction between the binding sites of enzymes and ligands, which is characterized by the binding affinity. If the ligand is bound to an allosteric site, which is different from the active site, this process is termed allosteric regulation. If the ligand binds to the active site and causes such an allosteric effect, this process is termed cooperativity. In both cases the binding affinity can be affected both positively or negatively.

There are several models in textbooks describing this effect. The models of Monod, Wyman, Changeux (MWC, symmetry or concerted model) and of Koshland, Nemethy, and Filmer (KNF, induced-fit or sequential model) describe the cooperative effect on a molecular level as they introduce conformational changes. Adair and Pauling used the reaction rates of ligand binding to describe cooperativity. For a more detailed description see Berg et al. (2007), Voet and Voet (2010).

1.2.7.1 Adair-Pauling equation

A protein with multiple binding sites is likely to bind the substrate sequentially, as for example hemoglobin does. This approach bases on the assumption that each substrate has dissociation rates which are not necessarily equal, and that substrates are bound and dissociated in a timescale much smaller than the catalytic steps. With this ansatz, the

---

[8]The substrate binds to the active site of an enzyme and undergoes chemical reactions. The inhibitor binds to an allosteric/inhibitor binding site.

[9]K_{m} is a measure for the affinity of substrate to enzyme.

fractional saturation of ligand binding Y_S, which is the ratio of occupied ligand-binding sites to the total concentration of ligand-binding sites, for an enzyme with four binding sites (e.g. hemoglobin) is

$$Y_S = \frac{\frac{[S]}{k_1} + \frac{3[S]^2}{k_1 k_2} + \frac{3[S]^3}{k_1 k_2 k_3} + \frac{[S]^4}{k_1 k_2 k_3 k_4}}{1 + \frac{4[S]}{k_1} + \frac{6[S]^2}{k_1 k_2} + \frac{4[S]^3}{k_1 k_2 k_4} + \frac{[S]^4}{k_1 k_2 k_3 k_4}} \quad, \tag{1.1}$$

with the values of k_i being the dissociation rates of the i-th substrate (Adair et al., 1925). The values k_i of this equation describe cooperativity, where decreasing k_i results in positive cooperativity, and increasing k_i leads to negative cooperativity.

The Adair equation describes the general relation of binding ligands to proteins, but gives no microscopic information such as the explanation for different dissociation constants. Oligomers of enzymes usually are composed of identical symmetric subunits. It is therefore useful to understand how the binding of a ligand at one enzyme subunit can influence the ligand-binding site of another enzyme subunit. Pauling (1935) made the first attempt to relate this formula to the geometry of the enzyme.

1.2.7.2   MWC model

In 1965 Jacques Monod, Jeffries Wyman, and Jean-Pierre Changeux formulated the so-called WMC (also symmetry or concerted) model, which assumes the following: an allosteric enzyme forms an oligomer of identical subunits with each subunit having two conformational states (termed tense (T) and relaxed (R) state, which are in equilibrium). The ligand can bind to both states but with different binding affinities between both conformations (see figure 1.5). The symmetry of the oligomers is conserved (Monod et al., 1965). This implies that the complex can either be in T or in the R state and no mixture is allowed. The equilibrium between these states is independent of any ligand binding. However, binding of the ligand stabilizes the state displaying a higher affinity for ligand-binding (which is usually assumed to be the R state).

1.2.7.3   KNF model

Daniel Koshland, George Némethy, and David Filmer made a slightly different attempt to describe allostery (Koshland et al., 1966). In this model, also called induced-fit or sequential model, the subunits can undergo conformational changes independently of one another. Binding of a ligand induces a local conformational change (i.e. the subunit),
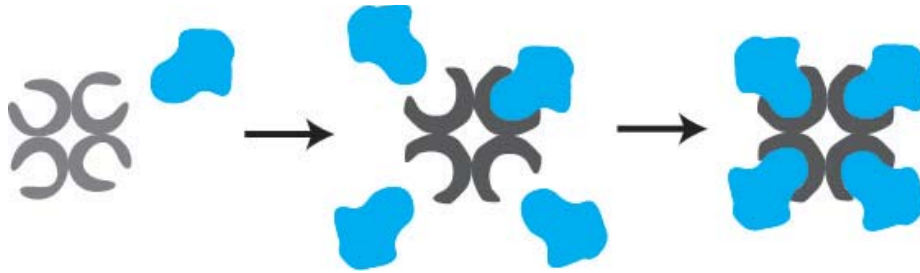
Figure 1.5: MWC Model: the binding of one ligand induces a conformational change of all subunits. The oligomer can only exist in two distinct states, either the R or the T state.
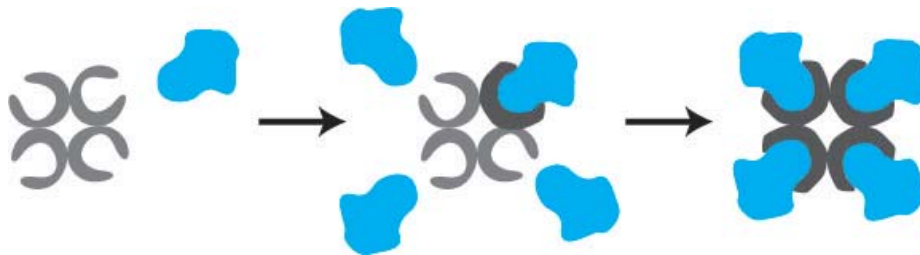
Figure 1.6: KNF Model: the binding of one ligand induces a local conformational change. Subunits coexisting in one enzyme can have different conformational states.

which then leads to a sequential conformational change of the remaining subunits. The corresponding reaction is sketched in figure (1.6). For very fast sequential influences, the KNF model approaches the MWC model.

Chapter 2

Materials, Models and Methods

2.1 Biochemical methods

2.1.1 Isolation, polymerization and labeling of tubulin

Tubulin was isolated from porcine brains using multiple polymerization and depolymerization steps, according to E. M. Mandelkow (1985), Adio et al. (2006) in a two day process. The brains used for these studies were obtained from the Bayerische Landesanstalt für Landwirtschaft, Institute of Animal Breeding (Poing, Germany), on the day of preparation and transported on ice. Microtubule associated proteins were taken from the last polymerization steps and diluted to a concentration of $1 \, \mathrm{mg \, ml^{-1}}$.

For polymerizing microtubules GTP (Jena Bioscience) was added to a final concentration of $1 \, \mathrm{mM}$ to the purified tubulin solution and centrifuged at 4°C, $100000 \, g$ for 10 minutes (Beckmann Coulter; Optima™ MAX-XP Ultrazentrifuge, rotor TLA-120.1) to remove non-polymerizable tubulin. The supernatant was incubated for at least 30 minutes at 35°C. To stabilize the polymerized filaments $20 \, \mu\mathrm{M}$ taxol (AppliChem) was added and incubated at 35°C for another 30 minutes.

In order to remove remaining GTP and non-polymerized tubulin, the microtubules were separated by spin-down over a sucrose cushion (40% w/v in BRB80+ buffer: $80 \, \mathrm{mM}$ PIPES $\cdot$ KOH, $2 \, \mathrm{mM}$ $MgCl_2$, $3 \, \mathrm{mM}$ Mg^{2+}-acetate, $0.5 \, \mathrm{mM}$ EGTA, pH 6.85) at 35°C, $450000 \, g$, for 10 minutes (pre-warmed rotor TLA-100.3). The pellet was then washed several times with BRB80+ buffer and resuspended in 90% of the initial volume in BRB80+ buffer including $20 \, \mu\mathrm{M}$ taxol.

The concentration of microtubules was measured photometrically at $280 \, \mathrm{nm}$ in the

presence of 6.6 M guanidinium hydrochloride, which leads to their denaturation (Huang and Hackney, 1994). The resulting concentration of tubulin dimers can be computed using the Lambert-Beer law

$$A_\lambda = \epsilon \cdot c \cdot d \, , \tag{2.1}$$

where A_λ denotes the absorption at the wavelength λ, ϵ the extinction coefficient (in case of tubulin $\epsilon = 1.03 \, \text{ml} \, \text{mg}^{-1} \text{cm}^{-1}$), c the concentration (in this case in units of $\text{mg} \, \text{ml}^{-1}$) and d the path length in cm (the thickness of the cuvette used here is 1 cm). The concentration in units of molar is then given by

$$c_{\text{protein}} \, [\text{mol/l}] = \frac{c_{\text{protein}} \, [\text{mg/ml}]}{M_{\text{protein}}} \, , \tag{2.2}$$

where $c_{\text{protein}} \, [\text{mg/ml}]$ is the concentration of the protein in units of $\text{mg} \, \text{ml}^{-1}$, M_{protein} the molecular weight of the protein (for tubulin $M = 100000 \, \text{g/mol}$). With equation (2.1) and equation (2.2) the concentration of tubulin can be computed via

$$c_{\text{tubulin dimer}} \, [\mu\text{M}] = \frac{A_{280}}{1.03} \cdot 10 \cdot \beta \, , \tag{2.3}$$

where β denotes the dilution factor.

Fluorescent microtubules were prepared as described in Hyman (1991), Ebbing et al. (2008), using covalent binding between tubulin dimers and Alexa Fluor® 555 (Invitrogen) or Atto 488 (Atto Tec) with NHS-ester respectively. Non-polymerizable labeled tubulin was removed by various polymerization and depolymerization steps. For microscopy usage, already labeled tubulin was polymerized with non-labeled tubulin as described above, including a purification step via sucrose cushion. The ratio of labeled to non-labeled tubulin varied depending on the different preparations of the stock samples, but usually were about 5:100 (labeled to non-labeled tubulin).

2.1.2   Purification of Kinesin and Spastin

$\Delta 227$ human spastin with an N-terminal GST-tag was expressed in *E. coli BL21(RIL)* and purified using GSH-sepharose (GE) affinity, ion exchange (GE) and gel filtration (GE) chromatography as described by Roll-Mecak and Vale (2008), Eckert et al. (2012a). The measurements of the effects of MAPs on kinesin were carried out in collaboration with Daniela Bauer at the lab of Prof. Dr. M. Rief. The chimeric Dm-ht kinesin cys-light, consisting of a human tail (A389-H546 human) and a Drosophila Melanogaster head domain
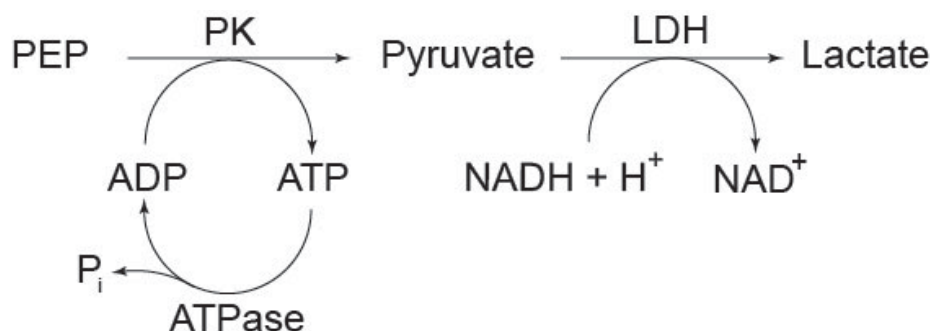
Figure 2.1: A reaction scheme of a coupled enzymatic ATPase assay: PEP reacts under the addition of PK to pyruvate, while regenerating ADP to ATP. The pyruvate undergoes a redox reaction to lactate, where the cofactor NADH acts as a reducing agent and NAD$^+$ is generated. LDH is used to catalyze this reaction. The decrease of NADH can be observed at 340 nm.

(M1-L393 Drosophila) with all exposed cysteins (C45S and C338S) being mutated, was expressed in *E. coli BL21(RIL)* and purified by Ni^{2+}-NTA affinity chromatography and ion exchange as described by Vukajlovic (2012).

2.1.3 Coupled enzymatic ATPase assay

Enzymatically active AAA proteins hydrolyze ATP to ADP and inorganic phosphate P_i. Hence the number of hydrolyzed ATP is an indicator for the enzyme's catalytic activity. One way to monitor the turnover of ATP is given by the so-called "coupled enzyme ATPase assay", where the ADP recovery to ATP is coupled to a photo detectable reaction. The reactions are the following (see figure 2.1): ATP is hydrolyzed by an ATPase to ADP and P_i. A regeneration system is used, where the phosphate group is transferred from phosphoenolpyruvate (PEP) to ADP by pyruvate kinase (PK). This results in the reconversion of ADP to ATP and the production of pyruvate. This pyruvate undergoes a redox reaction to lactate, under the oxidation of the cofactor nicotinamide adenine dinucleotide (NADH to NAD$^+$), which acts as a reducing agent. This reaction is catalyzed by lactate dehydrogenase (LDH). Hence the coupled enzyme ATPase assay gives a one-to-one correspondence between the number of ATP hydrolyzed and the decreased number of NADH. This can be followed photometrically by monitoring the absorption at $\lambda = 340$ nm as NADH has two absorption peaks at 340 nm and 260 nm, whereas NAD$^+$ has a single maximum at 260 nm.

The amount of ATP hydrolyzed is equal to the decrease of NADH over time. The Lambert-Beer law (equation 2.1) with $\epsilon_{\text{NADH}} = 6.22 \cdot 10^3 \, \text{M}^{-1}\text{cm}^{-1}$ can be translated to

$$\frac{\mathrm{d}}{\mathrm{d}t}c_{\mathrm{ATP}} = \frac{\frac{\mathrm{d}}{\mathrm{d}t}A_{340}}{\epsilon \cdot d} \ . \tag{2.4}$$

From this one can compute the catalytic turnover rate k_{obs} in the case that the amount of inserted protein is known. The latter is given by

$$c_{\mathrm{protein}} \, [\mathrm{mol/l}] = \frac{c_{\mathrm{protein}} \, [\mathrm{mg/ml}] \cdot V_{\mathrm{protein}}}{M_{\mathrm{protein}} \cdot V_{\mathrm{total}}} \ , \tag{2.5}$$

with $M_{\mathrm{Spastin}} = 44000 \, \mathrm{g/mol}$, V_{total} the volume used in the assay (in this case $80 \, \mu\mathrm{l}$) and V_{protein} the volume of inserted protein. Knowing this, the turnover rate per monomer is given by

$$\begin{aligned} k_{\mathrm{obs}} \, \left[s^{-1} \right] &= \frac{\frac{\mathrm{d}}{\mathrm{d}t}c_{\mathrm{ATP}}}{c_{\mathrm{protein}} \, [\mathrm{mol/l}]} \\ &= \frac{\frac{\mathrm{d}}{\mathrm{d}t}A_{340\,\mathrm{nm}} \cdot M_{\mathrm{protein}} \cdot V_{\mathrm{total}}}{\epsilon \cdot d \cdot c_{\mathrm{protein}} \, [\mathrm{mg/ml}] \cdot V_{\mathrm{protein}}} \ . \end{aligned} \tag{2.6}$$

The reactions were carried out in BRB80+ buffer in presence of an ATP regenerating system consisting of $2 \, \mathrm{mM}$ PEP (Sigma), $0.3 \, \mathrm{mM}$ NADH (Carl-Roth), $2 \, \mathrm{U \, ml^{-1}}$ PK (Sigma) and $3 \, \mathrm{U \, ml^{-1}}$ LDH (Sigma). ATP, enzyme, microtubules, and MAPs were added at the concentrations required for the specific measurement, where MAPs and microtubules were pre-incubated for 5 minutes at room temperature. In the case that the effect of microtubules on the turnover rate was examined, the concentration of ATP was chosen to be at saturating conditions ($2 \, \mathrm{mM}$). The titration of ATP was studied at a saturating concentration of microtubules (about $25 \, \mu\mathrm{M}$). If microtubules were present, $1 \, \mathrm{mM}$ DTT was added to stabilize them. The reaction was initiated by the addition of AAA ATPase protein and recorded over 5 minutes. For the measurements presented here a Lambda 25 UV/VIS spectrophotometer (Perkin Elmer) was used.

2.2 Microscopy methods

2.2.1 Fluorescence correlation spectroscopy - FCS

FCS is a microscopy technique, invented in the 1970s by Douglas Magde, Elliot Elson and Watt W. Webb, which measures fluorescence intensity fluctuations on the single molecule level (Magde et al., 1972, Elson and Magde, 1974, Magde et al., 1974). Technically the setup

(a) Confocal volume   (b) Time trace of Alexa488   (c) Auto-correlation
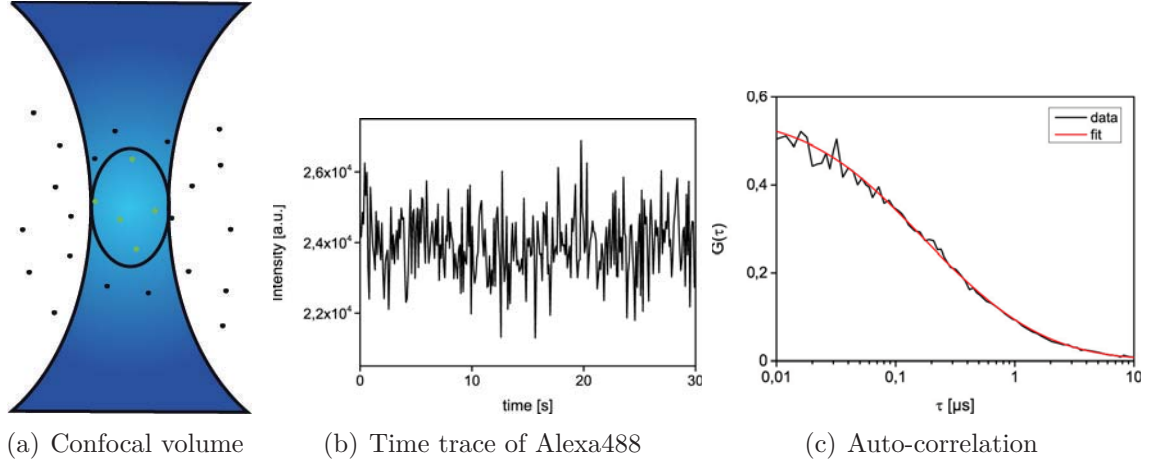
Figure 2.2: FCS: panel (a) shows fluorescently labeled particles diffusing through a confocal volume. They are only excited if they are in said volume. Panel (b) displays the time trace of intensity fluctuations of the freely diffusing dye Alexa488, which results in the auto-correlation depicted in panel (c). The red curve depicts a fit to the data according to equation (2.10).

is realized using a confocal microscope, which is basically a fluorescence microscope with an additional pinhole in front of the detector. Therefore only emission from the focal plane is detected. This in turn leads to a small excitation volume of the order of 10^{-12} l and sample concentrations of should be in the range of 1 - 100 nanomolars. Fluorescently labeled particles diffuse through the excitation volume due to Brownian motion and the detector records temporal fluctuations of the fluorescence signal. The autocorrelation function

$$G\left(\tau\right) = \frac{\langle \delta F\left(t\right) \delta F\left(t+\tau\right)\rangle}{\langle F\left(t\right)\rangle^2} \tag{2.7}$$

is used to compare the signals at time t and at lag time $t+\tau$, where $\delta F(t) = F(t) - \langle F(t)\rangle$ denotes the deviation from the mean fluorescence intensity and the angle brackets indicate averaging over time. Assuming that the optical pathway is well adjusted, the spacial distribution of the intensity in the excitation volume (which is equal to the focus of the laser) can be approximated by a 3D Gaussian

$$I\left(x, y, z\right) = I_0 exp\left(-\frac{2\left(x^2 + y^2\right)}{\omega_{\mathrm{xy}}^2} - \frac{2z^2}{\omega_{\mathrm{z}}^2}\right) \;, \tag{2.8}$$

with I_0 being the maximum intensity and ω_{xy}^2, ω_{z}^2 the radii of the Gaussian in the respective directions (laser in z direction). With this assumption the intensity fluctuation signal can

be computed to

$$\delta F(t) = \gamma \epsilon Q \int I(\mathbf{r})\, \delta c(\mathbf{r}, t) \mathrm{d}^3\mathbf{r} \; , \tag{2.9}$$

with δc the fluctuations in concentration, γ the efficiency of the detector, ϵ the extinction of the sample and Q the quantum efficiency of the dye. With this and the assumption of freely diffusing particles, equation (2.7) can be calculated analytically to (see Petrov and Schwille, 2008)

$$G(\tau) = \frac{1}{\bar{N}} \cdot \frac{1}{1 + \frac{\tau}{\tau_{\mathrm{D}}}} \cdot \frac{1}{\sqrt{1 + \frac{\tau}{S^2 \tau_{\mathrm{D}}}}} \; , \tag{2.10}$$

where $\bar{N}$ denotes the mean number of particles in the excitation volume, τ_{D} the average diffusion time of the particle through the volume in xy direction and the ratio $S = \omega_{\mathrm{z}}/\omega_{\mathrm{xy}}$, the structure parameter. Given the diffusion time τ_{D}, the diffusion coefficient D of the particle can be computed using

$$D = \frac{\omega_{\mathrm{xy}}^2}{4\tau_{\mathrm{D}}} \tag{2.11}$$

from which the hydrodynamic radius R of the particle can be determined by invoking the Stokes-Einstein equation

$$D = \frac{k_{\mathrm{B}} T}{6\pi\eta R} \; , \tag{2.12}$$

with k_{B} the Boltzmann constant, T the sample's temperature during measurement and η the medium's viscosity. Hence with FCS a sensitive method for measuring diffusion times and diffusion constants, kinetics of chemical reactions as well as hydrodynamic radii of diffusing particles is given. For a more detailed description of FCS see Schwille and Haustein (2006).

For the FCS measurements presented in this work a commercial ConfoCor 2 (Zeiss, Germany) FCS setup with a $40\times$ water emission objective was used. The assay was performed in 8-well chambers (IBIDI). The Atto488 labeled spastin was diluted to a concentration smaller than $100\,\mathrm{nM}$ using high-salt buffer ($50\,\mathrm{mM}$ HEPES $\cdot$ KOH, $300\,\mathrm{mM}$ NaCl, $5\,\mathrm{mM}$ MgCl$_2$ and 5% glycerol (v/v) at pH 7,4) without DTT. The laser intensity was set such that no observable photo bleaching occurred during measurement. To prevent the protein from binding to the surface unspecifically, BSA of a concentration of $1\,\mathrm{mg/ml}$ was pre-incubated for at least $25\,\mathrm{minutes}$ to create a saturated surface. The chambers were then washed several times with ddH$_2$O to remove free BSA. The recording time for each measurement was set to 20 seconds. For each chamber $10 - 20$ runs were performed and the average was computed by the acquisition software.
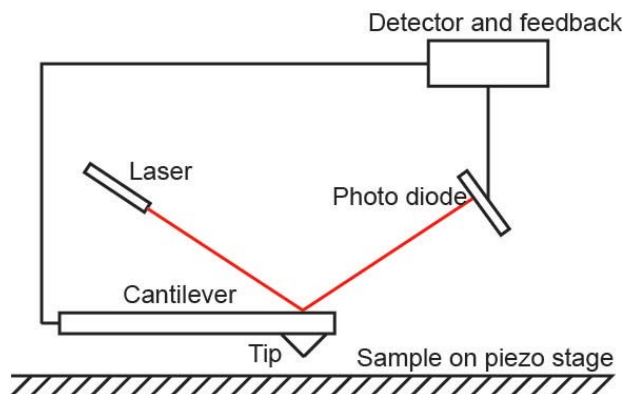
Figure 2.3: Schematic principle of an AFM: the sample set on a piezo table. Interactions between tip and sample result in a deflection of the tip, which in turn changes the signal of the laser on the photo diode. The detector generates an image of the sample while the feedback loop regulates the distance between tip and sample according to the chosen mode.

Estimation of the diffusion time using the sedimentation coefficient

Another technique to obtain the diffusion constant is given by analytical centrifugation, where the sedimentation coefficient s is determined. The diffusion constant and hence the diffusion time τ_{D} can be calculated from this. However it is important to note, that the determined sedimentation coefficient has a large uncertainty range (Eckert, 2012). The relation between the diffusion coefficient and sedimentation coefficient is given by

$$D = \frac{sRT}{M_{\mathrm{protein}}\left(1 - \bar{V}\rho\right)} \ , \tag{2.13}$$

where R is the gas constant, T the temperature (in the experiments $T = 277\,\mathrm{K}$), $\bar{\rho}$ the partial specific volume of the macromolecule (approximated by $1/1.4\,\mathrm{ml\,g^{-1}}$), and ρ the solvent's density ($\approx 1\,\mathrm{g\,ml^{-1}}$). Using equation (2.11) the diffusion time can be computed ($\omega_{\mathrm{xy}}^2 = 0.4 \cdot 10^{-9}\,\mathrm{cm^2}$ in the experimental setup used).

2.2.2 Atomic force microscopy - AFM

AFM, which was developed in 1986 by Binnig et al. (1986), is a scanning probe microscopy technique where the interacting force between the atoms in the tip and the sample is measured. The resulting image of the sample surfaces can be of atomic resolution. The basic principle is illustrated in figure (2.3). A cantilever with a tip at its end is brought close to the sample's surface. Due to their interaction a force is generated which results in

the deflection of the cantilever. This can be measured using a laser beam that is reflected by the cantilever and detected by a photo diode. A feedback system adjusts the distance between tip and surface, e.g. with a piezo element.

In order to image the sample, its surface has to be scanned. This can be done with different imaging modes: the static and the dynamic mode. In the first one the tip and the surface are in contact, leading to an interaction and deflection of the cantilever. In this mode, also called contact mode, either the force or the distance is kept fixed for imaging. In the dynamic mode, however, the cantilever does not touch the surface but it oscillates at a frequency close to its resonance frequency. The cantilever can be regarded as a damped harmonic oscillator described by

$$m\ddot{x} + \gamma\dot{x} + kx = F_0 \cos\omega_0 t \ , \tag{2.14}$$

where m is the mass, γ the damping constant, k the spring constant, F_0 the excitation frequency and ω_0 the resonance frequency. As the force F generated by the surface-tip interaction modifies k to

$$k_{\text{eff}} = k - \frac{\partial}{\partial z}F \tag{2.15}$$

the new resonance frequency is

$$\begin{aligned}
\omega_0' &= \sqrt{\frac{k - \frac{\partial}{\partial z}F}{m}} \\
&= \omega_0\sqrt{1 - \frac{1}{k}\frac{\partial}{\partial z}F} \ .
\end{aligned} \tag{2.16}$$

Under the assumption that the force gradient in z direction is small compared to the spring constant the shift of the resonance frequency can be estimated by

$$\begin{aligned}
\Delta\omega_0 &\approx \omega_0 - \omega_0' \\
&= -\frac{\omega_0'}{2k}\frac{\partial}{\partial z}F \ .
\end{aligned} \tag{2.17}$$

If the force is attractive then $\Delta\omega > 0$, if it is repulsive then $\Delta\omega < 0$. The image is then generated using the information of the tip-surface distance.

A further application of AFM is force spectroscopy. Here the force between the tip and the sample is measured as a function of their distance, resulting in a force-distance curve (Florin et al., 1994). The sample of interest is either attached to a cover slip or to the tip

and the latter is being retracted. When the distance between tip and cover slip gets larger than the length of the sample, a force is exerted which can be measured via deflection of the tip and hence the laser. A slight modification of this setup can be used to study the strength of the interaction between two protein samples. In order to achieve this, sample one is stuck on the cover slip and sample two to the tip. If there is an interaction, the force will be different compared to the one measured between functionalized tip and plain cover slip.

The AFM experiments presented in this thesis were performed in co-operation with Sandra Kienle from the group of Prof. Dr. T. Hugel. For the interaction measurements, MAPs were covalently attached to the tip using a flexible poly(ethylene-glycol)-linker (Rapp Polymere GmbH, Tübingen, Germany) according to Kienle et al. (2012). The tips were then stored in PBS buffer until usage.

The cover slips were silanized using different protocols and types of silane. For the first technique a cover glass was put into a plasma chamber (Electronic Diener Femto) with oxygen at 20% power, 0.26 mbar for 15 minutes. Then it was rinsed with acetone and incubated in a solution consisting of 5 ml acetone and 100 μl aminosilane (Vectabond$^{®}$, Axxora, Lörrach, Germany). Afterwards the cover glass was rinsed with acetone and ddH$_2$0 and dried under a nitrogen stream.

The second technique to silanize the glass cover slips was the following: the cover slips (Carl Roth) were plunged in ddH$_2$0 and ethanol for 20 minutes respectively. This procedure was performed twice. Afterwards they were put into an oven at 70°C to dry for 1 hour. Subsequently the slides were incubated in 0.05% dimethyldichlorosilane (Fluka) diluted in toluene for 1 hour. The functionalized cover slips were rinsed with ethanol to remove non-bound silane, then cleaned with ddH$_2$0 and ethanol for 20 minutes respectively twice and dried over night in an oven at 70°C.

In order to specifically bind microtubules onto the surface, anti-β-tubulin antibodies (Sigma-Aldrich) were used (on slides covered with dimethyldichlorosilane for force-distance measurements, for imaging also on Vectabond$^{®}$). The incubation time for each of the following steps was 10 minutes with enough fluid to get a large droplet on the glass surface (usually about 40 μl). The antibody, diluted in BRB80+ (1:400 of the stock solution), was incubated. Afterwards the glass was rinsed with twice the volume of BRB80+, and non-covered spots were then saturated with 5% PluronicR-F127 (Sigma-Aldrich) in BRB80+. Subsequently it was cleaned again with twice the volume of BRB80+. Finally polymerized microtubules were added (about 100 μM) and incubated for at least 15 minutes.
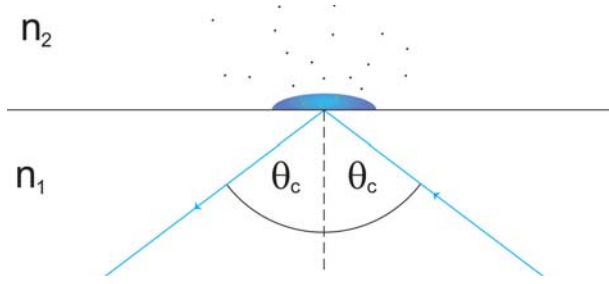
Figure 2.4: Schematic principle of a TIRF microscope: A laser beam strikes the boundary of two media with different refractive indexes, where $n_1 > n_2$, at the critical angle Θ_C and is reflected totally. The induced evanescent wave (blue spot in the figure) excites only fluorophores close to the surface.

As a negative control, the glass silanized using Vectabond® was coated with mPEG (MS(PEG)4, Thermo Scientific, Germany). The NHS-ester binds to the aminosilane on the surface and the methyl group (CH_3), which is supposed to be inactive, is free. Hence it should not show any interaction with the MAPs. To this end the slides were put into a plasma chamber (60 minutes, 50% power, 0.3 mbar), then incubated 10 minutes in Vectabond® and finally 30 minutes in MS(PEG)4.

For the experiments a MFP – 3D SA (Asylum Research, Santa Barbara, CA) AFM setup was used. In order to obtain the desorption force the spring constant was determined for each cantilever (MLCT from Bruker, SPM probes, Camarillo, CA) prior to measuring. This calibration, using the thermal noise method, is described by Pirzer and Hugel (2009). The inverse optical lever sensitivity (InvOLS) was recorded before and after the measurement, five times each. For recording a force-distance curve the cantilever was moved to the surface with a constant velocity of $1\,\mu m\,s^{-1}$, remained there for a dwell time of 10 seconds for interaction, and was then retracted with a constant velocity of $1\,\mu m\,s^{-1}$. Imaging was performed with an AC240TS cantilever (Olympus).

For the evaluation of the force-distance curves the maximal force F_{max} and the length of interaction l, i.e. the first point with $F = 0$, were determined.

2.2.3   Total internal reflection fluorescence microscopy - TIRFM

TIRFM is a microscopy technique which excites fluorophores close to the surface. When an electromagnetic wave strikes the boundary of two media with different refractive indices n_i the refraction will follow Snell's law (see figure 2.4):

$$n_1 \sin \Theta_1 = n_2 sin \Theta_2 \ . \tag{2.18}$$

If $n_1 > n_2$ and the incident angle is at least at the critical value

$$\Theta_{\mathrm{C}} = \arcsin\left(\frac{n_1}{n_2}\right) \ , \tag{2.19}$$

total internal reflection occurs. In the optically thin medium an electromagnetic field, which is known as an evanescent wave with the same wavelength as the incident wave, is induced. As it decreases exponentially with distance only fluorophores within a range of a few nanometers close to the surface will be excited.

For the measurements here an objective type TIRF microscope was used (inverted microscope IX71, Olympus Biosystems GmbH, Planegg, Germany). The excitation laser beam is introduced through the microscope and an oil-immersion objective with a numerical aperture $N.A. > 1.4$ is used to achieve the required critical angle. For a more detailed review see Fish (2001).

Gliding assay

A gliding assay was performed using a TIRF microscope to observe microtubules being transported by kinesin in absence and presence of MAPs. For this cover slips were cleaned superficially by kimwipes (Kimberly-Clark). The assay was performed in the assay buffer, which consisted of HS-BRB80 buffer (80 mM PIPES · KOH, 2 mM $MgCl_2$, 1 mM EGTA, 5 mM DTT, 100 mM K-acetate, pH 6.9) with an additional O_2 scavenger system (glucose oxidase and catalase), 0.2 mg ml^{-1} casein and 2 mM ATP. After building flow chambers 8 μM kinesin was allowed to bind for 5 minutes, then rinsed with ten times the chamber volume of HS-BRB80 buffer. A solution of diluted microtubules (about 330 nM) in assay buffer was rinsed and the data acquisition initialized. The exposure time was chosen to be 100 ms and the sampling rate 150 ms.

To evaluate the data the program Fiji (open source image processing package based on ImageJ) was used. The movement of one end of the microtubule was followed over a known distance (in our case over 50 frames). A micrometer scale was used to convert pixels into micrometers. With these values for distance and time, the gliding velocity was then computed.

2.3   Computational methods

2.3.1   Gillespie algorithm

The Gillespie algorithm is named after Daniel T. Gillespie who used it to describe chemical reactions numerically (Gillespie, 1976, 1977). With this algorithm even reactions with small numbers of molecules and also non-linear reactions (dimerization of the same species) can be computed. It is equivalent to solving the Master equation of a set of chemical reactions assuming that these reactions occur homogeneously within a given volume, the system is in thermal equilibrium, and the molecules exhibit a Maxwell-Boltzmann distributed velocity[1]. Each reaction involves two molecules at most (one molecule would result in its dissociation), as the probability of more species reacting at the same spot at the same time is negligible. Furthermore, the next reaction depends only on the current configuration of the system and is independent of any past events (the system is memoryless). The essential value which is needed in order to create a simulation based on the Gillespie algorithm is the probability that a certain reaction r_i occurs at time t. The following derivation can be read in more detail in Gillespie (1976), Fontana (2007), Timmer (2012).

The probability of a specific reaction r_i to occur within the time interval $t_0 + t$ and $t_0 + t + \mathrm{d}t$ is

$$p(i, t) \, \mathrm{d}t = p_0(t) \, p_i(\mathrm{d}t) \ . \tag{2.20}$$

Here $p_0(t)$ is the probability that no reaction takes place between t_0 and $t_0 + t$ and $p_\mathrm{i}(\mathrm{d}t)$ is the probability that the reaction r_i does occur within $t_0 + t$ and $t_0 + t + \mathrm{d}t$, and is given by

$$p_i(\mathrm{d}t) = a_i \, \mathrm{d}t \ . \tag{2.21}$$

a_i is the probability of the reaction r_i and it is the product of the reaction rate k_i for the reaction r_i and the number of possible reactions r_i.[2] The probability that any arbitrary reaction out of N possible ones happens within a time interval of $t_0 + t$ and $t_0 + t + \mathrm{d}t$ is

---

[1]The Maxwell-Boltzmann distribution is given by $p(v) = 4\pi \left(\frac{m}{2\pi k_\mathrm{B} T} \right)^{3/2} v^2 \exp\left(-\frac{mv^2}{2k_\mathrm{B} T} \right)$. It describes the distribution of the velocity of the particles in dependence of the temperature.

[2]An example: for dimerization of two species into a hetero-dimer $E_1 + E_2 \rightarrow E_3$, the probability is given by $a_i = k_i E_1 E_2$. For the case of homo-dimerization the probability is then $a_i = k_i E_1 (E_1 - 1)/2$.

given by

$$p\left(\mathrm{d}t\right) = \sum_{i=1}^{N} a_i \mathrm{d}t$$
$$= a\,\mathrm{d}t \ , \tag{2.22}$$

where a is the sum over all a_i. The probability of no reaction taking place at all is

$$p_0\left(t + \mathrm{d}t\right) = p_0\left(t\right)\left(1 - a\,\mathrm{d}t\right)$$
$$\Leftrightarrow \quad \frac{p_0\left(t + \mathrm{d}t\right) - p_0\left(t\right)}{\mathrm{d}t} = a p_0\left(t\right) \ , \tag{2.23}$$

which is a linear differential equation with the solution

$$p_0\left(t\right) = \exp\left(-at\right) \ . \tag{2.24}$$

With equations (2.21) and (2.24) the probability of reaction r_i occurring at time t (see equation 2.20) is

$$p\left(i, t\right) = a_i \exp\left(-at\right) \ . \tag{2.25}$$

Using equation (2.25) the calculations for the simulations of chemical reactions can be performed. To calculate at what time a reaction happens, the sum over all possible reactions has to be built:

$$\bar{p}\left(t\right) = a \exp\left(-at\right) \ . \tag{2.26}$$

The corresponding reaction can be computed via the conditional probability

$$p\left(i \mid t\right) = \frac{p\left(i, t\right)}{\bar{p}\left(t\right)}$$
$$= \frac{a_i}{a} \ . \tag{2.27}$$

The probability $p(i, t)$ (equation 2.25) is an important quantity to simulate the development of a system with time. The Gillespie algorithm consists basically of two Monte Carlo simulations[3], one for the time t and one for the reaction r_i. Initial values are the particle numbers of all species present in the system as well as their reaction rates. With these, the values for all a_i, which depend on the numbers of molecules and hence change

---

[3]Monte Carlo simulations are computational methods that use random sampling in order to obtain numerical results.

after each iteration, are computed. Two random numbers x_1 and x_2 are introduced which are uniformly distributed within the interval $]0;1]$. Using x_1 it can be determined which reaction r_i will take place according to

$$\sum_{j=1}^{i-1} \frac{a_i}{a} < x_1 \leq \sum_{j=1}^{i} \frac{a_i}{a} \ . \tag{2.28}$$

The time t at which this event occurs can be computed using the cumulative distribution function $F(t)$ of $\bar{p}(t)$

$$\begin{aligned} F(t) &= \int_{-\infty}^{t} \bar{p}(t) \\ &= 1 - \exp(-at) \ , \end{aligned} \tag{2.29}$$

which, under the condition $F(t) = x_2$, leads to

$$\begin{aligned} t &= \frac{1}{a} \ln \left(\frac{1}{1 - x_2} \right) \\ &= -\frac{1}{a} \ln x_2 \ , \end{aligned} \tag{2.30}$$

with x_2 being the second random number drawn. The second equality in equation (2.30) is due to the fact, that $1 - x_2$ and x_2 exhibit the same distribution.

The implementation of the algorithm works according to the following scheme (see also figure 2.5), assuming the system is determined at a given time τ:

1. Initialize the system by defining the number of molecules of each type represented in the reaction and their respective reaction rates.

2. Compute a_i and hence a.

3. Draw one random number x_1. If $x_1 \in]0; a_1/a]$ reaction r_1 occurs, if $x_1 \in]a_{i-1}/a; a_i/a]$ reaction r_i occurs (see figure 2.6).

4. Draw one random number x_2 and compute the time $\Delta\tau$ after τ at which the reaction takes place, then increase τ by $\Delta\tau$.

5. Recalculate the number of molecules and hence a_i and a.

The number of reiterations j depends on the timescale on which the evolution of the system should be followed.
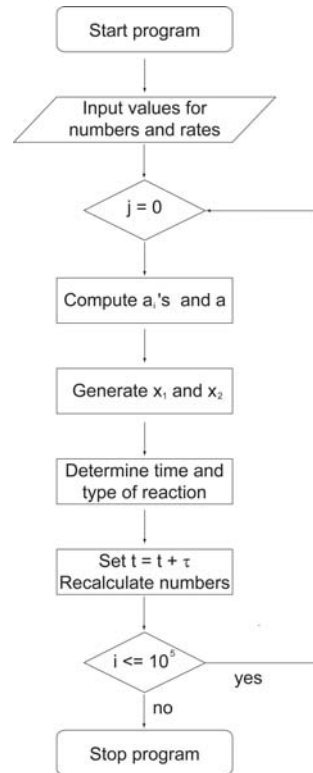
Figure 2.5: Flow chart of the Gillespie algorithm: the program needs initial values (number of molecules, reaction rates) and the number of reiterations j. With these probabilities for events, a_i, are computed. By drawing two random numbers x_1 and x_2 the event and its time of occurrence are determined. This is repeated j times, then the program ends.

Figure 2.6: Illustration of the correlation between the drawn number $x_1 \in \,]0;1]$ and resulting reaction r_i.

2.3.2   Gillespie's algorithm for the system at hand

The algorithm was implemented in the commercial program IgorPro 6.22A (Wavemetrics, Portland, OR, USA), which was also used to analyze previous experiments (Eckert et al., 2012a,b). The initial number of wild type monomers, n_{wt}, usually was chosen to be 1000 (in individual cases 5000 or 10000). If mutants were present, their initial monomer number varied between 0 and $10 \cdot n_{\mathrm{wt}}$. The number of iterations was chosen to be 10^5 (or $5 \cdot 10^5$ if the initial number of monomers was increased significantly). After each simulation the time traces of the resulting species of spastin (mono–, di–, tri–/tetra– and hexamers) were checked manually to ascertain that a steady state regime was reached, i.e. a constant concentration trace, and the requirements (amount of ATP release, population of intermediates) obtained from experiments by Eckert et al. (2012a) were fulfilled. For each set of parameters at least ten runs were performed for wild type only simulations and for mutant titrations at least three runs. The differences between these simulation runs were negligible, indicating no oscillations or bifurcation points.

The dynamic oligomerization process of spastin is a crucial part of the simulation (see chapter 3). The relative orientations of the two interacting molecules were taken into account, i.e. the molecule XY differs from YX and may have diverse forward and reverse rates. For higher oligomerization steps only the interface neighbors are important, that means the reactions $XX + YX$ and $YX + YY$ exhibit the same rates. This can be justified from the molecular perspective because the interaction only involves direct neighbors (see chapter 4.2).

The key value obtained from these simulations is the total ATP turnover rate into ADP. For this, the production of ADP per time was recorded and its slope fitted by a linear function. Only wild type subunits were allowed to hydrolyze with different rates, depending on the inhibition model chosen (see chapter 4.2). Mutant subunits were assumed not to hydrolyze at any time in the simulation. A crucial assumption in this simulation is that ATP is bound to the intermediates and is only hydrolyzed in a single step, when a hexamer dissociates into six monomers. This can be justified by energy conservation considerations: if each oligomerization step consumes one ATP but the resulting molecule is allowed to dissociate again, energy is wasted without any work performed by the enzyme. Hence the total ATP turnover rate per wild type subunit was derived from the number of wild type subunits incorporated in hexamers and their catalytic rate (see chapters 3.2 and

4.2) and is given by

$$k_{\text{obs/wt}} = \frac{k_{\text{catwt,f}} n_{\text{wt,f}} + k_{\text{catwt,i}} n_{\text{wt,i}}}{n_{\text{wt}}} \; , \tag{2.31}$$

where $k_{\text{catwt,f}}$ and $k_{\text{catwt,i}}$ denote the turnover rate of non-inhibited and inhibited wild type subunits, and $n_{\text{wt,f}}$ and $n_{\text{wt,i}}$ their respective amount. n_{wt} is the total number of wild type subunits defined in the simulation.

2.3.3 Analysis methods

The simulated data sets were analyzed and fitted by the following equations according to the respective models.

2.3.3.1 Michaelis-Menten fit

For wild type only simulations the goal was to obtain the catalytic turnover rate k_{cat} and the Michaelis-Menten constant K_{m}, which gives the substrate concentration at which the maximal turnover K_{max} is at half maximum. As in the experiments performed by Eckert et al. (2012a) the data were fitted by the Michaelis-Menten curve given by Fersht (1984)

$$k_{\text{obs}} = \frac{k_{\text{cat}} \cdot x}{K_{\text{m}} + x} \; , \tag{2.32}$$

where x is the wild type concentration. The on and off rates were varied in such a way that k_{obs} of the wild type titration saturated at a value very close to the one obtained in experiments (Eckert et al., 2012a).

2.3.3.2 Fitting models for inhibition schemes

In experiments where mutants were present their inhibitory behavior was analyzed. For this the number of mutant subunits was titrated at a set amount of wild type (see chapter 4.2). Two fitting models were studied: a binomial model and a non-competitive inhibition model. It has been shown that the latter one fits the experimental data on spastin very well (Eckert et al., 2012a).

Non-competitive inhibition model

In non-competitive inhibitions the binding of substrates and inhibitors to the enzyme are independent of each other. Both can bind to the enzyme alone as well as to an enzyme-

substrate or enzyme-inhibitor complex. In this study the complex including the inhibitor and substrate is assumed to have a smaller turnover rate compared to the enzyme-substrate complex. The fit function for the non-competitive model is given by the equation (see chapter 4.3)

$$f(x) = \frac{n_{\text{wt}} \left(k_{\text{cat, ww}} \cdot K_{\text{i}} + k_{\text{cat, wm}} \cdot x \right)}{\left(K_{\text{m}} + n_{\text{wt}} \right) \left(K_{\text{i}} + x \right)} \ , \tag{2.33}$$

where n_{wt} denotes the fixed number of total wild type subunits inserted, K_{i} the concentration of mutant subunits at which the turnover rate is 50% of the non-inhibited k_{obs}, $k_{\text{cat, ww}}$ and $k_{\text{cat, wm}}$ the non-inhibited and inhibited turnover rates respectively. x corresponds to the number of mutants. Equation (2.33) is an extention from a formula given in the textbook of Fersht (1985), and is modified with respect to the inhibited turnover rate, which can differ from zero.

Binomial inhibition model

Classical consideration

The random assembly of wild type and mutant subunits into hexamers is described by a binomial distribution function. The probability of k incorporated mutants in a hexamer ($n = 6$) is therefore

$$P\left(k \right) = \binom{6}{k} p^k \left(1 - p \right)^{6-k} \ , \tag{2.34}$$

where the binomial coefficient is given by

$$\binom{6}{k} = \frac{6!}{k! \left(6 - k \right)!} \tag{2.35}$$

and the probability of encountering a mutant subunit is

$$p = \frac{c_{\text{mut}}}{c_{\text{wt}} + c_{\text{mut}}} \ . \tag{2.36}$$

If the wild type turnover activity is reduced by a certain threshold amount k_{limit} of mutants incorporated in the hexamer (e.g. at least two mutants are needed to reduce the activity to the level of the inhibited turnover rate, see figure 2.7), the observed turnover rate per
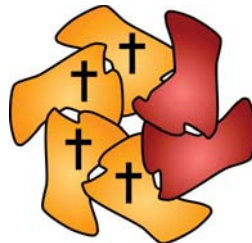
Figure 2.7: Threshold inhibition model: In this model it is assumed that a specific number of incorporated mutant subunits is needed to reduce the turnover activity of the wild type subunits to the basal level. In this scheme, at least two mutants are needed to induce inhibition. The position of the mutants in the hexamer is not important for the inhibition of all wild type subunits to occur.

hexamer is given by

$$k_{\text{obs}} = \frac{\sum_{k<k_{\text{limit}}} k_{\text{cat,ww}}}{k\binom{6}{k}p^k(1-p)^{6-k}} + \frac{\sum_{k>k_{\text{limit}}} k_{\text{cat,wm}}}{k\binom{6}{k}p^k(1-p)^{6-k}} \ . \tag{2.37}$$

Extended consideration

The classical considerations, however, do not distinguish between the amount of wild type and mutant subunits in the hexamer. This is an important issue as described in chapter (4.2). Therefore modifications were made, where the sum over the number of hexamers with one, two, etc. mutants is taken. The observed turnover rate is then computed via (see chapter 4.3)

$$k_{\text{obs}} = \frac{n_{\text{wt}}^5 k_{\text{cat, ww}} + \left(6dn_{\text{mut}}^4 + 15dn_{\text{mut}}^3 n_{\text{wt}} + 20dn_{\text{mut}}^2 n_{\text{wt}}^2 + 15dn_{\text{mut}} n_{\text{wt}}^3 + 6n_{\text{wt}}^4\right)dn_{\text{mut}} k_{\text{cat, wm}}}{6dn_{\text{mut}}^5 + 15dn_{\text{mut}}^4 n_{\text{wt}} + 20dn_{\text{mut}}^3 n_{\text{wt}}^2 + 15dn_{\text{mut}}^2 n_{\text{wt}}^3 + 6dn_{\text{mut}} n_{\text{wt}}^4 + n_{\text{wt}}^5} \ . \tag{2.38}$$

The factor d was introduced to take into account the possibility of different affinities between mutant and wild type (see chapter 4.3).

2.3.3.3 Pseudo-mono-molecular reaction scheme

For a rough approximation of K_{m} in the wild type only assembly the following reaction scheme (see figure 2.8) was used. The assumptions are that only the first reaction from E_1 to E_2 depends on the substrate concentration cS as well as the concentration of the educt E_1, while all subsequent steps only require the latter. Hence, the pseudo-mono-molecular

$$E_1 \xrightleftharpoons[k_{21}]{k_{12}} E_2 \xrightleftharpoons[k_{32}]{k_{23}} E_3 \xrightleftharpoons[k_{63}]{k_{36}} E_6 \xrightarrow{k_{cat}} 6\ E_1 + 6\ P$$
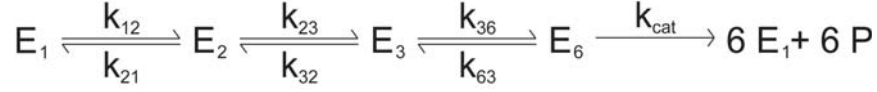
Figure 2.8: Pseudo-mono-molecular reaction scheme: only the reaction from state E_1 to E_2 is assumed to depend on the substrate concentration. All further reactions depend only on the concentration of the respective educt and the corresponding reaction rate.

reactions, neglecting higher orders, are given by the following set of equations:

$$\frac{d}{dt}cE_1(t) = -cS \cdot k_{12} \cdot cE_1(t) + k_{21} \cdot cE_2(t) + k_{cat,ww} \cdot cE_6(t)$$
$$\frac{d}{dt}cE_2(t) = cS \cdot k_{12} \cdot cE_1(t) - k_{21} \cdot cE_2(t) - k_{23} \cdot cE_2(t) + k_{32} \cdot cE_3(t)$$
$$\frac{d}{dt}cE_3(t) = k_{23} \cdot cE_2(t) - k_{32} \cdot cE_3(t) - k_{36} \cdot cE_3(t) + k_{63} \cdot cE_6(t) \tag{2.39}$$
$$\frac{d}{dt}cE_6(t) = k_{36} \cdot cE_3(t) - k_{cat,ww} \cdot cE_6(t) - k_{63} \cdot cE_6(t)$$
$$c_{total} = cE_1(t) + cE_2(t) + cE_3(t) + cE_6(t)\ ,$$

with k_{ij} the respective on and off rates, and cE_i the concentration of the intermediate state i. The solution for this set of equations is given by

$$
\begin{aligned}
cE_1(t) &= \frac{cE_{total}\left(k_{21}k_{32}k_{cat,ww} + k_{21}k_{36}k_{cat,ww} + k_{23}k_{36}k_{cat,ww} + k_{21}k_{32}k_{63}\right)}{\alpha} \\
cE_2(t) &= \frac{cE_{total}cS \cdot k_{12}\left(k_{32}k_{cat,ww} + k_{36}k_{cat,ww} + k_{32}k_{63}\right))}{\alpha} \\
cE_3(t) &= \frac{cE_{total}cS \cdot k_{12}k_{23}\left(k_{cat,ww} + k_{63}\right)}{\alpha} \\
cE_6(t) &= \frac{cE_{total}cS \cdot k_{12}k_{23}k_{36}}{\alpha} \\
\alpha &= k_{21}k_{32}k_{63} + k_{cat,ww}\left(k_{21}k_{32} + k_{21}k_{36} + k_{23}k_{36}\right) + \\
&+ cS \cdot \left[k_{12}k_{23}k_{36} + k_{12}k_{23}k_{63} + k_{12}k_{32}k_{63} + k_{cat,ww}\left(k_{12}k_{23} + k_{12}k_{32} + k_{12}k_{36}\right)\right]\ .
\end{aligned}
\tag{2.40}
$$

To calculate K_m, the maximal turnover rate

$$k_{max} = k_{cat,ww} \cdot cE_{6,max} \tag{2.41}$$

with

$$cE_{6,max} = \lim_{cS \to \infty} cE_6(t) \tag{2.42}$$

has to be known. As K_{m} is the concentration of cS with half maximum turnover rate, equation (2.41) has to be solved under these boundary conditions and one obtains

$$K_{\mathrm{m}} = \frac{k_{21}k_{32}k_{63} + k_{\mathrm{cat,ww}}\left(k_{21}k_{32} + k_{21}k_{36} + k_{23}k_{36}\right)}{k_{12}k_{23}k_{36} + k_{12}k_{23}k_{63} + k_{12}k_{32}k_{63} + k_{\mathrm{cat,ww}}\left(k_{12}k_{23} + k_{12}k_{32} + k_{12}k_{36}\right)} \ . \qquad (2.43)$$

It is important to note that this approximation is independent of the assembly pathway chosen (1-2-3-6 or 1-2-4-6, see chapter 3.2).

Chapter 3

Results I: Kinetics of the assembly pathway

The results in this chapter are subject of the publication [P1].

In the absence of ATP spastin is found as monomers, given proper salt concentrations. As outlined in chapter (1.2.3) its catalytically active form is assumed to be hexameric. This indicates that the dynamic oligomerization process is a part of spastin's kinetic cycle. Yet the pathway has not been elucidated with clear results so far, neither theoretically nor experimentally. In this chapter an experimental approach to investigate the oligomerization process using FCS is presented. Furthermore two assembly pathways are introduced, which are termed the 1-2-3-6 and 1-2-4-6 assembly pathway respectively. They are studied using the Gillespie algorithm presented in chapter (2.3.1). In all data shown in this chapter only wild type protein was used, the inclusion of mutant protein is presented in chapter (4).

3.1   Oligomerization studies using FCS

The dynamic oligomerization process of spastin takes place on a maximal timescale of seconds. Even though the exact times are unknown, this can be deduced from the experimental measurement of the catalytic turnover rate of four ATP per second and spastin wild type monomer [P1]. Traditional methods to detect different species, that is mono–, di–, ..., hexamers, present during oligomerization such as analytical ultracentrifugation, chemical cross-linking, size exclusion chromatography, etc. have a long run time which is in the order of several minutes. Therefore the detection of intermediary species is severely

hampered. Some of these techniques have provided some insight into the oligomerization process but for wild type spastin only monomers and dimers could be detected whereas no higher level wild type oligomers have been found (Eckert, 2012). This indicates that dimerization occurs and all further reactions have fast kinetic rates. Hence a detection method covering smaller timescales is needed.

As outlined in chapter (2.2.1) FCS is a suitable technique to study the diffusion coefficient and hence also diffusion time τ_D, and therefore also oligomerization because τ_D is proportional to the particle's size and the temporal resolution of FCS is in the order of ten seconds. Experiments were performed using pure wild type samples with an additional fluorophore (Atto488) at varying ATP concentrations. Histograms of the diffusion coefficient under differing conditions, which were obtained from fitting the auto-correlation function as described in chapter (2.2.1), were created (see figure 3.1).

In the case of no ATP being present, the histogram's width was relatively small with a peak around a diffusion coefficient of $0.8 \cdot 10^{-10}\,\mathrm{m^2 s^{-1}}$ (figure 3.1(a)). In order to test if this value is in agreement with the diffusion coefficient of a monomer an estimation using the sedimentation coefficient s obtained by analytical ultracentrifugation was performed. It has been shown that a monomer has the value $s_\mathrm{monomer} = 3.1 \cdot 10^{-13}\,\mathrm{s}$ and a hexamer $s_\mathrm{hexamer} = 7.6 \cdot 10^{-13}\,\mathrm{s}$ (White et al., 2007, Eckert, 2012). This then leads to a diffusion coefficient of $D_\mathrm{monomer} = 0.588 \cdot 10^{-10}\,\mathrm{m^2 s^{-1}}$ and $D_\mathrm{hexamer} = 0.24 \cdot 10^{-10}\,\mathrm{m^2 s^{-1}}$ (see equation 2.13). Even though the values for the monomers differ by about 25%, it is still in a reasonable agreement. This is due to the large uncertainty range during the measurement of the sedimentation coefficient s (Eckert, 2012).

In measurements with ATP, a shift from the well defined peak towards a small population of particles with a smaller diffusion coefficient can be observed (figures 3.1(b) and (c)), where a small number has a diffusion coefficient close to the value corresponding to a hexamer, which was extrapolated by applying the considerations above (about $0.2 \cdot 10^{-10}\,\mathrm{m^2 s^{-1}}$). The particles with diffusion coefficients in between correspond to the intermediate states. Furthermore a broadening of the main peak is visible. This corresponds to the overlap of the diffusion coefficient of monomers and dimers as they differ only by a factor of 1.4[1] and therefore cannot be resolved into two clearly distinct peaks. In addition to the intermediate diffusion coefficients, the decreasing number of particles diffusing through the focal volume over time (figure 3.1(d)) indicates an oligomerization process resulting in a higher oligomer level than dimers. The low amount of hexamers can

---

[1]The factor 1.4 results from equation (2.12) and the assumption that $r_\mathrm{dimer} = 2r_\mathrm{monomer}$.

(a) no ATP

(b) 0.5 mM ATP

(c) 1 mM ATP

(d) number of particles vs. time
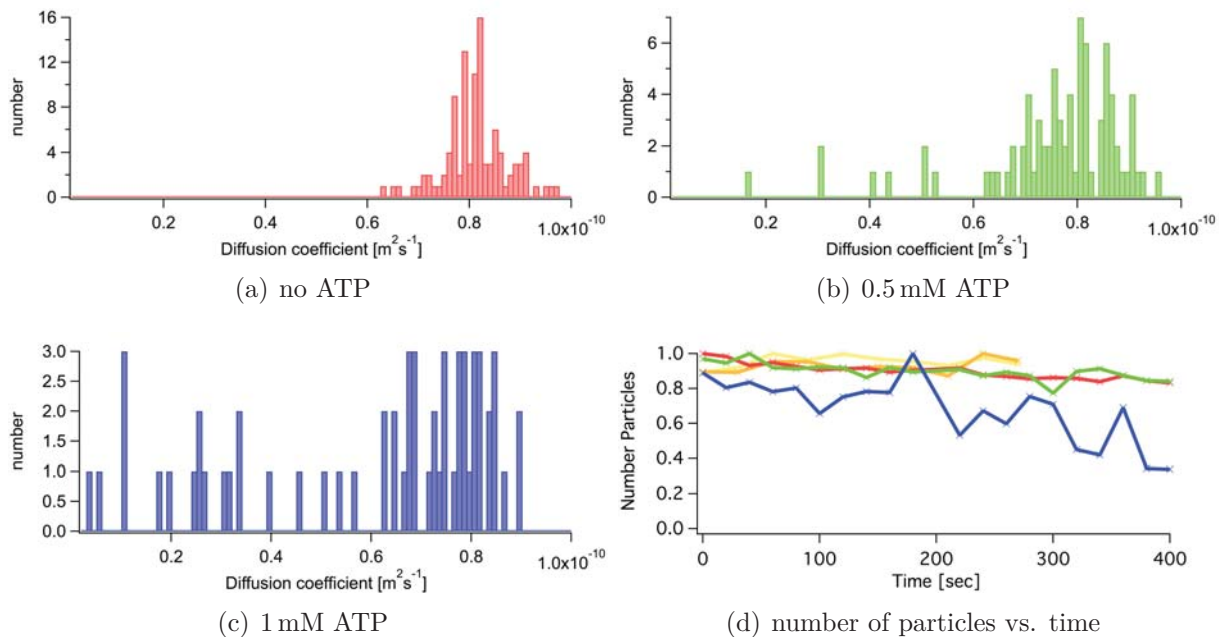
Figure 3.1: Experimental data obtained from FCS measurements. Panel (a) shows the diffusion coefficient of spastin without ATP, (b) and (c) with 0.5 mM and 1 mM ATP respectively. It can be seen that with the addition of ATP some particles show a lower diffusion coefficient. In panel (d) the normalized amount of spastin diffusing through the confocal volume is displayed as a function of measurement time. It can be seen that only at high concentrations of ATP the number of particles diffusing through the confocal volume is reduced significantly, indicating oligomerization in the course of the measurement. The concentration of spastin was 10 nM. The orange and yellow graph are control measurements with fluorophore (Atto488) only.

be explained by the small concentration of spastin (about 10 nM) present in the sample.

3.2 Implemented pathways

The described experiment and further observations by Eckert (2012) suggest a minimal reaction scheme for spastin, which can be described as shown in figure (3.2). Two monomers build a dimer with on-rate k_{12}. This reaction is reversible with the rate k_{21}. Here the oligomerization from dimers into hexamers is regarded as one collective reaction with the rate k_{26}. When a hexamer is formed it can either disassemble with k_{62} or hydrolyze with the rate k_{cat} with the simultaneous disassembly into six monomers. As ATP is assumed to be at saturating concentrations, its binding to the enzyme does not need to be modeled as a bi-molecular reaction. It is important to mention that the binding of ATP is not specified to any step, i.e. it can bind either during the individual oligomerization steps or a collective
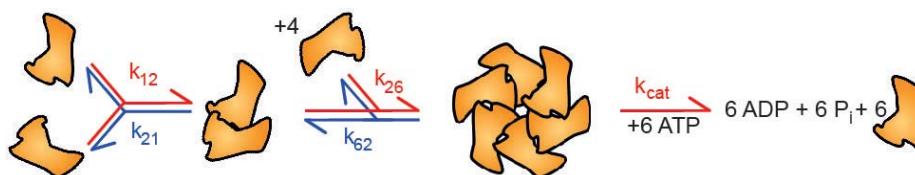
Figure 3.2: Minimal reaction scheme for a dynamical hexamerization process, suggested by the FCS experiments. The dimerization occurs at the encounter of two monomers. The hexamerization is assumed to occur at one collective reaction. The hexamer can either disassemble with the rate k_{62} or hydrolize with the rate k_{cat}.

binding of six ATP to the formed hexamer can occur. Hydrolyzation of all bound ATPs is assumed to take place at once, but only during the catalytic step of a hexamer including its disassembly into monomers. This can be justified by energy considerations: if each oligomerization step depletes one ATP but the resulting molecule is allowed to dissociate again, energy is wasted without any work performed by the enzyme.

The described minimal scheme needs to be extended as the assembly from a dimer into a hexamer by the assumed collective binding of four monomers is not realistic. The probability of the encounter of five molecules at the same place and time is negligible. This leads to the conclusion that intermediate oligomers must occur and play an important role for the hexamerization process. Many different possible pathways can be thought of. One is the sequential addition of monomers to a partially assembled oligomer, which will be termed 1-2-3-4-5-6 pathway. This hexamerization process includes five different reactions with six pools of diverse oligomer species (figure 3.3). However, the subunits of these species are identical, and hence the interactions between intermediates are expected to occur (Gutfreund, 1995). This reduces the number of different reaction steps which are needed for the assembly of a hexamer. The number of reactions is always five, but the number of different reaction types can be smaller, see figure (3.3).

Two possible pathways with the minimal amount of different reaction types are shown in figures (3.3(b)) and (c) which are denoted the 1-2-3-6 and 1-2-4-6 pathway respectively. Both have the initial dimerization process in common but differ later on. The first assumes that dimers form trimers, under the use of another monomer, and that two trimers then react to a hexamer. The latter pathway uses two dimers to build a tetramer and then a further dimer to construct a hexamer. In principle a mixture of both pathways is possible which would result in up to nine different reactions (see figure 3.3, with a further reaction between trimers and dimers). As the two pathways presented here have the minimal number of reactions, they require the least amount of different oligomeric intermediates.

This is a crucial aspect as all forward rates depend on the concentrations of the reaction partners. That in turn means that the reactions only occur if a sufficient amount of the intermediates is at hand.

A quantitative description of the assembly process is complicated, even using the minimal pathways described above. From the reaction scheme presented in figure (3.3) and the conservation of mass, the rate equations can be derived which describe the temporal development of the system. The 1-2-3-6 pathway is described by

$$
\begin{aligned}
\frac{\mathrm{d}}{\mathrm{d}t}c_1 &= 2k_{21}c_2 + k_{32}c_3 + 6k_{\mathrm{cat}}c_6 - 2k_{12}c_1^2 - k_{23}c_1c_2 \\
\frac{\mathrm{d}}{\mathrm{d}t}c_2 &= k_{12}c_1^2 + k_{32}c_3 - k_{21}c_2 - k_{23}c_1c_2 \\
\frac{\mathrm{d}}{\mathrm{d}t}c_3 &= k_{23}c_1c_2 + 2k_{63}c_6 - k_{32}c_3 - 2k_{36}c_3^2 \\
\frac{\mathrm{d}}{\mathrm{d}t}c_6 &= k_{36}c_3^2 - k_{63}c_6 - k_{\mathrm{cat}}c_6
\end{aligned}
\tag{3.1}
$$

and the 1-2-4-6 pathway by

$$
\begin{aligned}
\frac{\mathrm{d}}{\mathrm{d}t}c_1 &= 2k_{21}c_2 + 6k_{\mathrm{cat}}c_6 - 2k_{12}c_1^2 \\
\frac{\mathrm{d}}{\mathrm{d}t}c_2 &= k_{12}c_1^2 + 2k_{42}c_4 + k_{64}c_6 - 2k_{24}c_2^2 - k_{46}c_2c_4 - k_{21}c_2 \\
\frac{\mathrm{d}}{\mathrm{d}t}c_4 &= k_{24}c_2^2 + k_{64}c_6 - k_{46}c_2c_4 - k_{42}c_4 \\
\frac{\mathrm{d}}{\mathrm{d}t}c_6 &= k_{46}c_2c_4 - k_{64}c_6 - k_{\mathrm{cat}}c_6 \;,
\end{aligned}
\tag{3.2}
$$

where c_i denotes the number of oligomers in state i, k_{ij} and k_{ji} the respective forward and reverse rates between the states i and j. The importance of the pools of monomers and dimers is obvious in equation (3.1) and (3.2) respectively. They are needed to induce the sequential reactions. The concentrations of free subunits contribute to the equations linearly and quadratically, depending on the oligomerization step. This leads to a set of five coupled, non-linear equations which cannot be solved analytically. One way to solve this problem is numerical calculations. It has been shown that in finite systems with a capped maximal size of oligomers the numerical solution in general is not accurate and hence stochastic simulations are needed especially in the regime of steady state concentration (D'Orsogna et al., 2012, Yvinec et al., 2012).

In simulations with only wild type subunits, the main goal was to model the ATP
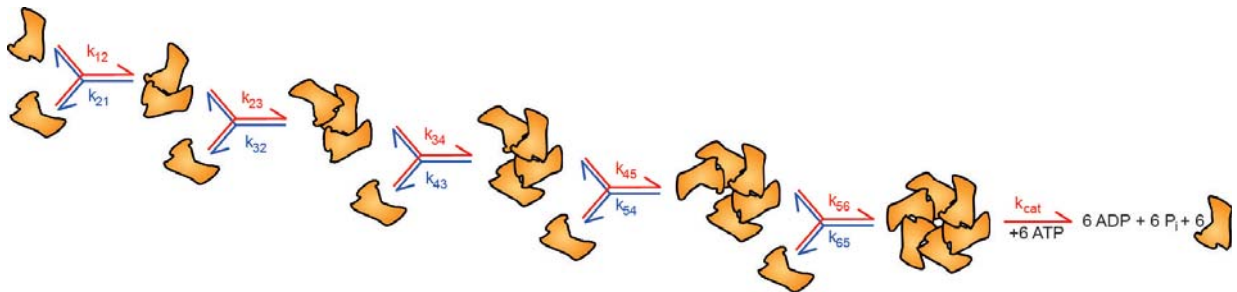
(a) 1-2-3-4-5-6 pathway
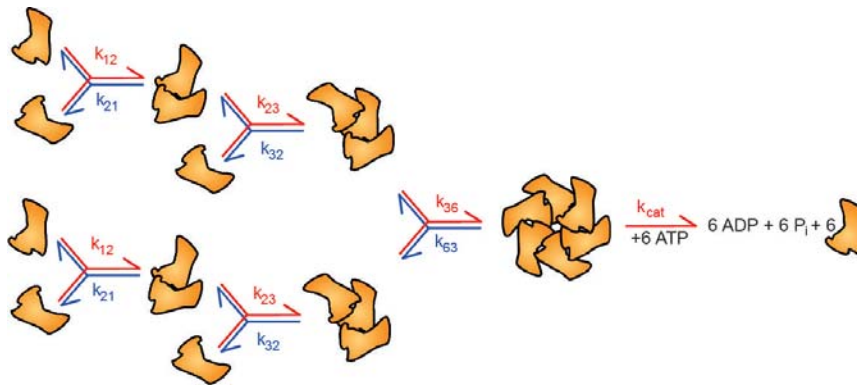
(b) 1-2-3-6 pathway
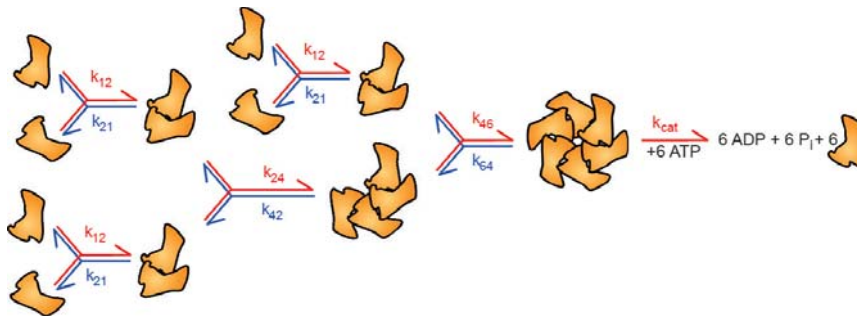
(c) 1-2-4-6 pathway

Figure 3.3: Assembly pathways: panel (a) shows the 1-2-3-4-5-6 assembly pathway, which needs five oligomerization steps with five different reactions to form a hexamer. Panels (b) and (c) display two alternative pathways with five steps as well, but only three different reactions, and are denoted 1-2-3-6 and 1-2-4-6 pathway respectively.

reaction	forward rates	reverse rates
2 monomers ↔ dimer	$k_{12} = 0.01$	$k_{21} = 10$
dimer + monomer ↔ trimer	$k_{23} = 0.1$	$k_{32} = 10$
2 dimers ↔ tetramer	$k_{24} = 0.1$	$k_{42} = 10$
2 trimers ↔ hexamer	$k_{36} = 0.5$	$k_{63} = 10$
tetramer + dimer ↔ hexamer	$k_{46} = 0.5$	$k_{64} = 10$
catalytic step (hexamer → 6 monomers)	$k_{cat} = 5.0$	n.a. (irreversible)

Table 3.1: Set of default parameters which were used in the simulation. They were optimized for the 1-2-4-6 pathway and fulfilled all requirements given by experimental observations.

turnover rate in dependence of inserted enzyme, which has been shown to saturate in experiments (Eckert et al., 2012a). To match further experimental observations, the following requirements have to be fulfilled: the concentration of monomers at reaction equilibrium has to be kept as high as possible. Furthermore the number of dimers should be larger than the number of trimers or tetramers. These restrictions were fulfilled when the dimerization with the rate k_{12} was chosen to be the slowest step, whereas all further oligomerization reactions ran faster. The catalytic rate[2] k_{cat} had to be set slightly higher (about 20%) than the experimentally determined value k_{max}. The default parameter set (see table 3.1) was optimized for the 1-2-4-6 pathway and fulfilled all requirements (figure 3.4(b)). When using the same parameters in the 1-2-3-6 pathway, the population of trimers exceeds the one of dimers slightly (figure 3.4(a)). This can be explained by the fact that trimerization depends not only on the concentration of dimers but also on the concentration of monomers. Apart from this the maximal turnover rates and distributions of monomers and hexamers are comparable for both assembly pathways (see figure 3.4).

As the observed value for k_{obs} depends on the amount of enzyme, the simulation was performed with various total amounts of monomer units while the parameter set of forward and reverse rates was not changed. The data of ten runs for each concentration and the default forward and reverse rates are shown in figures (3.5(a)) and (b) for the 1-2-3-6 and 1-2-4-6 pathway respectively. It can be seen that the different iterations, using the same parameter set, result in nearly indistinguishable values for k_{obs}. The plot of k_{obs} vs. the increasing number of subunits bears resemblance to a Michaelis-Menten kinetics. The data were fitted using equation (2.32), which results in the continuous curve in figures (3.5(a)) and (b)). However, the residuals of the fits display a systematic deviation, indicating that

---

[2]Note: k_{obs} is the turnover rate at a given substrate concentration under specific conditions, k_{max} is the extrapolated maximal turnover rate and k_{cat} is the parameter inserted into the simulation as the rate of the catalytic step.

(a) 1-2-3-6 pathway

(b) 1-2-4-6 pathway
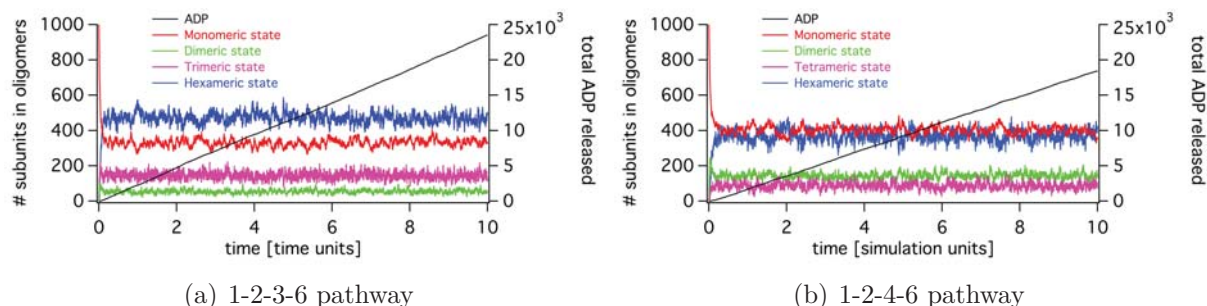
Figure 3.4: Simulation of hydrolyzation by wild type. The curves (left scale) show the evolution of the population of oligomeric states, corresponding to the assembly pathway. Red denotes monomers, green dimers, pink trimers or tetramers respectively, and blue hexamers. The initial value for wild type subunits was 1000. The black line is the ADP release, the amount given on the right scale.

(a) 1-2-3-6 pathway

(b) 1-2-4-6 pathway
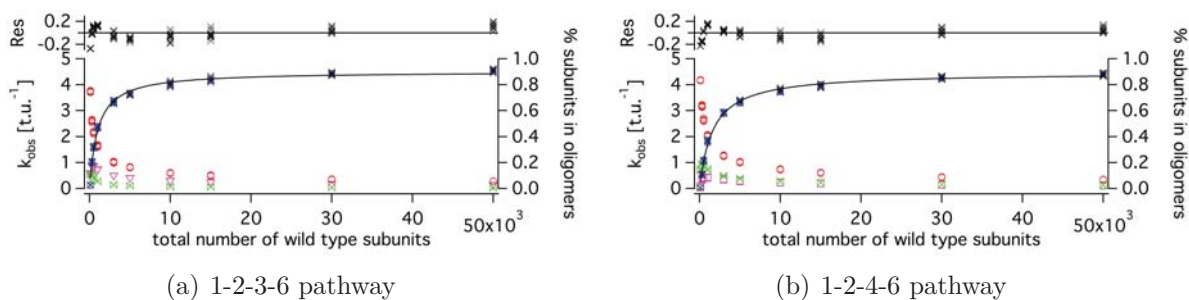
Figure 3.5: The turnover rate k_{obs}, given in inverse time units $[\mathrm{t.u.}^{-1}]$, is displayed as a function of the total number of wild type subunits inserted into the simulation. The data were fitted using the Michaelis-Menten equation (black curve). The left scale shows the amount of ATP hydrolyzed by a monomer, denoted as black crosses in the graph. The residuals (Res) displayed above show the deviation of the Michaelis-Menten fit from the data. The graphs also show the percentage distribution of the oligomeric population, on the right axis. Red circles represent monomers, green double-triangles dimers, pink triangles and squares trimers and tetramers respectively, and blue hexagons hexamers.

the system is not accurately described by the Michaelis-Menten model. This result is not surprising as the hexamerization process is non-linear and hence involves reactions of higher order than the first order assumed in the Michaelis-Menten model. Nevertheless, the value of the half-maximal activation constant K_m computed using a pseudo-mono-molecular reaction (equation 2.43) is close to the number of particles at which the simulation reached $k_{obs} = 0.5 \, k_{cat}$, which is $2.5 \, \mathrm{s^{-1}}$ for the default parameters. K_m in the 1-2-3-6 pathway was found to be $K_{m,1236} = 1008 \pm 25$ particles, in the 1-2-4-6 pathway $K_{m,1246} = 1645 \pm 38$ particles and in the pseudo-mono-molecular model $K_{m,pmm} = 990$, slightly lower than found in the simulations.

In addition to the turnover rate k_{obs}, figure (3.5) displays the fraction of wild type subunits incorporated in the respective oligomeric states, depending on the assembly pathways. The courses of the intermediates show that the requirements defined previously (concentration of monomers are kept as high as possible, concentration of dimers larger than higher intermediates) are fulfilled over a large range of concentrations. Furthermore it is shown that the amount of wild type subunits incorporated in hexamers is directly proportional to k_{obs}. This observation is in accordance with the assumption that hexamers are the only catalytically active species.

With the data obtained so far, a comparison of the two assembly pathways can be made. From figure (3.5) some conclusions can be drawn: in the 1-2-3-6 pathway the turnover rate k_{obs} shows a steeper dependency on the number of subunits, and K_m has a smaller value compared to the 1-2-4-6 pathway. In addition, the 1-2-3-6 pathway favors the population of trimers at the expense of dimers and also of free monomers, which are consumed by both dimerization and trimerization. This leads to the conclusion that the formation of a large trimeric population is an essential step in this assembly pathway.

In contrast, the 1-2-4-6 assembly pathway shows a higher amount of dimeric intermediates than tetrameric ones, and also the pool of monomers is higher than in the 1-2-3-6 pathway. This can be deduced from the two reactions driven by a high concentration of dimers, which is the key population in the 1-2-4-6 pathway.

To study the influence of the oligomerization rates k_{12}, k_{23}, k_{24}, k_{36}, k_{46}, and k_{cat} on the equilibrium concentrations of the intermediates and k_{obs}, these values were increased individually by a factor of 100. The resulting simulations are presented in figure (3.6) and the fitted values for K_{cat} and K_m are given in table (3.2). Increasing the dimerization rate k_{12} in both pathways results in an increase of the dimeric population and a significant reduction of the monomeric one. In the 1-2-3-6 pathway the trimer population was also

increased. The values of K_m obtained from the simulations and from the pseudo-mono-molecular model differ significantly, demonstrating the utmost importance of the initial non-linear oligomerization step.

The increase of the forward rates in the 1-2-3-6 pathway compared to the default parameter set can be explained as follows: the higher value for the trimerization reaction reduces the number of monomers, and the number of dimers nearly vanishes. These species are consumed by the formation of trimers. Compared to the default parameter set the resulting K_m is reduced by a factor of two, again showing the important role of trimers. The increase of the hexamerization rate obviously reduces the number of trimers present and increases the pool of free monomers. Furthermore, at low concentrations of subunits the dimerization step is rate-limiting. K_m is also reduced by a factor of two.

In the 1-2-4-6 pathway the results of 100 times higher forward rates are the following: increasing the tetramerization rate results in a larger population of tetramers at the expense of dimers. K_m was increased by 12%. A higher hexamerization rate results in a reduced pool of tetramers, especially at low numbers of subunits, leading to the pool of tetramers being rate limiting. K_m is reduced by one third.

These variations demonstrate that a change in the rates of reaction of quadratic order leads to a significant deviation of the resulting K_m compared to the value of K_m obtained from the pseudo-mono-molecular model. Hence the reactions of second order (e.g. dimerization) cannot be simplified as it has been done so far in the literature.

In either pathway, increasing k_{cat} leads to a lower population of hexamers in favor of free monomers due to the catalytic step. Furthermore the number of the crucial intermediates (trimers and dimers respectively) are increased due to the higher amount of monomers present. Due to limited computational power, the simulation could not be continued to a significantly higher amount of initial subunits, which would be necessary to observe the saturation of k_{obs}.

3.3   Application of the simulation to experimental data

In order to elucidate the assembly pathway of spastin, data obtained from experiments and simulations were compared. The concentration of wild type used in experiments was converted into the number of wild type particles used in simulation such that the scales of titration were consistent. The turnover rate k_{obs} was obtained from experiments without the addition of microtubules and hence is lower than the simulated turnover rate k_{max}.

1-2-3-6 assembly pathway   1-2-4-6 assembly pathway

(a) default

(b) default

(c) $100 \cdot k_{12}$

(d) $100 \cdot k_{12}$

(e) $100 \cdot k_{23}$

(f) $100 \cdot k_{24}$

(g) $100 \cdot k_{36}$

(h) $100 \cdot k_{46}$

(i) $100 \cdot k_{cat}$

(j) $100 \cdot k_{cat}$
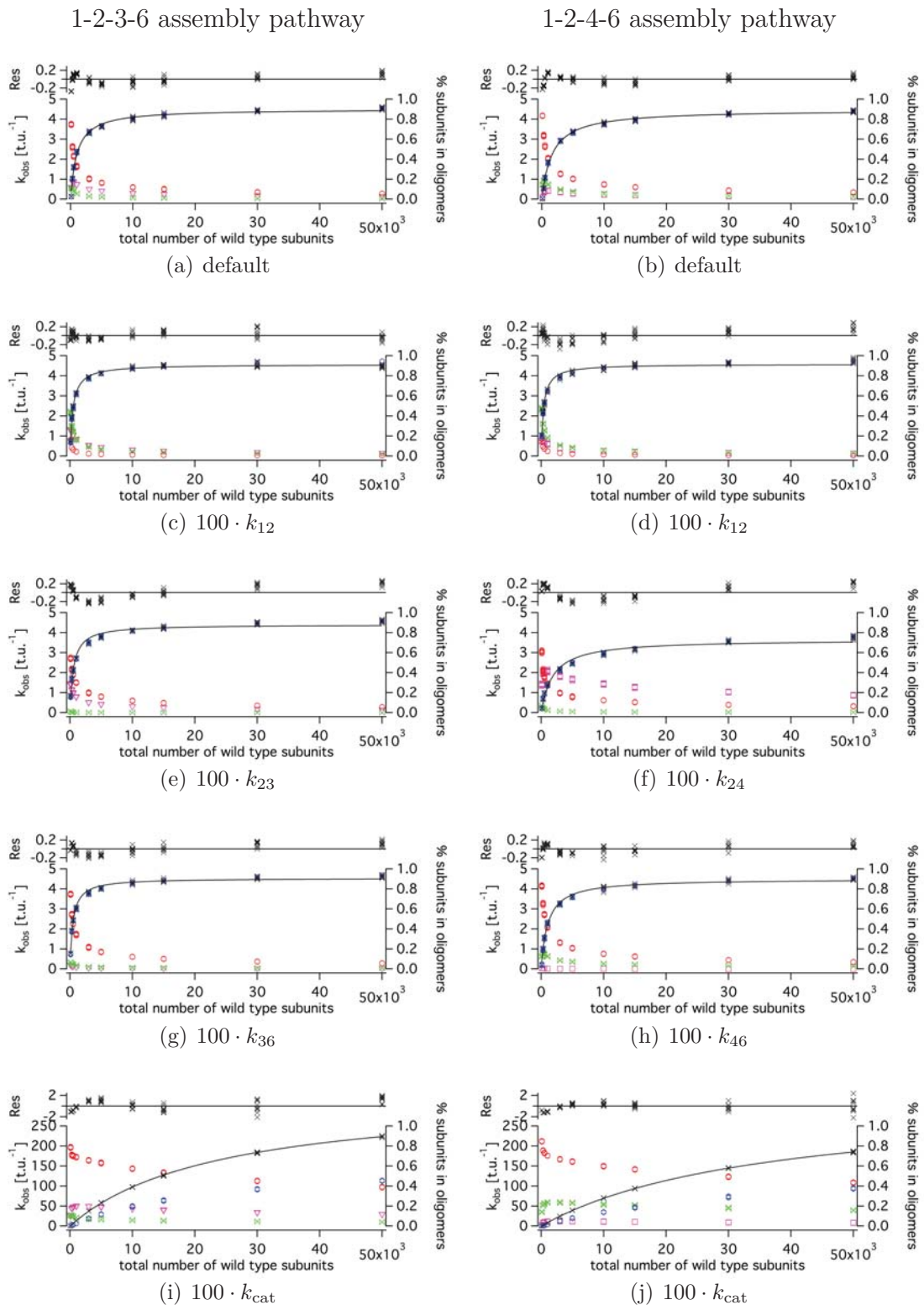
Figure 3.6: Resulting k_{max} from simulations with different initial parameters, where the default values were multiplied by a factor of 100. The left and right panels show the 1-2-3-6 and 1-2-4-6 assembly respectively. Labeling is analog to fig (3.5). It can be seen that the value for K_m is altered. Furthermore the distributions of intermediate populations are affected by the respective forward rates.

parameter set	**1-2-3-6**			pseudo-mono-molecular	**1-2-4-6**		
	k_{cat}	K_{m}	δK_{m}	K_{m}	k_{cat}	K_{m}	δK_{m}
default	4.5	1008	25	990	4.5	1645	38
$100 \cdot k_{12}$	4.6	451	7	9.9	4.6	346	9
$100 \cdot k_{23(24)}$	4.4	557	17	504	3.7	1858	77
$100 \cdot k_{36(46)}$	4.5	458	9	990	4.5	1060	22
$100 \cdot k_{\text{cat}}$	330	23846	160	991	318	35901	271

Table 3.2: Comparison of the Michaelis-Menten constant K_{m} obtained from the fitting of the oligomerization simulation and the one calculated by the pseudo-mono-molecular reaction. δK_{m} denotes the standard error of the fit.

(a) 1-2-3-6 pathway
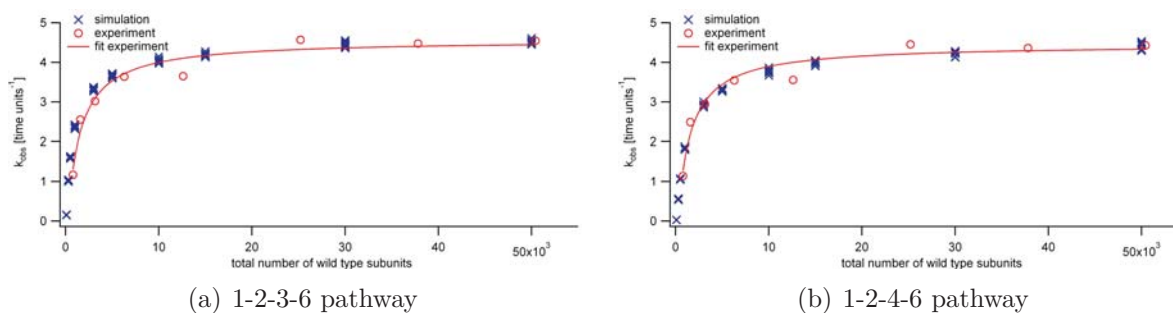
(b) 1-2-4-6 pathway

Figure 3.7: The results obtained from experiments (red circles) and simulations (blue crosses) are compared. Even though both simulated assembly pathways reflect the experimental data equivalently well, the 1-2-4-6 pathway is best when regarding the Michaelis-Menten fit of the experimental data.

These values were adjusted such that the values in saturation were consistent (figure 3.7).

The experimental data obtained from T. Eckert [P1] show a strong dependency of the apparent turnover rate of spastin on its concentration. Hence the activation shows a positive correlation to the enzyme concentration and could be fitted by a Michaelis-Menten hyperbola. The simulated data presented here are in good agreement with this behavior, both for the 1-2-3-6 and 1-2-4-6 assembly pathway. As experiments at low enzyme concentrations tend to be very noisy, only limited experimental data points could be recorded in in this regime in [P1]. Therefore unfortunately the assembly pathway cannot be elucidated in more detail and no definitive answer on the assembly pathway of spastin can be made.

Chapter 4

Results II: Mutant inhibition schemes and fit models

The results in this chapter are subject of the publications [P1] and [P3].

In classical textbooks, inhibition schemes are treated as a competition of two different substrates, one of which is an inhibitor for binding sites of an enzyme in its wild type state. This however does not account for all the cases of hereditary spastic paraplegia. Gene products from intact and defective alleles can be co-expressed and these proteins can co-assemble into a complex, where the mutant gene product inhibits the proper function of the wild type protein.

It has been shown that some patients show a mutation in the gene at E442Q. This has been investigated in [P3]. The coupled enzyme ATPase assay reported there was performed at a constant concentration of wild type spastin, where the concentration of the mutant was increased. The addition of the mutant reduced the turnover rate of wild type subunits, which points to a physical interaction of wild types and mutants. In this biochemical assay, performed by T. Eckert, the addition of 20% mutant spastin led to a reduction of the wild type turnover rate by 50%. When performing a microscopic severing assay (T. Eckert), the inhibitory effect was even more prominent as only 5% mutant was sufficient to reach the same inhibition level. This shows that inactive mutant subunits of AAA proteins inhibit the activity of wild type enzymes, and also demonstrates that both enzyme types form hetero-oligomers.

(a) wild type – wildtype (b) wild type – mutant (c) mutant – wild type (d) mutant – mutant
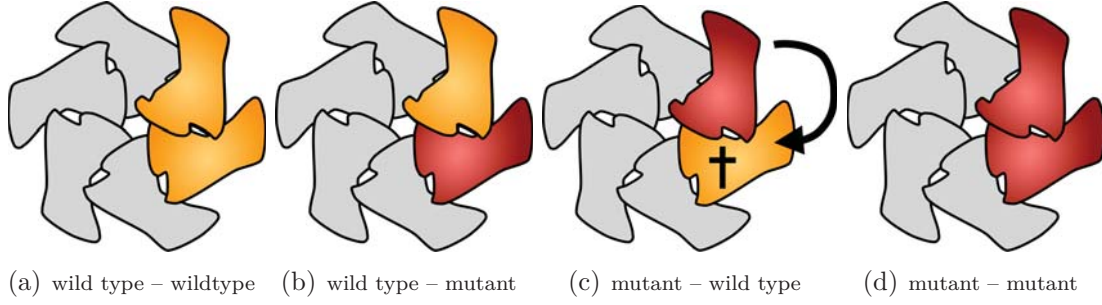
Figure 4.1: Nearest-neighbor inhibition model: one mutant subunit inhibits one wild type subunit, which in this case is assumed to be his direct neighbor. For the inhibition to occur, the two subunits have to display a specific orientation with respect to each other. Here the left neighbor is inhibited. Panels (a) and (b) show no inhibition, panel (c) depicts the inhibited wild type subunit, and panel (d) shows the configuration of two mutant subunits, which has no catalytic activity.

4.1 Nearest neighbor inhibition scheme

A first attempt to describe this inhibitory behavior was to consider only the interaction of any two subunits, possibly neighbors, in a hexamer (see figure 4.1). Furthermore this scheme assumes orientated inhibition, where the mutant can only inhibit one wild type subunit that assumes a specific orientation with respect to the mutant. Without loss of generality, the wild type subunit is now assumed to be the direct neighbor on the left. The ATP turnover rate is given by

$$k_{\text{obs}} = \frac{k_{\text{cat,ww}}c_{\text{ww}} + k_{\text{cat,wm}}c_{\text{wm}}}{c_{\text{w,total}}} \; , \tag{4.1}$$

where $k_{\text{cat},wx}$ is the catalytic turnover rate of wild type subunits, which have an oriented neighbor x (that can either be a mutant or a wild type subunit), c_{wx} is the respective concentration at equilibrium, and $c_{\text{w,total}}$ denotes the total concentration of wild type enzyme in the assay. The mutant is considered to be catalytically incapable, therefore $k_{\text{cat,m}} = 0$. This is also assumed to be true if a mutant has a wild type neighbor to the right ($k_{\text{cat,mw}} = 0$). The total concentration of wild type is given by

$$c_{\text{w,total}} = 2c_{\text{ww}} + c_{\text{wm}} + c_{\text{mw}} + c_{\text{w}} \; , \tag{4.2}$$

with c_{w} the concentration of free wild type monomers at equilibrium. As the orientation within the dimer is important in this scheme, c_{wm} and c_{mw} can differ and hence have to be

treated separately. The law of mass action for dimerization gives the affinity constants

$$
\begin{aligned}
K_{\mathrm{a,ww}} &= \frac{c_{\mathrm{ww}}}{c_{\mathrm{w}}^2} \\
K_{\mathrm{a,wm}} &= \frac{c_{\mathrm{wm}}}{c_{\mathrm{w}} c_{\mathrm{m}}} \\
K_{\mathrm{a,mw}} &= \frac{c_{\mathrm{mw}}}{c_{\mathrm{w}} c_{\mathrm{m}}} \\
K_{\mathrm{a,mm}} &= \frac{c_{\mathrm{mm}}}{c_{\mathrm{m}}^2} \ ,
\end{aligned}
\tag{4.3}
$$

where c_{m} indicates the concentration of free mutant monomers at equilibrium. Using equations (4.2) and (4.3), equation (4.1) can be rewritten as

$$
k_{\mathrm{obs}} = \frac{k_{\mathrm{cat,ww}} c_{\mathrm{w}} K_{\mathrm{a,ww}} + k_{\mathrm{cat,wm}} c_{\mathrm{m}} K_{\mathrm{a,wm}}}{2 c_{\mathrm{w}} K_{\mathrm{a,ww}} + c_{\mathrm{m}} \left(K_{\mathrm{a,wm}} + K_{\mathrm{a,mw}} \right) + 1} \ .
\tag{4.4}
$$

With equation (4.2), the equilibrium concentration of wild type monomers can be computed, and analogously also for the mutant concentrations:

$$
\begin{aligned}
c_{\mathrm{w}} &= c_{\mathrm{w,total}} - 2 c_{\mathrm{ww}} - c_{\mathrm{wm}} - c_{\mathrm{mw}} \\
c_{\mathrm{m}} &= c_{\mathrm{m,total}} - 2 c_{\mathrm{mm}} - c_{\mathrm{wm}} - c_{\mathrm{mw}}
\end{aligned}
\tag{4.5}
$$

where equation (4.4) becomes

$$
k_{\mathrm{obs}} = \frac{a + b + c}{d}
\tag{4.6}
$$

with

$$
\begin{aligned}
a &= k_{\mathrm{cat,ww}} c_{\mathrm{w,total}} K_{\mathrm{a,ww}} - 2 k_{\mathrm{cat,ww}} c_{\mathrm{w}}^2 K_{\mathrm{a,ww}}^2 \\
b &= -2 c_{\mathrm{m}} c_{\mathrm{w}} K \left(k_{\mathrm{cat,ww}} K_{\mathrm{a,ww}} + k_{\mathrm{cat,wm}} K_{\mathrm{a,wm}} \right) \\
c &= 2 c_{\mathrm{m}}^2 k_{\mathrm{cat,wm}} K_{\mathrm{a,wm}} K_{\mathrm{a,mm}} + c_{\mathrm{m,total}} k_{\mathrm{cat,wm}} K_{\mathrm{a,wm}} \\
d &= 1 + 2 c_{\mathrm{m,total}} K - 4 c_{\mathrm{m}}^2 K_{\mathrm{a,mm}} K - 4 c_{\mathrm{m}} c_{\mathrm{w}} K^2 \\
&\quad - 4 c_{\mathrm{m}} c_{\mathrm{w}} K_{\mathrm{a,ww}} K + 2 c_{\mathrm{w,total}} K_{\mathrm{a,ww}} - 4 c_{\mathrm{w}}^2 K_{\mathrm{a,ww}}^2 \ ,
\end{aligned}
\tag{4.7}
$$

and for simplification

$$
2K = K_{\mathrm{a,wm}} + K_{\mathrm{a,mw}} \ .
\tag{4.8}
$$

Here possible variations in the assembly rates of mutant-wild type and wild type-mutant are neglected. In the limit of infinite concentrations for inserted wild type and mutants,

the concentration of free monomers will decrease to zero[1], and hence equation (4.6) is simplified to

$$k_{\text{obs}} \approx \frac{k_{\text{cat,ww}}c_{\text{w,total}}K_{\text{a,ww}} + k_{\text{cat,wm}}c_{\text{m,total}}K_{\text{a,wm}}}{2c_{\text{w,total}}K_{\text{a,ww}} + 2c_{\text{m,total}}K + 1} \ . \tag{4.9}$$

This inhibition scheme using mutant subunits as inhibitors is similar to a model that considers competing substrates. Hence the experimental data can be fitted by

$$k_{\text{obs}} = \frac{\frac{k_{\text{cat,ww}}c_{\text{w,total}}}{K_{\text{d,ww}}} + \frac{k_{\text{cat,wm}}c_{\text{m,total}}}{K_{\text{d,wm}}}}{2\frac{c_{\text{w,total}}}{K_{\text{d,ww}}} + 2\frac{c_{\text{m,total}}}{K^{-1}} + 1} \ , \tag{4.10}$$

since $K_{\text{d}} = K_{\text{a}}^{-1}$.

This strongly simplified dimerization inhibition scheme fits the experimental data very well (black line in figure 4.2). Also the fit values for $k_{\text{cat,ww}}$ are in very good agreement with the experimental data ($k_{\text{cat,ww,exp}} = 3.83\,\text{s}^{-1}$ and $k_{\text{cat,ww,fit}} = 3.45\,\text{s}^{-1}$ for measurements with microtubules, and $k_{\text{cat,ww,exp}} = 1.92\,\text{s}^{-1}$ and $k_{\text{cat,ww,fit}} = 0.78\,\text{s}^{-1}$ without microtubules).

As an alternative inhibition scheme a random distribution of mutant subunits in the hexamer was considered. This scheme assumes that a minimum threshold number of mutant subunits is necessary to reduce the catalytic activity of a hexamer. The principle of the fitting function was already introduced and derived in chapter (2.3.3) and results in equation (2.36). Even though this binomial scheme requires hexamerization to occur, it fails to reflect the experimental data, as shown by the gray lines in figure (4.2).

4.2 Modeling mutant inhibition

The nearest-neighbor inhibition scheme fits the experimental data for the inhibitory effect of increasing mutant concentration on the catalytic turnover of wild type spastin at a fixed concentration very well. However, it is limited to two of the six subunits of a hexamer. As the catalytically active form of spastin is generally assumed to be a hexamer, the scheme above does not reflect this situation. One possibility to achieve a more detailed description of the system would be, as outlined in chapter (3.2), to solve a set of rate equations similar to equations (3.1) and (3.2). However, the case at hand is more complicated as not only wild type but also mutants are present, resulting in a larger set of coupled

---

[1]The simplified case of wild type dimerization is calculated here (the consideration is analogous with mutants), where the subscript "eq" denotes the concentration at equilibrium: with $K_{\text{a}} = \frac{c_{\text{wtwt,eq}}}{c_{\text{wt,eq}}}$ and $c_{\text{w,total}} = c_{\text{w,eq}} + c_{\text{ww,eq}}$ one obtains $c_{\text{ww,eq}} = \frac{1}{8}\left(4c_{\text{w,total}} + \frac{1}{k_{\text{a}}} - \sqrt{\frac{1 + 8c_{\text{w,total}}K_{\text{a}}}{k_{\text{a}}}}\right)$.
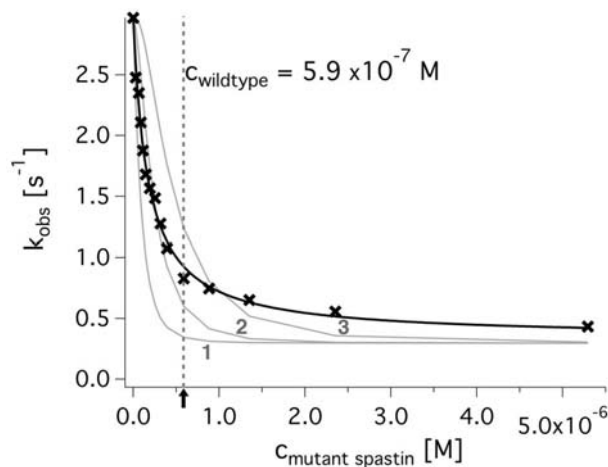
Figure 4.2: Experimental data for the inhibitory effect of increasing mutant concentration on the catalytic turnover rate of wild type spastin, at a fixed concentration of $c_{wt} = 5.9 \cdot 10^{-7}$ M. The data (black crosses) were fitted by the nearest neighbor scheme (black line) as well as the classical binomial fitting (gray lines), where the numbers correspond to the threshold number of mutant subunits incorporated within a hexamer.

differential equations. For the same reasons presented in chapter (3.2) a simulation was performed. To this end the Gillespie algorithm presented in chapter (3.2) was extended to incorporate mutant subunits into the assembly pathway. The mutant enzyme was taken to be catalytically inactive, which means it cannot hydrolyze ATP ($k_{cat,m} = 0$). This was shown experimentally for a number of AAA ATPase protein point-mutants (Hoskins et al., 2009, Eckert et al., 2012a). It was assumed that the inhibitory effect of mutants originates from an allosteric coupling between the subunits incorporated into the hexamer. The catalytic activity of the wild type enzyme present in a heterogeneous hexamer is changed due to interactions with mutants. Accordingly, wild type subunits in the simulation were allowed to have a non-inhibited turnover rate, termed $k_{cat,ww}$, and a reduced, inhibited turnover rate, $k_{cat,wm}$, which originates from the influence of a mutant subunit.

Several different schemes exist that consider the allosteric modulation of the catalytic turnover rate. It has been assumed that a certain threshold number of mutant subunits present in a hexamer reduces the catalytic activity of the hexamer to a basal level, which is generally assumed to be zero (Werbeck et al., 2008). This inhibition scheme resembles the description of the Monod-Wyman-Changeux (MWC) model, which assumes that all subunits of the oligomer are either in a tensed (T) or a relaxed (R) state. They therefore have different affinities to substrates and inhibitors (Monod et al., 1965). However, further possible schemes for the effect of mutant enzymes on the catalytic activity of wild type

enzymes could be:

Scheme 1: one mutant subunit is sufficient to inhibit the activity of all wild type subunits present in the hexamer.

Scheme 2: one mutant subunit inhibits both of its direct neighbors and leaves the others unaffected.

Scheme 3: one mutant subunit inhibits one oriented neighbor and leaves the others unaffected.

Scheme 4: mutant subunits do not have any effect on the wild type subunits in the hexamer.

If mutants do not have any effect on the wild type turnover rate, then the relative increase of mutants compared to a constant concentration of wild type subunits would not change the catalytic turnover rate. If a threshold of more than two subunits has to be overcome, the dependency of turnover rates on mutant concentration, which is the sum over binomial probabilities, should show a sigmoidal behavior. None of these predictions could be observed in experiments (Werbeck et al., 2008), [P3]. Therefore here only the inhibition schemes 1, 2, and 3 will be examined further. A schematic inhibition pattern for each of these schemes is shown in figure (4.3). Furthermore, it is not the activity of the whole hexamer that is regarded but the effect of individual mutant subunits on individual wild type subunits incorporated in a hexamer. In addition, the basal activity can differ from zero.

In the simulation, the incorporation of mutant subunits into hexamers is based on the assembly pathways introduced in chapter (3.2). In the case where only wild type subunits assemble, hexamer formation requires a minimum of five reactions, of which at least three have to be different ones. This simple assembly does not occur when mutant subunits are present, as the number of possible reactions is increased significantly. Each reaction shown in figure (3.3) can occur in any constellation of mutant and wild type intermediates. In addition to this the relative orientation of the reaction partners is taken into account, i.e. the dimers wild type-mutant (WM) and mutant-wild type (MW) form different constellations. This leads to four different dimer species, which in turn lead to 16 possible configurations for trimers and tetramers respectively. This again results in 64 different possible arrangements for mutants and wild types in a hexamer.

(a) Inhibition scheme 1   (b) Inhibition scheme 2   (c) Inhibition scheme 3
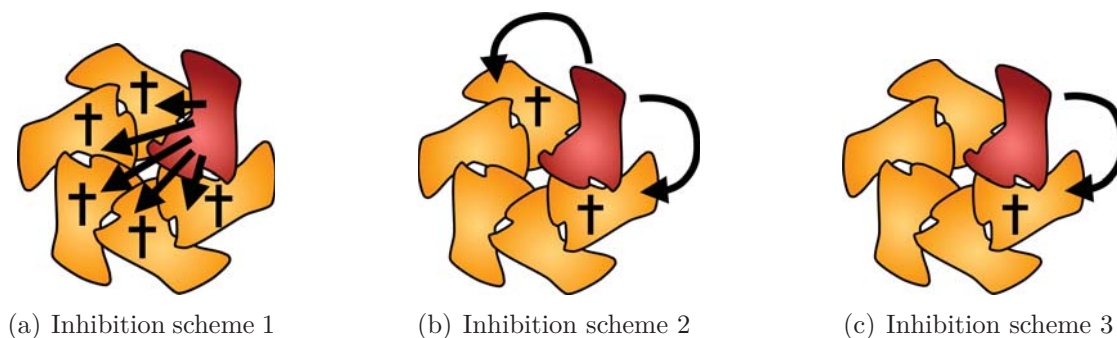
Figure 4.3: Schematic depictions of inhibition by mutant subunits: red monomers denote mutants (no catalytic turnover), and the yellow ones are wild type subunits (fully active). The arrows indicate the effects of a mutant subunit on the remaining wild type subunits, and the crosses correspond to wild type subunits with an inhibited turnover rate.

In principle all reactions could exhibit one unique forward and one unique reverse reaction rate. However, from a molecular perspective it seems reasonable to assume that the kinetic rates depend only on the interaction of the two interacting neighbors. Hence it is reasonable to use the same reaction rate for the oligomerization of WM + WM and MM + WW, because the reaction only occurs between the right mutant of the first dimer and the left wild type of the second, and these interactions are identical. Therefore in the simulation the kinetic rates between two identical reaction interfaces undergoing the same oligomerization process (i.e. dimerization, ..., hexamerization and reverse) were set to the same value. All permutations and possible reactions between intermediate oligomers in the reaction scheme described in chapter (3.2) were taken into account.

Furthermore all 64 possible arrangements of hexamers were divided into 14 rotationally symmetric configurations, as shown in figure (4.4). Each of the arrangements was associated with a specific turnover rate, given by

$$k_{\text{obs, hexamer}} = n_{\text{ww}} \cdot k_{\text{cat,ww}} + n_{\text{wm}} \cdot k_{\text{cat,wm}} \ . \tag{4.11}$$

For each inhibition scheme the number of inhibited and non-inhibited wild type subunits was determined. The fraction of the (non-)inhibited wild type subunits incorporated into the respective hexamer configuration is given in table (4.1).

The simulation was repeated three times for each set of parameters. The output was stable in the sense that all simulation runs resulted in similar values for k_{obs}, both for the 1-2-3-6 and 1-2-4-6 assembly pathway. Increasing the number of mutant subunits at a constant number of wild type subunits (typically $n_{\text{wt}} = 1000$) led to a continuous

WWWWWW
Hexamer 1

WWWWWM
WWWWMW
WWWMWW
WWMWWW
WMWWWW
MWWWWW
Hexamer 2

WWWWMM
WWWMMW
WWMMWW
WMMWWW
MWWWWM
MMWWWW
Hexamer 3

WWWMWM
WWMWMW
WMWWWM
WMWMWW
MWWWMW
MWMWWW
Hexamer 4

WWMWWM
WMWWMW
MWWMWW
Hexamer 5

WWWMMM
WWMMMW
WMMMWW
MWWWMM
MMWWWM
MMMWWW
Hexamer 6

WWMWMM
WMMWWW
WMWMMW
MWWWMW
MWMMWW
MMWWMW
Hexamer 7

WWMMWM
WMWWMM
WMMWMW
MWWMMW
MWMWWM
MMWMWW
Hexamer 8

WMWMWM
MWMWMW
Hexamer 9

WWMMMM
WMMMMW
MWWMMM
MMWWMM
MMMWWM
MMMMWW
Hexamer 10

WMWMMM
WMMMMW
MWMWMM
MWMMMW
MMWMWM
MMMWMW
Hexamer 11

WMMWMM
MWMMWM
MMWMMW
Hexamer 12

WMMMMM
MWMMMM
MMWMMM
MMMWMM
MMMMWM
MMMMMW
Hexamer 13

MMMMMM
Hexamer 14

Figure 4.4: Configuration of rotationally symmetric hexamers: all possible hexameric assemblies (- 64 -) are divided into 14 species which show a rotational symmetry in the case that the ring is closed. Different configurations (bottom) can result in the same symmetric hexamer (top).

configuration	Scheme 1		Scheme 2		Scheme 3	
	fraction of fully active wild type	fraction of inhibited wild type	fraction of fully active wild type	fraction of inhibited wild type	fraction of fully active wild type	fraction of inhibited wild type
(see figure 4.4)	n_{ww}	n_{wm}	n_{ww}	n_{wm}	n_{ww}	n_{wm}
1	6/6	0	6/6	0	6/6	0
2	0	5/5	3/5	2/5	4/5	1/5
3	0	4/4	2/4	2/4	3/4	1/4
4	0	4/4	1/4	3/4	2/4	2/4
5	0	4/4	0	4/4	2/4	2/4
6	0	3/3	1/3	2/3	2/3	1/3
7	0	3/3	0	3/3	1/3	2/3
8	0	3/3	0	3/3	1/3	2/3
9	0	3/3	0	3/3	0	3/3
10	0	2/2	0	2/2	1/2	1/2
11	0	2/2	0	2/2	0	2/2
12	0	2/2	0	2/2	0	2/2
13	0	1/1	0	1/1	0	1/1
14	0	0	0	0	0	0

Table 4.1: Activity pattern in mixed hexamers: for each configuration of the rotationally symmetric hexamers the fraction of fully active wild type subunits and the fraction of inhibited wild type subunits were determined.

1-2-3-6   1-2-4-6

(a) 1000 wild type subunits   (b) 1000 wild type subunits

(c) 5000 wild type subunits   (d) 5000 wild type subunits
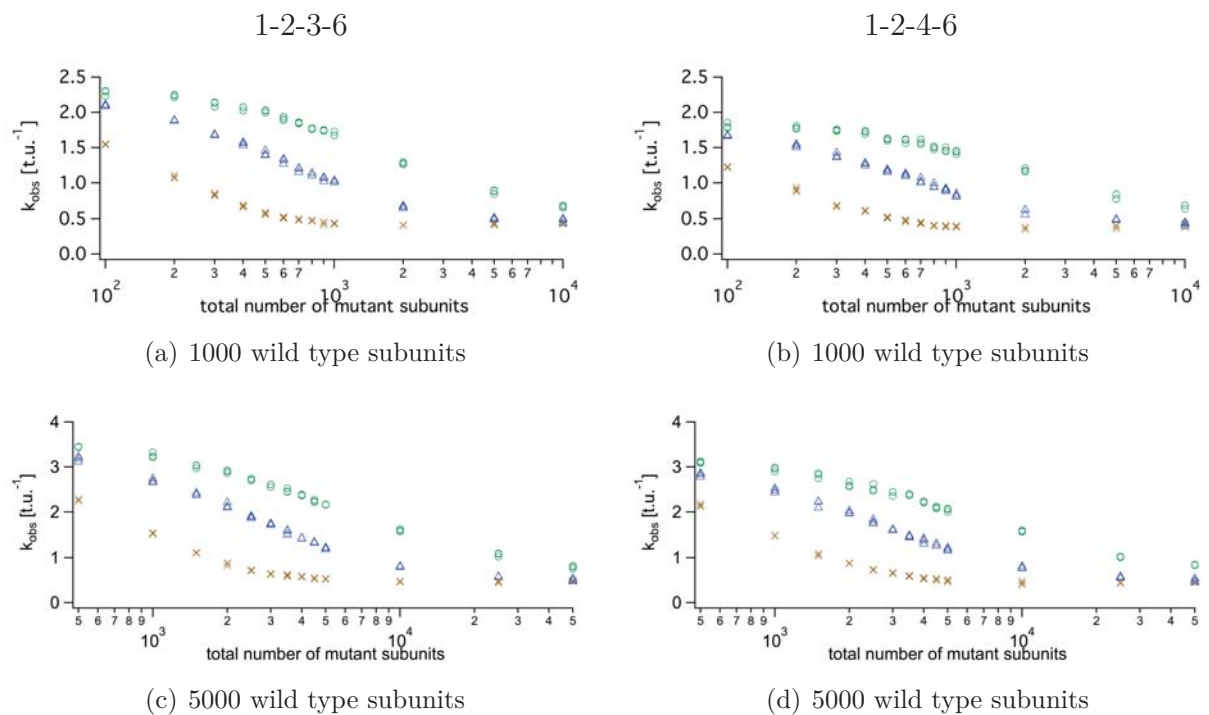
Figure 4.5: Inhibition schemes using the default parameter set: comparison of the inhibitory effect of mutants on the catalytic activity of 1000 and 5000 wild type subunits respectively. The number of mutants was increased proportionally to the wild type. The resultant catalytic activity in inverse time units is depicted as a function of mutant subunits. The ocher crosses are data obtained from simulations using inhibition scheme 1, blue triangles using inhibition scheme 2, and green circles using inhibition scheme 3.

decrease in the turnover rate (k_{obs}) per wild type monomer as shown in figures (4.5(a)) and (b) for the 1-2-3-6 and 1-2-4-6 pathway respectively. In the case that mutant and wild type subunits were allowed to incorporate into oligomers with identical rates given by the default parameter set (see table 3.1), inhibition scheme 1 (one mutant subunit in a hexamer reduces the activity of all wild type subunits present to a slower turnover rate) shows the steepest inhibitory effect and hence has the lowest inhibition coefficient K_{i} (which is the concentration of mutant subunits at which the turnover rate is 50% of the non-inhibited k_{obs}). Inhibition scheme 3 (one mutant subunit in a hexamer reduces the activity of one oriented neighbor to a slower turnover rate) is influenced by the additional mutants only at higher concentrations, hence exhibiting the highest K_{i}. Inhibition scheme 2 (one mutant subunit reduces the activity of both its direct neighbors to a slower turnover rate) shows an intermediate behavior. An estimation shows that the half maximal inhibition is achieved with the addition of 100 to 1000 mutant subunits, depending on the inhibition scheme applied. The inhibition schemes followed a similar pattern even if the number of wild type subunits was increased five-fold (figure 4.5). Simulations were typically performed with 1000 wild type subunits, as this number corresponds approximately to the Michaelis-Menten constant K_{m} obtained in simulations of the assembly of wild type.

As described in chapter (3.2), the effects of varying the kinetic parameters (forward, reverse and catalytic rates) on the turnover rates and hence on the inhibitory effects of mutants were studied. To this end forward and reverse rates were varied for the interactions between wild type and mutant subunits. Decreasing the catalytic turnover rate for a wild type inhibited by mutants, $k_{\mathrm{cat,wm}}$, did not result in a qualitative change in the inhibition pattern. Also varying the forward and reverse assembly rates to achieve different dissociation constants $K_{\mathrm{d}} = k_{i+1,i}/k_{i,i+1}$, which take into account the possible different incorporation affinities of mutant and wild type subunits into oligomers, did not show a qualitative change in the pattern.

Quantitatively, a large ratio of $k_{\mathrm{cat,ww}}$ to $k_{\mathrm{cat,wm}}$, which can be obtained from decreasing the turnover rate of the inhibited subunits $k_{\mathrm{cat,wm}}$ by a factor of ten to $0.05\,\mathrm{s}^{-1}$, leads to the largest discrepancies between the three inhibition schemes (figures 4.6(g) and 4.6(h)). As expected the asymptote of the turnover for all schemes was decreased from $0.5\,\mathrm{s}^{-1}$ to $0.05\,\mathrm{s}^{-1}$. The values for K_{i} were reduced by approximately 10% compared to the default parameter set.

The inhibitory effect was less prominent when assuming that the position of mutant subunits is important for the oligomerization (figures 4.6(c) and (d)). This can be un-

1-2-3-6

1-2-4-6

(a) default

(b) default

(c) $k_{\text{off}}(MX) = 100 \cdot \text{default}$

(d) $k_{\text{off}}(MX) = 100 \cdot \text{default}$

(e) $k_{\text{off}}(\text{mutant}) = 0$

(f) $k_{\text{off}}(\text{mutant}) = 0$

(g) $k_{\text{cat,wm}} = 0.05$ (10% default)

(h) $k_{\text{cat,wm}} = 0.05$ (10% default)
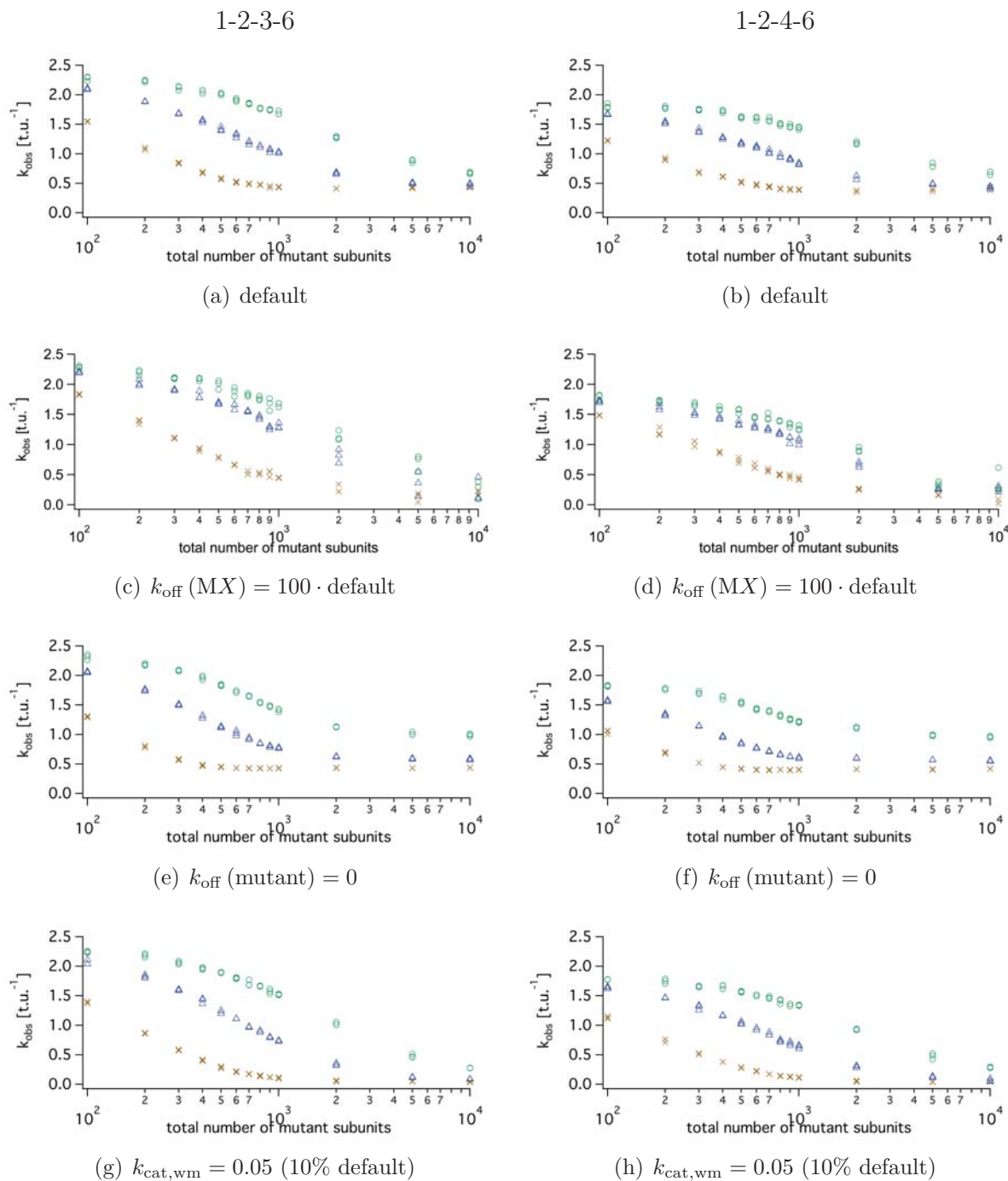
Figure 4.6: Inhibition schemes at various kinetic rates: to study the effect of different kinetic rates on the inhibition induced by mutants, the parameters were changed according to the captions shown. The turnover rate in time units^{-1} is shown as a function of mutant concentration. The ocher crosses are data obtained from simulations using inhibition scheme 1, blue triangles using inhibition scheme 2, and green circles using inhibition scheme 3.

derstood with the idea that the subunits have two distinguished binding sites, where one is the active binding site (without loss of generality assumed to be the right side in this scheme) and the other is the passive binding site. The first site is required for binding a further subunit, the latter site be bound by another subunit. Mutants can bind any subunit but their lifetime within an oligomer is short due to their interaction surface, i.e. $k_{\text{off}}(MX) = 100 \cdot 10 \, \text{s}^{-1}$. Wild type subunits can bind both species and their lifetime is unaffected by an interaction with mutants, i.e. $k_{\text{off}}(WW) = k_{\text{off}}(WM) = 10 \, \text{s}^{-1}$ (default). These rates lead to a large pool of mutant monomers and hence reduce the amount of hexamers with incorporated mutants. Therefore the inhibition is weakened, especially at low mutant concentrations. This also leads to the observation that inhibition scheme 2 is weakly inhibited compared to the default parameter set.

One extreme condition regarding mutant-wild type interaction is, that firstly one mutant subunit does bind to its partner without the possibility to disassemble, and secondly mutant subunits can only be released after hydrolyzation of a hexamer including ADP release (figures 4.6(e) and (f)). These assumptions are realized if the reverse rate of oligomers including mutants is zero ($k_{\text{off}}(MX) = k_{\text{off}}(XM) = 0$) whereas the turnover rate $k_{\text{cat,wm}}$ is greater than zero (in the simulation depicted in figures (4.6(e)) and (f) it was set to the default value of $k_{\text{cat,wm}} = 0.5 \, \text{s}^{-1}$). All three inhibition schemes show a lower K_i compared to simulations using the default parameter set, which was expected as mutants incorporate into oligomers more easily than is reflected by the default parameters. However, inhibition scheme 3 shows a significantly higher asymptote for the turnover rate compared to the default parameter set ($k_{\text{obs},\infty} = 1 \, \text{s}^{-1}$ vs. $k_{\text{obs},\infty,\text{default}} = 0.5 \, \text{s}^{-1}$). This can be explained by the following: with the dissociation rate of mutants set to zero the pool of their free monomers is reduced very rapidly. Furthermore at high mutant concentrations the oligomerization into homo-mutant-hexamers is favored and as these hexamers cannot react any further this also leads to a significant decrease in free mutants. The relatively small number of wild type subunits on the other hand can react equally well compared to the simulations with default rates. Hence at some point the mutants are incorporated into slowly hydrolyzing hexamers, whereas hexamers with few mutants can react faster and refill the pool of wild type monomers. In addition the inhibition scheme 3 assumes the weakest inhibitory effect by mutants. These considerations explain the higher asymptote observed.

All these observations describe the inhibition pattern resulting from both assembly pathways, 1-2-3-6 and 1-2-4-6, equally well, suggesting that the assembly pathway does not play a crucial role in the inhibition mechanism.

4.3   Analysis of inhibitory effects

One key question to be answered through the simulation and inhibition study was whether it is possible to generate simple formulas with which inhibition experiments can be fit and the inhibitory effect and pattern of mutant subunits on active wild types deduced. For other AAA ATPases a binomial fit model, which was introduced in chapter (2.3.3) as the classical fit function, has frequently been used in the literature (Werbeck et al., 2008, Hoskins et al., 2009, Stotz et al., 2011). However, in this approach the turnover rate is computed per hexamer, which means that the hexamer is 100% active when the number of incorporated mutants is lower then the threshold required, and is completely inactive otherwise. The resultant population distribution and relative activity per percentage of mutants present are shown by Werbeck et al. (2008).

This model however has several disadvantages: the sum of wild type and mutant is constant, i.e. the concentration of wild type is reduced to zero as mutants increase to 100%. As fewer fully active hexamers are present, the amount of hydrolyzed ATP is reduced, leading to a low signal to noise ratio, both in simulations and experiments. Futhermore this classical approach does not implement allosteric effects, which is the assumption that the wild type enzyme has two states, namely a fully active and a less active one. Finally, this model uses the initial concentration of enzyme to compute the binomal probabilities (see equation 2.36 in chapter 2.3.3). This is a crude approximation as the initial and the steady state equilibria are likely to differ.

4.3.1   Extended binomial fitting function

Therefore a novel fitting function based on a binomial distribution was developed, which includes the following aspects: the activity is calculated per wild type monomer with the possibility to distinguish between the fully active ($k_{\text{cat,ww}}$) and the inhibited, basally active enzyme ($k_{\text{cat,wm}}$). Furthermore, mutant and wild type can assemble with different rates into oligomers. Finally only homo-hexamers consisting of wild type are fully active, whereas one mutant is sufficient to inhibit all wild type subunits present to the basal level, and the mutants themselves are inactive.

The sum over the number of hexamers with one, two, ..., mutants is taken. The probability of finding a hexamer with n mutants ($n \in \{0; 5\}$)[2] is computed, assuming a

---

[2]Mutant homo-hexamers are regarded as catalytically incapable, i.e. they cannot hydrolyze ATP, and hence do not occur in this fit function.

binomial distribution of mutants in hexamers. The probability to encounter a hexamer with at least one mutant is

$$p\left(\text{mut} \geq 1\right) = \frac{\sum\limits_{k=1}^{5} \binom{6}{k} \left(\frac{n_{\text{wt}}}{n_{\text{wt}}+n_{\text{mut}}}\right)^{(6-k)} \left(1 - \frac{n_{\text{wt}}}{n_{\text{wt}}+n_{\text{mut}}}\right)^{k}}{\sum\limits_{k=0}^{5} \binom{6}{k} \left(\frac{n_{\text{wt}}}{n_{\text{wt}}+n_{\text{mut}}}\right)^{(6-k)} \left(1 - \frac{n_{\text{wt}}}{n_{\text{wt}}+n_{\text{mut}}}\right)^{k}} \, , \tag{4.12}$$

with n_{wt} and n_{mut} the number of wild type and mutant subunits respectively. The summands in the numerator represent the number of hexamers with one to five mutant subunits respectively, whereas the denominator reflects all hexamers with at least one wild type subunit. The probability of encountering a homo-wild type hexamer is hence

$$p\left(\text{mut} = 0\right) = \frac{\left(\frac{n_{\text{wt}}}{n_{\text{wt}}+n_{\text{mut}}}\right)^{6}}{\sum\limits_{k=0}^{5} \binom{6}{k} \left(\frac{n_{\text{wt}}}{n_{\text{wt}}+n_{\text{mut}}}\right)^{(6-k)} \left(1 - \frac{n_{\text{wt}}}{n_{\text{wt}}+n_{\text{mut}}}\right)^{k}} \, . \tag{4.13}$$

The observed turnover rate is then computed via

$$\begin{aligned}
k_{\text{obs}} &= k_{\text{cat, ww}} \frac{\sum\limits_{k=1}^{5} \binom{6}{k} \left(\frac{n_{\text{wt}}}{n_{\text{wt}}+n_{\text{mut}}}\right)^{(6-k)} \left(1 - \frac{n_{\text{wt}}}{n_{\text{wt}}+n_{\text{mut}}}\right)^{k}}{\sum\limits_{k=0}^{5} \binom{6}{k} \left(\frac{n_{\text{wt}}}{n_{\text{wt}}+n_{\text{mut}}}\right)^{(6-k)} \left(1 - \frac{n_{\text{wt}}}{n_{\text{wt}}+n_{\text{mut}}}\right)^{k}} \\
&\quad + k_{\text{cat, wm}} \frac{\left(\frac{n_{\text{wt}}}{n_{\text{wt}}+n_{\text{mut}}}\right)^{6}}{\sum\limits_{k=0}^{5} \binom{6}{k} \left(\frac{n_{\text{wt}}}{n_{\text{wt}}+n_{\text{mut}}}\right)^{(6-k)} \left(1 - \frac{n_{\text{wt}}}{n_{\text{wt}}+n_{\text{mut}}}\right)^{k}} \\
&= \frac{n_{\text{wt}}^{5} k_{\text{cat, ww}} + \left(6n_{\text{mut}}^{4} + 15n_{\text{mut}}^{3}n_{\text{wt}} + 20n_{\text{mut}}^{2}n_{\text{wt}}^{2} + 15n_{\text{mut}}n_{\text{wt}}^{3} + 6n_{\text{wt}}^{4}\right) n_{\text{mut}} k_{\text{cat, wm}}}{6n_{\text{mut}}^{5} + 15n_{\text{mut}}^{4}n_{\text{wt}} + 20n_{\text{mut}}^{3}n_{\text{wt}}^{2} + 15n_{\text{mut}}^{2}n_{\text{wt}}^{3} + 6n_{\text{mut}}n_{\text{wt}}^{4} + n_{\text{wt}}^{5}} \, .
\end{aligned} \tag{4.14}$$

Thus far the assumption is that wild type and mutant subunits assemble into hexamers with the same association rates. In order to take into account the possibility of different affinities between the two species, a factor d was introduced, with which n_{mut} in equation (4.14) was multiplied:

$$k_{\text{obs}} = \frac{n_{\text{wt}}^{5} k_{\text{cat, ww}}}{6d^{5}n_{\text{mut}}^{5} + 15d^{4}n_{\text{mut}}^{4}n_{\text{wt}} + 20d^{3}n_{\text{mut}}^{3}n_{\text{wt}}^{2} + 15d^{2}n_{\text{mut}}^{2}n_{\text{wt}}^{3} + 6dn_{\text{mut}}n_{\text{wt}}^{4} + n_{\text{wt}}^{5}}$$

$$\tag{4.15}$$

$$+ \frac{\left(6d^{4}n_{\text{mut}}^{4} + 15d^{3}n_{\text{mut}}^{3}n_{\text{wt}} + 20d^{2}n_{\text{mut}}^{2}n_{\text{wt}}^{2} + 15dn_{\text{mut}}n_{\text{wt}}^{3} + 6n_{\text{wt}}^{4}\right) dn_{\text{mut}} k_{\text{cat, wm}}}{6d^{5}n_{\text{mut}}^{5} + 15d^{4}n_{\text{mut}}^{4}n_{\text{wt}} + 20d^{3}n_{\text{mut}}^{3}n_{\text{wt}}^{2} + 15d^{2}n_{\text{mut}}^{2}n_{\text{wt}}^{3} + 6dn_{\text{mut}}n_{\text{wt}}^{4} + n_{\text{wt}}^{5}}$$

Figure 4.7: Non-competitive inhibition scheme: E denotes the enzyme , I the inhibitor, S the substrate, ES the enzyme-substrate complex, IE the inhibitor-enzyme complex, IES the inhibitor-enzyme-substrate complex and P the released product. In this scheme state one is presented by E, state two by ES, state three by IE and state four by IES. The rates k_{ij} are the on- and k_{ji} the off-rates of the states respectively.

4.3.2   Extended non-competitive fitting function

In addition to the extended binomial fitting function, an extended non-competitive inhibition model was developed. In this model the binding affinities of substrates and inhibitors are completely independent of each other. Both can bind to the enzyme alone as well as to an enzyme-substrate complex (figure 4.7). In this study the ternary complex (IES of figure 4.7) is assumed to have a smaller turnover rate compared to the non-inhibited form. Here cS and cE both represent the concentration of wild type. This distinct consideration of the concentration of wild type circumvents the need to consider non-linear equations (see equations 3.1 and 3.2). cI denotes the concentration of mutant enzyme. The concentrations of cES and $cIES$ were calculated from the concentrations of the enzymes and the kinetic rates using the law of mass action. The total turnover rate is given by the superposition of the fully active and inhibited complexes multiplied with their catalytic turnover rates respectively. The fit function for the non-competitive inhibition model is given by the following equation:

$$f(x) = \frac{n_{\mathrm{wt}} \left(k_{\mathrm{cat,\,ww}} \cdot K_{\mathrm{i}} + k_{\mathrm{cat,\,wm}} \cdot x\right)}{\left(K_{\mathrm{m}} + n_{\mathrm{wt}}\right)\left(K_{\mathrm{i}} + x\right)} \ , \tag{4.16}$$

where n_{wt} denotes the number of total wild type subunits inserted, K_{i} the concentration of mutant subunits at which the turnover rate is 50% of the non-inhibited k_{obs}, $k_{\mathrm{cat,\,ww}}$ and $k_{\mathrm{cat,\,wm}}$ the non-inhibited and inhibited turnover rates respectively. x denotes the number of mutants. Equation (4.16) is an extension of a textbook formula of Fersht (1985) and is generalized with respect to the inhibited turnover rate, which can differ from zero.

4.3.3   Applying fitting functions to simulated data

In order to examine the applicability of these simplified fit models, the data obtained from
the inhibition simulation using the default parameter set were fit (figures 4.8 and 4.9). A
single exponential fit was used as a purely empirical comparison.

The non-competitive inhibition model fits the data of inhibition schemes 2 and 3 very
well, but displays a systematic deviation while fitting data of the inhibition scheme 1 (one
mutant inhibits all wild type subunits). This can be seen in the distribution of the residuals
in figures (4.8(b)) and (4.9(b)). This is not surprising as the fundamental assumption of
the inhibition scheme (binomial distribution of mutant subunits into the hexamer with
one mutant sufficient to inhibit all remaining wild type subunits) and the fit model (non-
competitive inhibition of wild type by mutants) differ significantly. Inversely, the binomial
fitting function could be applied to all three inhibition schemes equally well (figures 4.8(a)
and 4.9(a)). Important to note, however, an exponential fit which contains no information
about inhibitory effects, also fits all three inhibition schemes equally well. This means that
from the fits alone no conclusion on the kinetic mechanism can be drawn. The quantitative
mismatch of the fit turnover rate of non-inhibited wild type ($k_{cat,ww}$) by the binomial fit
function is significant, as it is a factor of two to three lower than the inserted value in
the simulation (tables 4.2, 4.3, and 4.4). Furthermore this turnover rate is known from
experiments, leading to a severe deficit of the binomial fit function.
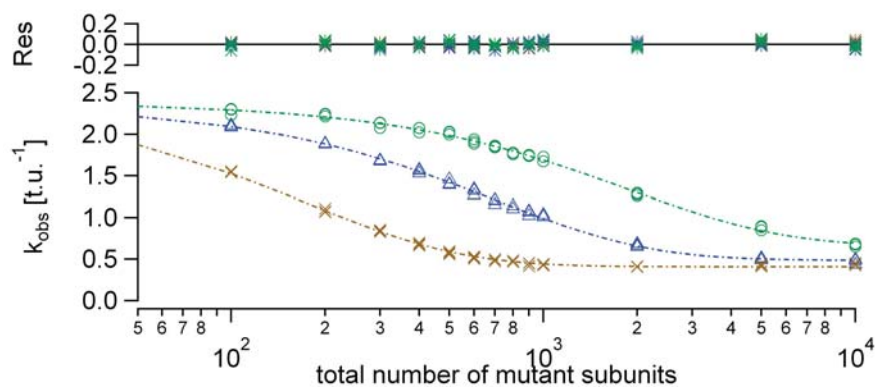
(a) binomial fit
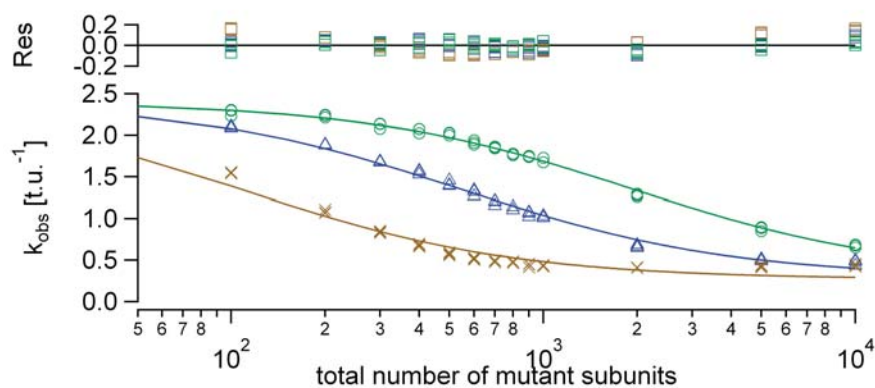
(b) non-competitive fit
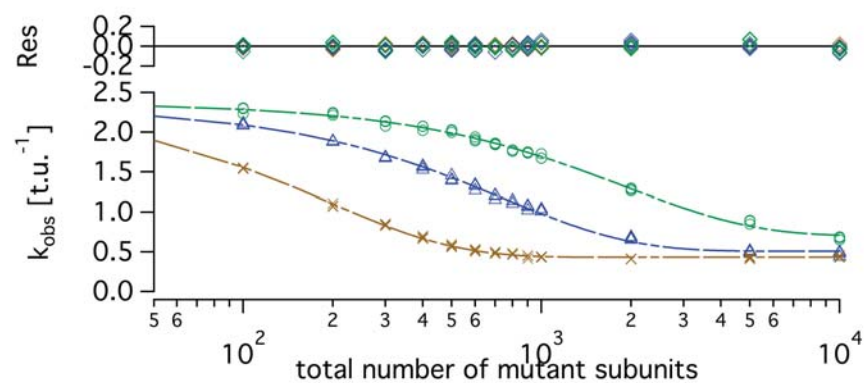
(c) exponential fit

Figure 4.8: Fit models: the inhibitory effects of mutants according to inhibition schemes 1, 2, and 3 obtained from simulations using the 1-2-3-6 assembly pathway as fit by the extended binomial fit model (a), the extended non-competitive inhibition model (b), and an exponential fit (c). The ocher crosses are data obtained from simulations using inhibition scheme 1, blue triangles using inhibition scheme 2, and green circles using inhibition scheme 3. It can be seen that the models fit the data accurately, except for the non-competitive fit, which fails to fit the data obtained from inhibition scheme 1.
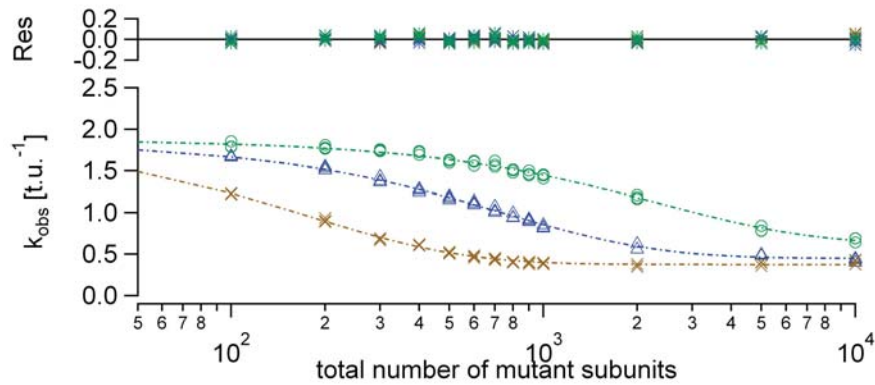
(a) binomial fit
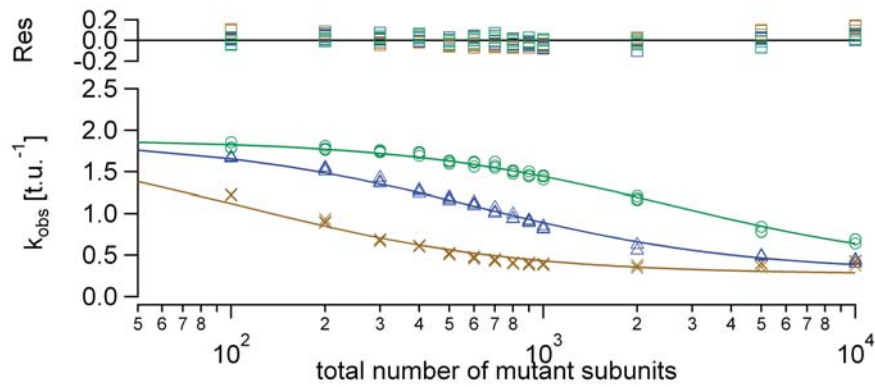
(b) non-competitive fit
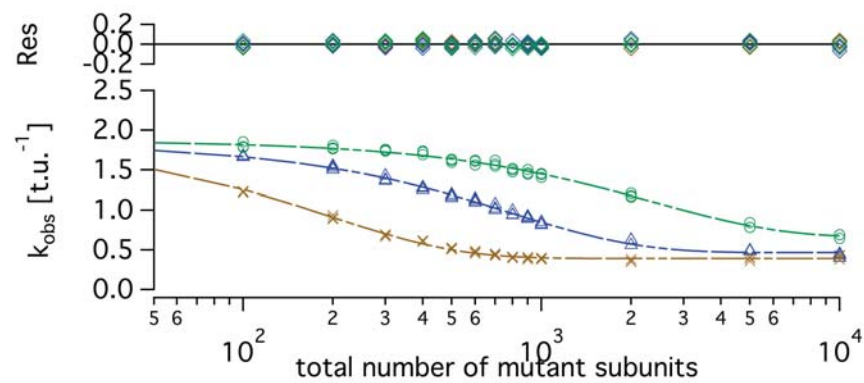
(c) exponential fit

Figure 4.9: Fit models: the inhibitory effects of mutants according to inhibition schemes 1, 2, and 3 obtained from simulations using the 1-2-4-6 assembly pathway as fit by the extended binomial fit model (a), the extended non-competitive inhibition model (b), and an exponential fit (c). The ocher crosses are data obtained from simulations using inhibition scheme 1, blue triangles using inhibition scheme 2, and green circles using inhibition scheme 3. It can be seen that the models fit the data accurately, except for the non-competitive fit, which fails to fit the data obtained from inhibition scheme 1.

Variations of simulation	Assembly pathway	Inhibition scheme	Exponential fit					
			y_0	σy_0	A	σA	τ^{-1}	$\sigma\tau^{-1}$
default	1-2-3-6	s1	0.43155	0.00400	1.90682	0.00996	0.00524	5.91e-05
		s2	0.50736	0.01199	1.81483	0.01643	0.00135	2.62e-05
		s3	0.70100	0.01586	1.67131	0.01678	0.00052	1.42e-05
	1-2-4-6	s1	0.39157	0.00553	1.44483	0.01360	0.00514	1.05e-04
		s2	0.46547	0.01071	1.36354	0.01447	0.00127	2.91e-05
		s3	0.65743	0.01763	1.21091	0.01746	0.00042	1.74e-05
$k_{\mathrm{off}}(Mut)=0$	1-2-3-6	s1	n.A.	n.A.	n.A.	n.A.	n.A.	n.A.
		s2	0.58474	0.00760	1.83004	0.01229	0.00235	3.39e-05
		s3	0.98482	0.01629	1.46961	0.02144	0.00114	3.63e-05
	1-2-4-6	s1	n.A.	n.A.	n.A.	n.A.	n.A.	n.A.
		s2	0.55026	0.00831	1.33009	0.01472	0.00290	6.97e-06
		s3	0.96931	0.01922	0.94687	0.02523	0.00113	6.58e-05
$k_{\mathrm{cat,wm}}=0.05$	1-2-3-6	s1	0.08407	0.00745	2.2479	0.01829	0.00512	8.99e-05
		s2	0.12263	0.01151	2.21623	0.01573	0.00133	2.03e-05
		s3	0.28886	0.01400	2.06897	0.01477	0.00052	1.00e-05
	1-2-4-6	s1	0.07687	0.00684	1.70558	0.01553	0.00448	8.84e-05
		s2	0.10483	0.01088	1.72988	0.01452	0.00121	2.21e-05
		s3	0.25580	0.01792	1.59470	0.01750	0.00040	1.27e-05
5000 Wt	1-2-3-6	s1	0.50714	0.00703	3.14095	0.01810	0.00112	1.39e-05
		s2	0.59223	0.0209	3.01797	0.03018	0.00033	6.94e-06
		s3	0.90786	0.02762	2.71158	0.03289	0.00015	4.46e-06
	1-2-4-6	s1	0.47619	0.00825	2.81538	0.02013	0.00101	1.56e-05
		s2	0.57085	0.02085	2.64111	0.02948	0.00031	7.26e-06
		s3	0.89909	0.02761	2.34726	0.03206	0.00014	4.72e-06
$k_{\mathrm{off}}(MX)=1000$	1-2-3-6	s1	0.23668	0.01997	2.09803	0.03441	0.00274	9.72e-05
		s2	0.26170	0.03736	2.06461	0.04342	0.00070	3.64e-05
		s3	0.30019	0.04814	2.05199	0.04724	0.00041	2.71e-05
	1-2-4-6	s1	0.18677	0.01657	1.59119	0.02555	0.00206	7.05e-05
		s2	0.23858	0.01639	1.57651	0.01874	0.00067	1.98e-05
		s3	0.30622	0.03492	1.56833	0.03604	0.00048	3.08e-05

Table 4.2: Fit parameters of the exponential fit, according to $y = y_0 + A\exp\left(-\tau^{-1}x\right)$, with y_0 the offset, A the amplitude, τ the life time and σ their respective standard deviation.

Variations of simulation	Assembly pathway	Inhibition scheme	Binomial fit						
			$k_{\text{cat,ww}}$	$\sigma k_{\text{cat,ww}}$	$k_{\text{cat,wm}}$	$\sigma k_{\text{cat,wm}}$	n_{wt}	d	σd
default	1-2-3-6	s1	2.35588	0.01023	0.40836	0.00444	1000	0.96523	0.01234
		s2	2.34313	0.01041	0.48596	0.00942	1000	0.24267	0.00387
		s3	2.38208	0.00956	0.65458	0.01558	1000	0.08933	0.00236
	1-2-4-6	s1	1.85108	0.01234	0.37417	0.00540	1000	0.94985	0.01931
		s2	1.84275	0.01096	0.44806	0.01024	1000	0.22703	0.00517
		s3	1.87394	0.01014	0.61548	0.02029	1000	0.07150	0.00328
$k_{\text{off}}(Mut) = 0$	1-2-3-6	s1	2.38643	0.01684	0.4067	0.00603	1000	1.53640	0.03347
		s2	2.43623	0.01642	0.56069	0.01119	1000	0.42765	0.00953
		s3	2.46437	0.01984	0.96370	0.01968	1000	0.20075	0.00803
	1-2-4-6	s1	1.85112	0.01250	0.38859	0.00449	1000	1.52442	0.03330
		s2	1.89395	0.02005	0.53195	0.01216	1000	0.52818	0.01939
		s3	1.92135	0.02104	0.95431	0.02104	1000	0.19756	0.01310
$k_{\text{cat,wm}} = 0.05$	1-2-3-6	s1	2.35378	0.00918	0.05523	0.00403	1000	0.94012	0.00913
		s2	2.36294	0.00948	0.09556	0.00865	1000	0.23881	0.00285
		s3	2.36993	0.00847	0.23145	0.01394	1000	0.08841	0.00168
	1-2-4-6	s1	1.80142	0.00782	0.05347	0.00369	1000	0.82174	0.00895
		s2	1.85200	0.01007	0.08258	0.00964	1000	0.21604	0.00362
		s3	1.85700	0.01017	0.19664	0.02152	1000	0.06778	0.00247
5000 Wt	1-2-3-6	s1	3.67386	0.01054	0.46911	0.00443	5000	1.02671	0.00823
		s2	3.64891	0.01852	0.55688	0.01523	5000	0.29610	0.00479
		s3	3.64097	0.01872	0.85714	0.02307	5000	0.13353	0.00329
	1-2-4-6	s1	3.31778	0.01434	0.43999	0.00634	5000	0.92995	0.01127
		s2	3.24531	0.01891	0.54014	0.01608	5000	0.27646	0.00530
		s3	3.26493	0.01995	0.85293	0.02597	5000	0.12204	0.00390
$k_{\text{off}}(MX) = 1000$	1-2-3-6	s1	2.36605	0.02585	0.20783	0.01615	1000	0.50094	0.01503
		s2	2.34203	0.02997	0.22131	0.03895	1000	0.12235	0.00667
		s3	2.36414	0.02506	0.23006	0.05138	1000	0.06981	0.00476
	1-2-4-6	s1	1.79997	0.02033	0.16687	0.01485	1000	0.37524	0.01210
		s2	1.82621	0.01400	0.20671	0.01889	1000	0.11545	0.00399
		s3	1.88149	0.02357	0.25923	0.04131	1000	0.08212	0.00607

Table 4.3: Fit parameters and constants of the binomial fit with a variable $k_{\text{cat,ww}}$: $k_{\text{cat,ww}}$, $k_{\text{cat,wm}}$, and d are fit parameters and σ their respective standard deviation. The value of n_{wt} was kept fixed at 1000 and 5000 particles respectively.

Non-competitive fit

Variations of simulation	Assembly pathway	Inhibition scheme	$k_{\mathrm{cat,ww}}$	$\sigma k_{\mathrm{cat,ww}}$	$k_{\mathrm{cat,wm}}$	$\sigma k_{\mathrm{cat,wm}}$	K_{M}	σK_{M}	K_{I}	σK_{I}	n_{wt}
default	1-2-3-6	s1	4.8354	40293.9000	0.5449	4541.1100	1024.7100	1.69e+07	111.76900	9.97217	1000
		s2	4.9369	9202.9900	0.6019	1121.9400	1054.1800	3.83e+06	547.31600	23.26190	1000
		s3	4.9183	5473.0000	0.6390	711.0500	1044.5200	2.28e+06	1909.10000	83.82840	1000
	1-2-4-6	s1	4.2050	22180.3000	0.6031	3181.0700	1237.7600	1.18e+07	112.69700	9.67716	1000
		s2	4.2713	7266.5500	0.6692	1138.5200	1269.6100	3.86e+06	602.30300	32.30870	1000
		s3	4.4052	5203.2200	0.7579	895.2170	1335.8800	2.76e+06	2531.77000	184.14300	1000
$k_{\mathrm{off}}(Mut) = 0$	1-2-3-6	s1	4.8075	29506.4000	0.6052	3714.4400	1008.1900	1.23e+07	63.03680	6.40764	1000
		s2	4.9983	22743.0000	0.7855	3574.0700	1011.6500	9.15e+06	288.07300	24.56620	1000
		s3	4.9597	6379.4000	1.5562	2001.6100	992.8740	2.56e+06	726.37400	67.54560	1000
	1-2-4-6	s1	4.3995	36953.6000	0.7371	6191.5700	1367.6000	1.99e+07	63.10810	6.87133	1000
		s2	4.3132	25101.1000	0.9302	5413.4200	1245.9000	1.31e+07	227.58100	25.01070	1000
		s3	4.1770	4981.7600	1.7926	2137.9400	1162.8800	2.58e+06	763.65000	93.50450	1000
$k_{\mathrm{cat,wm}} = 0.05$	1-2-3-6	s1	4.8208	130159.0000	-4.93e-17	0.0617	1000.9200	5.40e+07	93.87690	9.40971	1000
		s2	4.3825	34106.9000	1.21e-17	0.0655	783.5450	1.39e+07	480.23400	30.02750	1000
		s3	5.8089	10323.9000	1.02e-16	0.1007	1390.8700	4.25e+06	1603.75000	88.59650	1000
	1-2-4-6	s1	4.2264	74301.0000	-1.36e-17	0.0543	1281.4500	4.01e+07	112.11000	9.35815	1000
		s2	4.6009	27910.2000	2.78e-17	0.0732	1393.5600	1.45e+07	545.26500	40.52040	1000
		s3	4.3136	11616.6000	-3.36e-17	0.1157	1272.8900	6.12e+06	2141.11000	180.00100	1000
5000 Wt	1-2-3-6	s1	3.8349	16290.5000	0.2490	1057.7300	147.9470	2.19e+07	524.02600	39.91430	5000
		s2	4.9716	6017.1300	0.3405	412.0770	1613.3700	8.00e+06	2152.98000	109.51300	5000
		s3	4.8159	2048.0500	0.5747	244.4170	1502.5000	2.77e+06	5739.47000	145.09400	5000
	1-2-4-6	s1	4.8682	15121.6000	0.3279	1018.4400	2223.0800	2.24e+07	587.88300	51.99730	5000
		s2	4.4310	4120.8500	0.3625	337.1440	1629.3500	6.17e+06	2329.11000	93.47540	5000
		s3	4.0966	1891.6000	0.5863	270.7220	1177.7400	2.85e+06	6393.36000	289.45000	5000
$k_{\mathrm{off}}(MX) = 1000$	1-2-3-6	s1	4.9106	26818.2000	0.0369	201.3350	1008.4000	1.10e+07	234.60100	13.32500	1000
		s2	5.7252	18806.4000	0.0000	0.1396	1380.6200	7.82e+06	1141.71000	93.97470	1000
		s3	5.3609	16716.1000	0.0000	0.1679	1207.3500	6.88e+06	1998.0200	190.8020	1000
	1-2-4-6	s1	3.1974	27737.9000	0.0250	216767.0000	720.9670	1.49e+07	328.95700	19.27900	1000
		s2	4.4034	13088.3000	0.0000	0.0912	1362.4300	7.02e+06	1283.60000	88.42350	1000
		s3	4.9116	20952.2000	0.0000	0.1901	1572.9800	1.10e+06	1941.86000	234.36400	1000

Table 4.4: Fit parameters and constants of the non-competitive fit with a variable $k_{\mathrm{cat,ww}}$: $k_{\mathrm{cat,ww}}$, $k_{\mathrm{cat,wm}}$, K_{M}, and K_{I} are fit parameters and σ their respective standard deviation. The value of n_{wt} was kept fixed at 1000 and 5000 particles respectively.
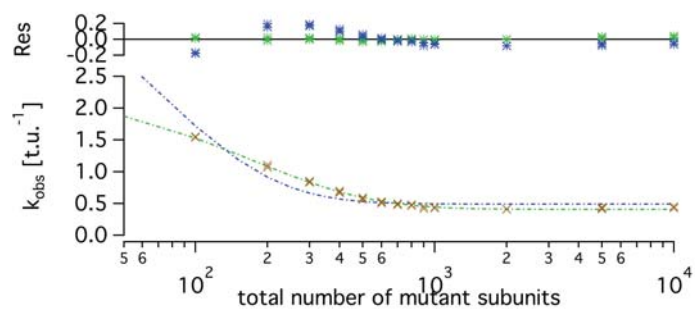
Hence the number of free fit parameters was reduced by setting the turnover rate to a fixed value $k_{cat,ww} = 5.0\,s^{-1}$ in both fit models. Using this constraint the binomial fit function displayed an obvious qualitative deviation as shown in figures (4.10(a)) and (b). The non-competitive inhibition model, however, was qualitatively unaffected by this restraint. The quantitative agreement of this fit model with reduced fit parameters was improved as the fit value of the Michaelis-Menten coefficient K_m was now close to the value obtained in experiments with wild type only (see figure 3.5). Furthermore the fit returns a reasonable value $k_{cat,wm}$, which is close to the value assigned in the simulation. In addition the value for K_i is close to the value of half-maximal inhibition (tables 4.5 and 4.6).

Considering the expected deviation of the fitting of inhibition scheme 1, the extended non-competitive inhibition model characterizes both inhibition schemes 2 and 3 qualitatively and also quantitatively with good accuracy.

(a) comparison of binomial fits 1-2-3-6
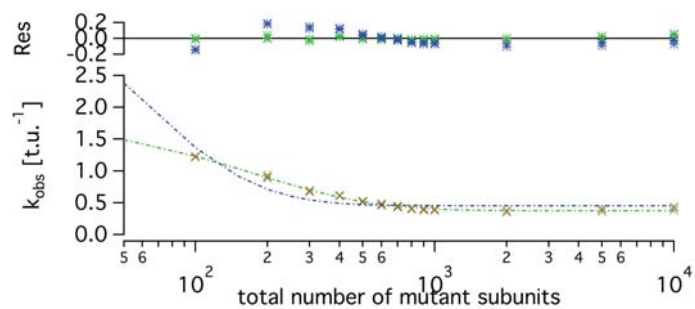
(b) comparison of binomial fits 1-2-4-6
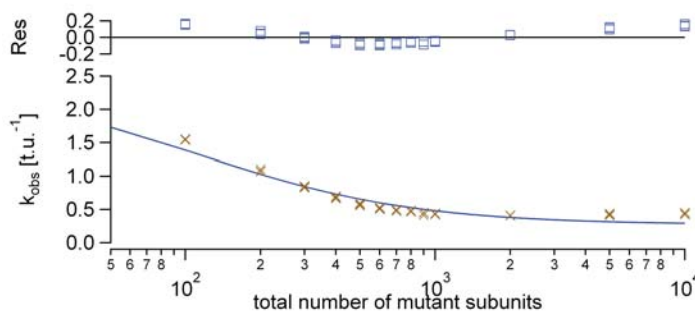
(c) comparison of non-competitive fits 1-2-3-6
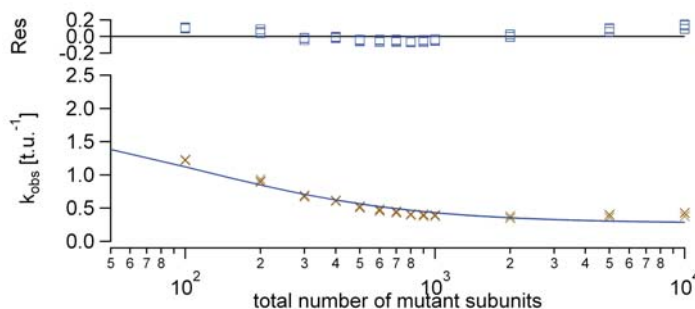
(d) comparison of non-competitive fits 1-2-4-6

Figure 4.10: Binomial and non-competitive fit: the number of free fit parameters was reduced by setting the catalytic turnover rate $k_{cat,ww}$ to a fixed value of $5\,s^{-1}$. It can be seen that the extended binomial fit function (blue line) fails to fit the data quantitatively, whereas the non-competitive fit model (green line) still results in an accurate quantitative fit. This is true for both assembly pathways.

Variations of simulation	Assembly pathway	Inhibition scheme	Binomial fit					
			$k_{cat,ww}$	$k_{cat,wm}$	$\sigma k_{cat,wm}$	n_{wt}	d	σd
default	1-2-3-6	s1	5	0.4914	0.1358	1000	2.4201	0.6624
		s2	5	0.9761	0.1608	1000	1.5519	0.4132
		s3	5	1.5662	0.1612	1000	1.8650	0.6589
	1-2-4-6	s1	5	0.4530	0.1558	1000	3.0677	1.1681
		s2	5	0.8940	0.1683	1000	2.4198	0.9012
		s3	5	1.3878	0.1639	1000	3.3552	1.8439
$k_{off}(Mut) = 0$	1-2-3-6	s1	5	0.4368	0.1294	1000	3.0655	0.9650
		s2	5	0.8184	0.1501	1000	1.6256	0.4007
		s3	5	1.4378	0.1557	1000	1.6648	0.5076
	1-2-4-6	s1	5	0.4172	0.1525	1000	3.7497	1.6988
		s2	5	0.7040	0.1622	1000	2.4847	0.8701
		s3	5	1.3136	0.1610	1000	3.0489	1.4706
$k_{cat,wm} = 0.05$	1-2-3-6	s1	5	0.1540	0.1377	1000	2.2288	0.5405
		s2	5	0.6341	0.1778	1000	1.2067	0.2791
		s3	5	1.2890	0.1863	1000	1.3292	0.4028
	1-2-4-6	s1	5	0.1684	0.1612	1000	2.6875	0.8864
		s2	5	0.6345	0.1797	1000	1.8990	0.5956
		s3	5	1.2186	0.1758	1000	2.7182	1.2612
5000 Wt	1-2-3-6	s1	5	0.5271	0.0760	5000	1.5186	0.1696
		s2	5	0.8181	0.1290	5000	0.5760	0.0642
		s3	5	1.2576	0.1744	5000	0.3529	0.0463
	1-2-4-6	s1	5	0.5198	0.0954	5000	1.5904	0.2293
		s2	5	0.9173	0.1476	5000	0.7463	0.1137
		s3	5	1.4516	0.1894	5000	0.5198	0.0946
$k_{off}(MX) = 1000$	1-2-3-6	s1	5	0.4562	0.1485	1000	1.6987	0.3923
		s2	5	1.1035	0.1828	1000	1.3174	0.3711
		s3	5	1.4271	0.1815	1000	1.4921	0.4924
	1-2-4-6	s1	5	0.4796	0.1704	1000	2.2024	0.7026
		s2	5	0.9950	0.1770	1000	2.3623	0.9312
		s3	5	1.1890	0.1750	1000	2.6093	1.1564

Table 4.5: Fit parameters of binomial fit with a fix $k_{cat,ww}$: $k_{cat,wm}$ and d are fit parameters and σ their respective standard deviation. The value of $k_{cat,ww}$ was kept fixed at $5.0\,\mathrm{s}^{-1}$ and n_{wt} was kept fixed at 1000 (5000) particles.

Non-competitive fit

Variations of simulation	Assembly pathway	Inhibition scheme	$k_{\mathrm{cat,ww}}$	$k_{\mathrm{cat,wm}}$	$\sigma k_{\mathrm{cat,wm}}$	K_{M}	σK_{M}	K_{I}	σK_{I}	n_{wt}
default	1-2-3-6	s1	5	0.5632	0.0552	1093.7900	42.9863	111.8420	9.2601	1000
		s2	5	0.6096	0.0457	1080.4100	19.0614	547.3120	22.8677	1000
		s3	5	0.6496	0.0572	1078.4800	10.6918	1909.0900	78.9730	1000
	1-2-4-6	s1	5	0.7179	0.0547	1660.1600	53.5683	112.4680	9.4571	1000
		s2	5	0.7832	0.0548	1656.9000	27.9256	602.4640	30.8415	1000
		s3	5	0.8603	0.1000	1651.2800	18.4152	2531.7300	181.3130	1000
$k_{\mathrm{off}}(Mut)=0$	1-2-3-6	s1	5	0.6293	0.0517	1088.7000	45.0609	63.0640	6.3257	1000
		s2	5	0.7843	0.0732	1013.1200	39.6375	288.8230	24.1290	1000
		s3	5	1.5688	0.0800	1009.0900	28.1912	726.3880	64.5971	1000
	1-2-4-6	s1	5	0.8372	0.0503	1691.1800	55.3026	63.2462	6.3387	1000
		s2	5	1.0789	0.0826	1603.0600	63.0365	227.2590	24.6183	1000
		s3	5	2.1454	0.0887	1589.1600	39.0893	764.1780	89.4197	1000
$k_{\mathrm{cat,wm}}=0.05$	1-2-3-6	s1	5	-3.77e-17	0.0631	1075.2000	51.0286	93.8528	8.4836	1000
		s2	5	1.43e-17	0.0737	1034.7100	31.3462	480.2400	28.7260	1000
		s3	5	-2.78e-17	0.0856	1057.8600	17.8717	1603.3800	87.3287	1000
	1-2-4-6	s1	5	-7.22e-17	0.0619	1699.0100	61.9976	112.1020	9.2123	1000
		s2	5	-2.57e-17	0.0771	1601.3000	39.3312	545.3560	32.9879 6	1000
		s3	5	4.99e-17	0.1304	1634.5500	27.2994	2141.0600	167.7520	1000
5000 Wt	1-2-3-6	s1	5	0.3244	0.0498	1712.3500	127.1560	524.0010	38.3230	5000
		s2	5	0.3424	0.0448	1651.1500	66.6268	2152.9500	87.8960	5000
		s3	5	0.5967	0.0318	1751.1100	28.2436	5739.4600	142.7860	5000
	1-2-4-6	s1	5	0.3379	0.0534	2416.3200	145.8950	586.3490	44.0233	5000
		s2	5	0.4091	0.0429	2480.5900	69.2567	2329.0100	90.5838	5000
		s3	5	0.7156	0.0529	2540.0500	49.0105	6393.3600	268.0580	5000
$k_{\mathrm{off}}(MX)=1000$	1-2-3-6	s1	5	0.0377	0.0543	1044.8700	31.9633	234.5410	12.9831	1000
		s2	5	1.99e-17	0.1203	1078.9800	32.3357	1141.5200	92.7345	1000
		s3	5	1.53e-16	0.1545	1058.7500	26.90	1997.9600	188.2970	1000
	1-2-4-6	s1	5	0.0402	0.0631	1690.6300	42.3957	328.5420	18.9600	1000
		s2	5	4.24e-17	0.1020	1682.5000	32.7013	1283.6300	86.6705	1000
		s3	5	-3.59e-17	0.1907	1619.2700	43.3177	1941.7800	227.2240	1000

Table 4.6: Fit parameters of the non-competitive fit with a fix $k_{\mathrm{cat,ww}}$: $k_{\mathrm{cat,wm}}$, K_{M}, and K_{I} are fit parameters and σ their respective standard deviation. The value of $k_{\mathrm{cat,ww}}$ was kept fixed at $5.0\,\mathrm{s}^{-1}$ and n_{wt} was kept fixed at 1000 (5000) particles.

## 4.4   Application of the simulation to experiments

In order to examine if the simulation reflects the experimental observations of the inhibition behavior of mutant spastin on wild type spastin's activity, the measured and simulated data points were compared. For this purpose the experimental concentrations had to be converted into the number of wild type subunits used in the simulation, in this instance using 5000 wild type particles, and the default parameter set. To this end, the concentration of wild type spastin which was held fixed at $c_{\mathrm{spastin,wt}} = 5.88 \cdot 10^{-7}$ M was converted to make it consistent with the fixed number of wild type subunits ($n_{\mathrm{wt}} = 5000$). The concentration of mutant spastin was scaled accordingly to this gauging. The extrapolated turnover rate of the measurement $k_{\mathrm{max}} \approx 3.8\,\mathrm{s}^{-1}$ was slightly higher than the value of k_{max} obtained from the simulations ($k_{\mathrm{max,1236}} = 3.7\,\mathrm{s}^{-1}$ and $k_{\mathrm{max,1246}} = 3.3\,\mathrm{s}^{-1}$). Hence the measured turnover rate was adjusted to the simulated value. Figure (4.11) shows the calibrated experimental data in red circles and the simulated data in blue crosses. It can be seen that the inhibition patterns obtained from simulation and experiment are similar. In particular inhibition scheme 2 shows a strong resemblance to the experimental data. However, from this plot it is not clear which inhibition scheme matches the experimental data best.

In experiments, the concentrations of wild type and mutant spastin are essential values for calculating the inhibited turnover rate k_{obs}. Their determination however is an inherently error-prone procedure. This can lead to significant systematic errors in the calculated ratio of mutant to wild type concentration. An error of 20% in each concentration leads to differences in the ratio of both species by a factor ranging from 0.67 to 1.5. Taking this into account, the re-scaling of the measured data to the simulated results was done manually in such a way that they matched the respective inhibition schemes best (figures 4.12 and 4.13). Subsequently the scaling factors were recorded. As already indicated in figure (4.11), inhibition scheme 2 shows the best agreement for both assembly pathways (figures 4.12(b) and 4.13(b)). Furthermore the correction for the systematic error is given by a factor of 1.3, which is also in the range given by the experiments. The qualitative shape of the simulation according to inhibition scheme 1 differs clearly from the experimental data (figures 4.12(a) and 4.13(a)). The correction factor of 0.25 lies clearly outside the estimated error range. Inhibition scheme 3 results in data points that can be overlaid with the experimental inhibition data, but in order to achieve this an improbably high scaling factor of 4.0 was neccessary.

Considering the agreement of simulated and experimentally measured data in the qual-
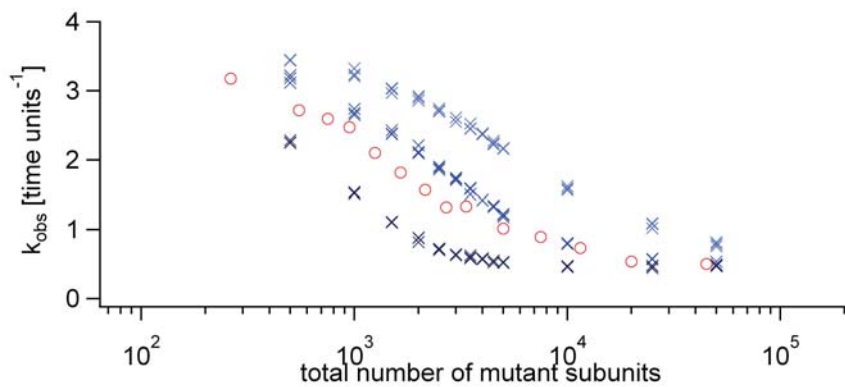
(a) 1-2-3-6
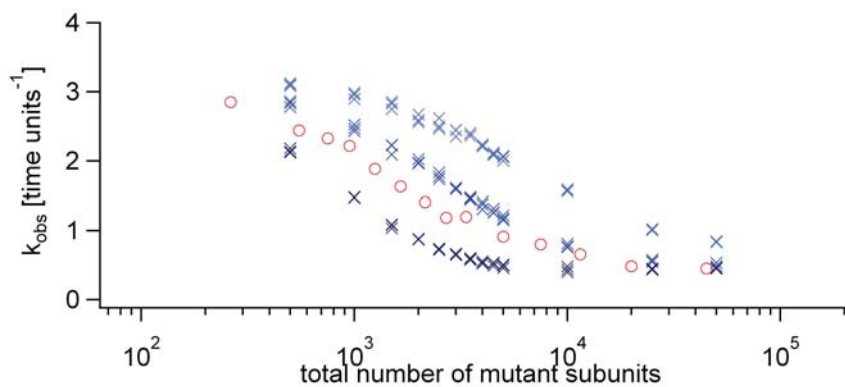
(b) 1-2-4-6

Figure 4.11: Comparison of measured and simulated data: experimental data are represented using red circles, and simulated data are represented as blue crosses (inhibition scheme 1 is coded in dark, inhibition scheme 2 in medium, and inhibition scheme 3 in light blue). Panel (a) shows the data obtained from the 1-2-3-6, and (b) that from the 1-2-4-6 assembly pathway. The data are quite similar, however no clear overlay can be found.
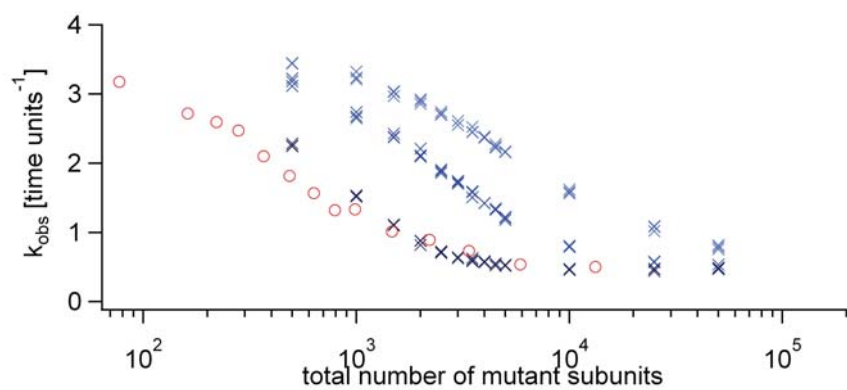
(a) Inhibition scheme 1
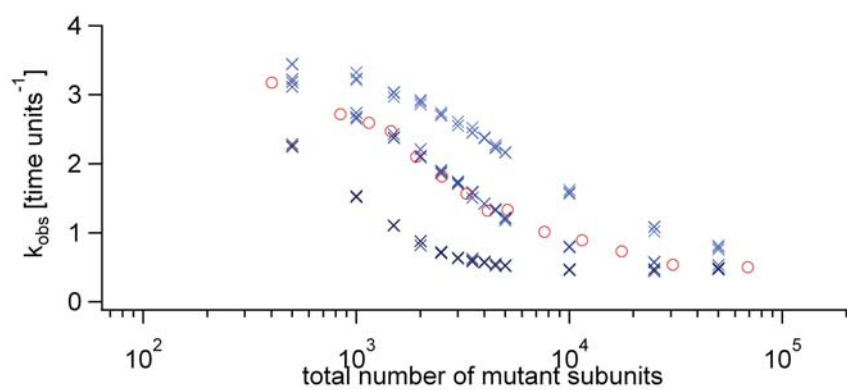
(b) Inhibition scheme 2
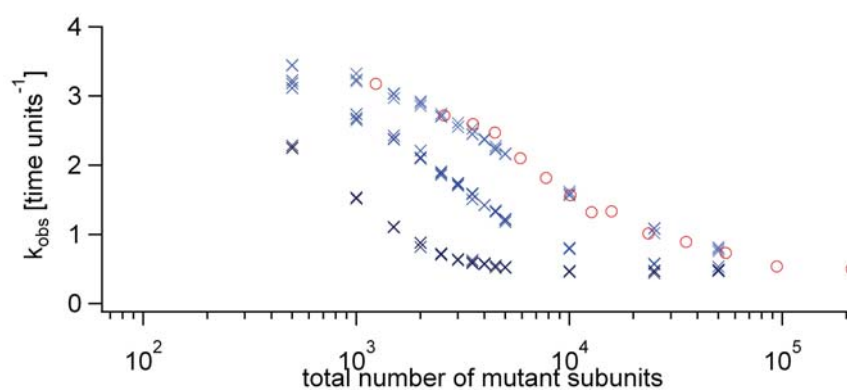
(c) Inhibition scheme 3

Figure 4.12: Comparison of measured and simulated data obtained from the 1-2-3-6 assembly model: the experimental data were adjusted such that the inhibition pattern exhibits a clear overlap with the simulated inhibition schemes. To this end, the concentrations used in the experiments were multiplied by a factor x (see text), whereas the turnover rate was not adjusted for each simulation. Labeling is the same as in figure (4.11).
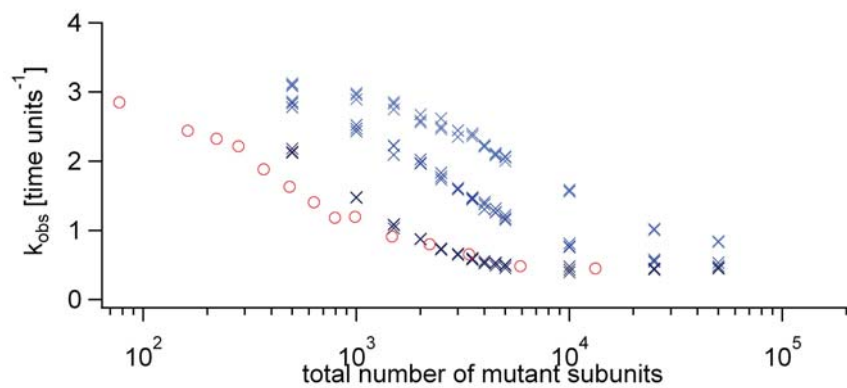
(a) Inhibition scheme 1
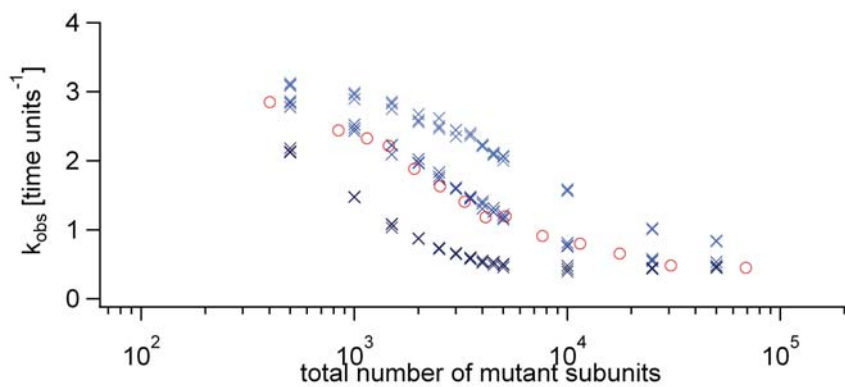
(b) Inhibition scheme 2
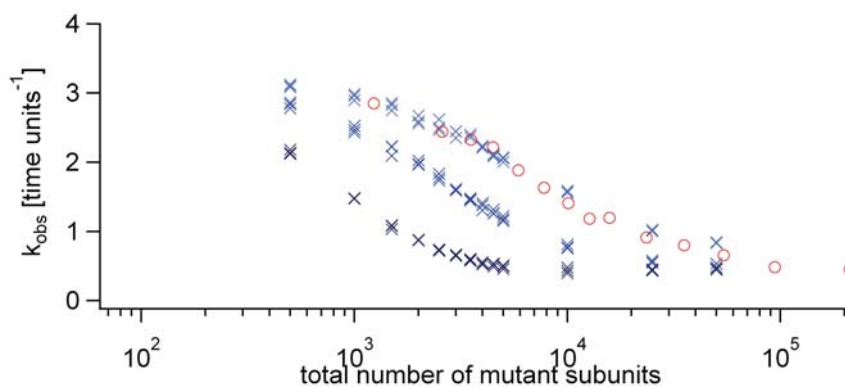
(c) Inhibition scheme 3

Figure 4.13: Comparison of measured and simulated data obtained from the 1-2-4-6 assembly model: the experimental data were adjusted such that the inhibition pattern exhibits a clear overlap with the simulated inhibition schemes. To this end, the concentrations used in the experiments were multiplied by a factor x (see text), whereas the turnover rate was not adjusted for each simulation. Labeling is the same as in figure (4.11).

itative shape of the inhibition behavior, inhibition scheme 1 is ruled out as a possible explanation for the interaction between mutant and wild type subunits. This inhibition scheme does not reflect the experiment as the mutants inhibit the activity of the wild type enzyme too strongly at low mutant concentrations: in simulations the addition of 10% mutants led to a reduction in the activity by nearly 50%, whereas in experiments 20% mutants were neccessary to achieve this effect.

Taking into account the calibration values of experimental data, inhibition scheme 3 is not favored due to the large correction factor, which falls out of the boundaries set by the systematic error of the ratio of mutant and wild type. The simulation according to this inhibition scheme does not inhibit the turnover of wild type as strongly as is observed in experiments, where about 50% mutants were required to inhibit the activity of wild type by 50%.

Inhibition scheme 2 does resemble the experimental data both in the inhibition pattern and the scaling factor, which lies within the tolerance region of the systematic errors.

These considerations in turn provide an important and also unexpected insight into the inhibition mechanism of spastin: they show that one mutant subunit with a single point mutation does inhibit both of its direct neighbors, and other wild type subunits remain unaffected. This suggests that either the subunit has to undergo a large conformational change in order to cooperate with other subunits, or the effect of binding translates over a large region of the subunit. So far this inhibition pattern has neither been studied nor described systematically elsewhere. Furthermore, the results presented here show that the nearest neighbor inhibition scheme, that was suggested previously in [P3], does not hold true when hexamers are assumed to be the catalytically active form. In addition, the inhibition scheme 1, which is a conversion of the classical inhibition of substrate binding of the Monod-Wyman-Changeux model (MWC-model), does neither describe the experiments qualitatively nor quantitatively. Thus the behavior of spastin cannot be described by a tensed and relaxed state of the hexamer as it is done in the MWC-model.

Chapter 5

Results III: Effect of MAPs on ATPase activity

Stoppin-Mellet et al. (2002) have used microtubule associated proteins (MAPs) to bind microtubules to the surface of cover slips. As MAPs have the function of stabilizing microtubules by binding to their surface, the question arises if they also have an inhibitory effect on enzymes interacting with the microtubules.

5.1 Influence of MAPs on spastin's activity

To study the effect of MAPs on microtuble severing enzymes, in particular spastin, a coupled enzymatic assay was performed as described in chapter (2.1.3). Increasing amounts of MAPs were pre-incubated with $25\,\mu$M microtubules at room temperature for 5 minutes. This assay was performed using $160\,$nM spastin and $2\,$mM ATP. As the MAPs used here were a byproduct of the tubulin preparation and hence are a mixture of MAP2 and tau, their average concentration in $\mathrm{mg\,ml^{-1}}$ was obtained by measuremening the absorption at $280\,$nm. The ratio of microtubules and MAPs was calculated on this basis.

The resulting decrease in the absorption at $340\,$nm over time ($\mathrm{dA_{340}/d}t$) was fitted linearly using the software IGOR. The slopes obtained this way are displayed versus the percentage of added MAPs with respect to $25\,\mu$M of inserted microtubules (figure 5.1). The plot shows that even though the concentration of MAPs is increased, no clear change in the slope, and hence in the hydrolysis of ATP, can be observed. The measurement at 100% MAPs is a negative control, where only MAPs and no microtubules were present, showing that MAPs alone do not alter the catalytic activity of spastin. These measurements show no
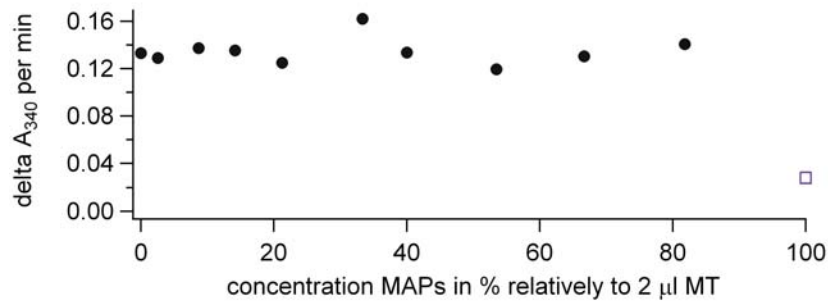
Figure 5.1: The obtained values for $\mathrm{d}A_{340}/\mathrm{d}t$ are shown as a function of increasing concentration of MAPs. The latter is given in relation to $25\,\mu\mathrm{M}$ microtubules, which were inserted in the measurement. The measurement at 100% MAPs is a controll measurement where no microtubules are present.

significant change of catalytic activity of spastin, even at high MAP concentrations. That is a surprising result, as MAPs are very large proteins (about $200\,\mathrm{kDa}$) which decorate the surface of microtubules and therefore should significantly decrease the available contact surfaces for spastin.

5.2 Influence of MAPs on kinesin's motility

A further study regarding the effect of MAPs was carried out in a gliding assay, as described in chapter (2.2.3), where the gliding velocity of microtubules above kinesin was investigated. This is of interest because an interaction between MAPs and microtubules should reduce said velocity. A cover slip was coated with a chimeric kinesin1 mutant, consisting of a *Drosophila* head and human tail in which exposed cysteins were mutated to serins (C45S, C338S). Microtubules, which had been pre-incubated with MAPs for 5 minutes, were added and their gliding behavior was observed. In the case that only microtubules were present at the initialization of a measurement (which was several seconds after addition of microtubules into the chamber) many microtubules were already bound to the kinesin and were mobile (figure 5.2(a)). The addition of MAPs changed the amount and the behavior of bound microtubules significantly. Compared to the large amount of microtubules bound in the absence of MAPs, in their presence no bound microtubules were found for at least 5 minutes after initialization (figures 5.2(b) and (c)). After that only few microtubules interacted with the kinesin, but after about 15 minutes that number started to increase (figure 5.2(d)). However, a comparable number of bound microtubules, as in the

ratio MT:MAPs	time after adding MT [min]	$v_{gliding}$ [nm s^{-1}]
1 : 0 (no MAPs)	0.5	317
1 : 1	10	214
1 : 1	15	264
1 : 1	25	255
1 : 2	10	175
1 : 2	15	170

Table 5.1: Mean velocity determined by a Gaussian fit of the data obtained from the gliding assays (figure 5.3). The ratio of microtubules (MT) to MAPs was varied.

measurements without MAPs, was not reached during the observation time. Furthermore the length of the binding filaments was decreased by about 50%.

The main goal of these gliding assays was the determination of the effect of MAPs on the velocity of kinesin. For this time series were recorded. Two ratios of MAPs to microtubules were tested (1:1 and 2:1). The calculated velocities of single microtubules (see chapter 2.2.3), in the presence and absence of MAPs respectively, are shown in the histograms of figure (5.3).

Each velocity distribution was fitted with a Gaussian function in order to determine the mean velocity. The obtained values are displayed in table (5.1). It can be seen that the highest velocity of $317\,\mathrm{nm\,s^{-1}}$ is measured for the case that only microtubules were interacting with the kinesin. The addition of MAPs led to a reduction of the net velocity. In case of the addition of MAPs in a one to one ratio to microtubules, the resulting velocity is reduced by about one third, but with increasing time the velocity seems to increase again. In the case that more MAPs were added (2:1), the apparent reduction is even more prominent as the velocity is reduced to 50%. However, the values presented here are the average net velocities that a microtubule exhibits over the observation time. There could be alternative explanations for this behavior: one is that the velocity itself is reduced by the interaction with MAPs. A further one could be a stop and go mechanism, where the maximum velocity is the same as in the case without MAPs. This would also result in a lower apparent velocity.

(a) microtubules only

(b) microtubules pre-incubated with MAPs 1:1, 1 min after initiation

(c) microtubules pre-incubated with MAPs 1:2, 1 min after initiation

(d) microtubules pre-incubated with MAPs 1:2, 21 min after initiation
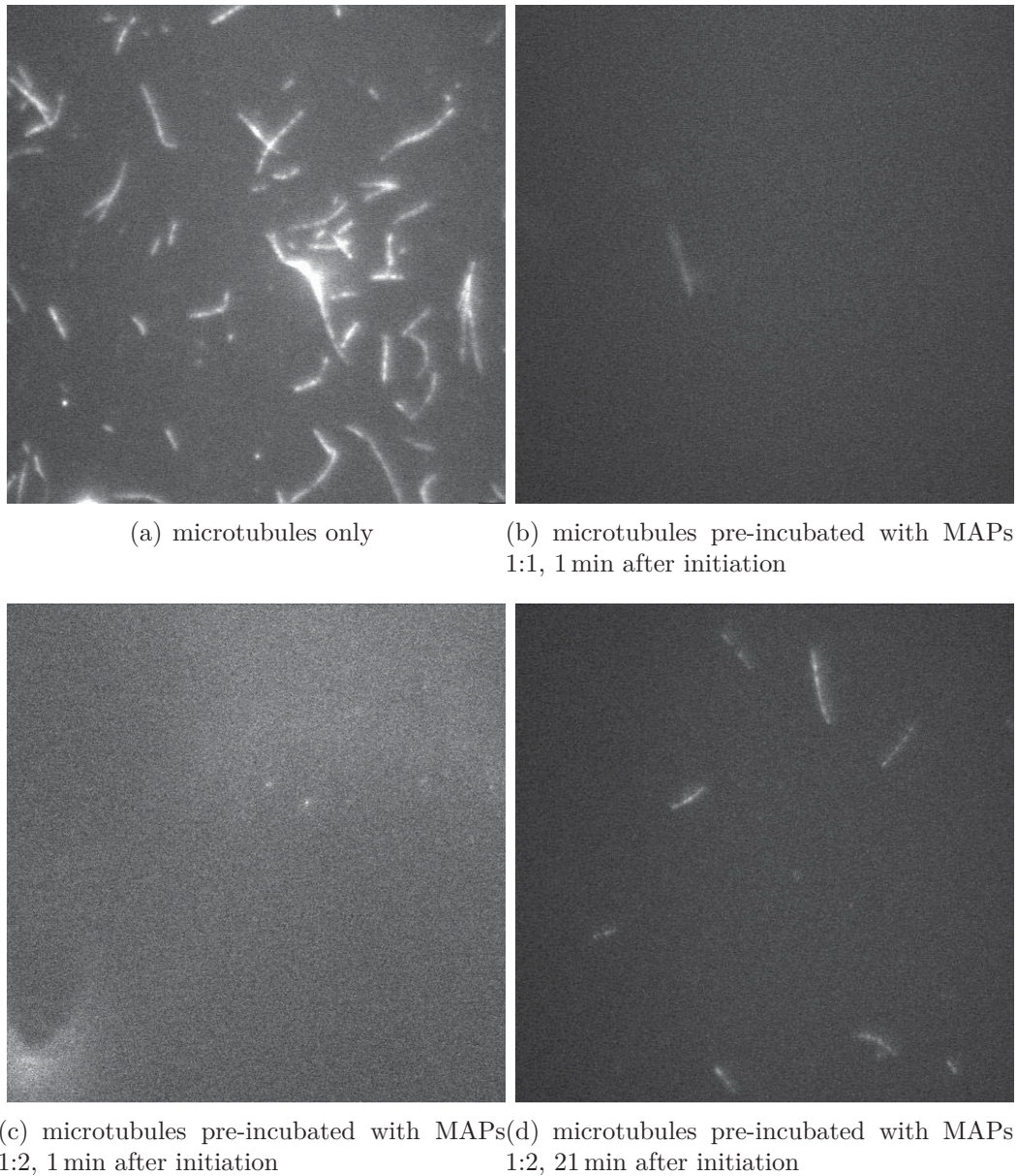
Figure 5.2: Binding of microtubules to a kinesin coated surface in the presence and absence of MAPs: panel (a) shows microtubules bound to a kinesin coated cover slip after 1 minute. Panels (b) and (c) show that significantly less microtubules are bound to a surface that is incubated with MAPs. In panel (b) the ratio of MAPs to microtubule is 1:1, in panel (c) 2:1. After 21 minutes more microtubules pre-incubated with MAPs bind.
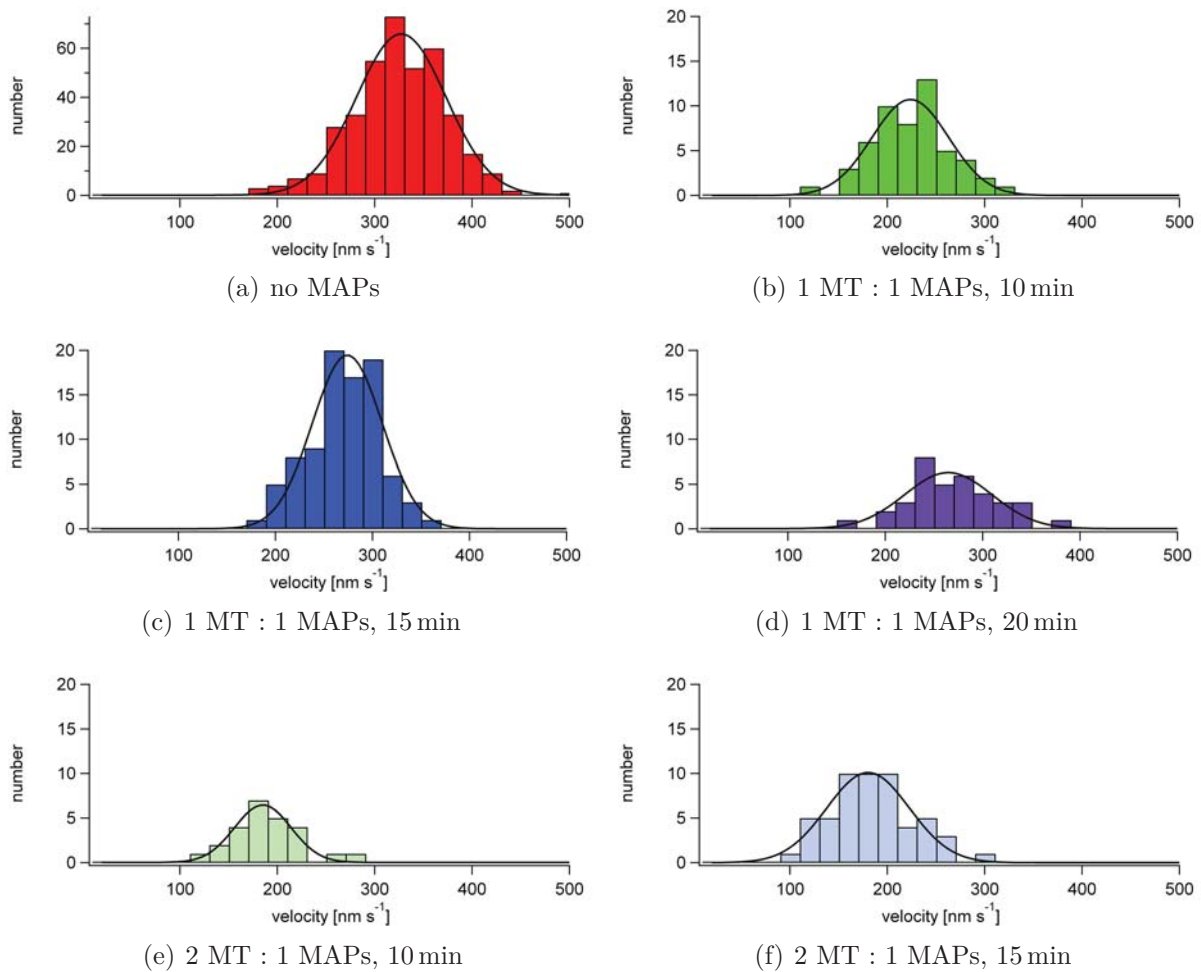
Figure 5.3: Distribution of velocities measured in gliding assays: a histogram of the number of microtubules exhibiting different gliding velocities is shown for each ratio of microtubules (MT) to MAPs at different times after the addition of microtubules. The histograms were fitted with a Gaussian distribution (black line).

5.3   Investigation of interaction force between MAPs and microtubules

The interaction force between MAPs and microtubules is interesting to study as it might explain the observations above. To this end experiments using AFM were performed. The MAPs were covalently coupled to the cantilever tip and the microtubules were fixed to cover slips, as described in chapter (2.2.2). As a negative control a surface covered with mPEG was used. The experiments were performed at room temperature (about 21°C) in BRB80+ and $4 \, \mu$M taxol.

As it could not be ascertained that the cover slip was coated completely with microtubules, reference measurements were executed, both on the glass alone and on silanized glass coated with additional antibodies. Representative force-distance curves are shown in figure (5.4).

From the measured force-distance curves the maximal force $F_{\max}$ and the interacting length l was determined. For the negative control using mPEG the force-length distribution is displayed in figure (5.5). In order to ascertain that the measured forces did not result from interactions between the MAPs and the uncoated glass surface, the force generated by MAPs with glass, mPEG and antibodies was determined (figure 5.6). It can be seen that the force between MAPs and glass is significantly higher compared to the interaction between MAPs and mPEG or MAPs and antibody or even MAPs and microtubule respectively. However, the force between MAPs and microtubules lies within the same regime.

Measurements with the addition of microtubules to glass slides coated with anti-β-tubulin antibodies were performed in an analogous way. The resulting force-distance distribution is displayed in figure (5.7(a)), where two populations of force-distance correlations can be distinguished. They correspond to interactions between MAPs and antibodies and MAPs and microtubules respectively. It can be seen that the interaction forces between MAPs and microtubules are on average lower compared to the force between MAPs and antibodies. Furthermore some measurements show an increase in the binding length.

To elucidate if this interaction is of ionic nature the concentration of salt in the buffer was increased by the addition of $300 \, \mathrm{mM}$ and $600 \, \mathrm{mM}$ potassium acetate respectively. The results are shown in figure (5.7(b)) and (c). The two populations are still present but their separation becomes less prominent. The interaction length does not change drastically with increasing salt concentrations. The force of the interaction, however, is affected: the data

(a) glass

(b) glass

(c) mPEG

(d) mPEG

(e) antibody

(f) antibody

(g) microtubules

(h) microtubules
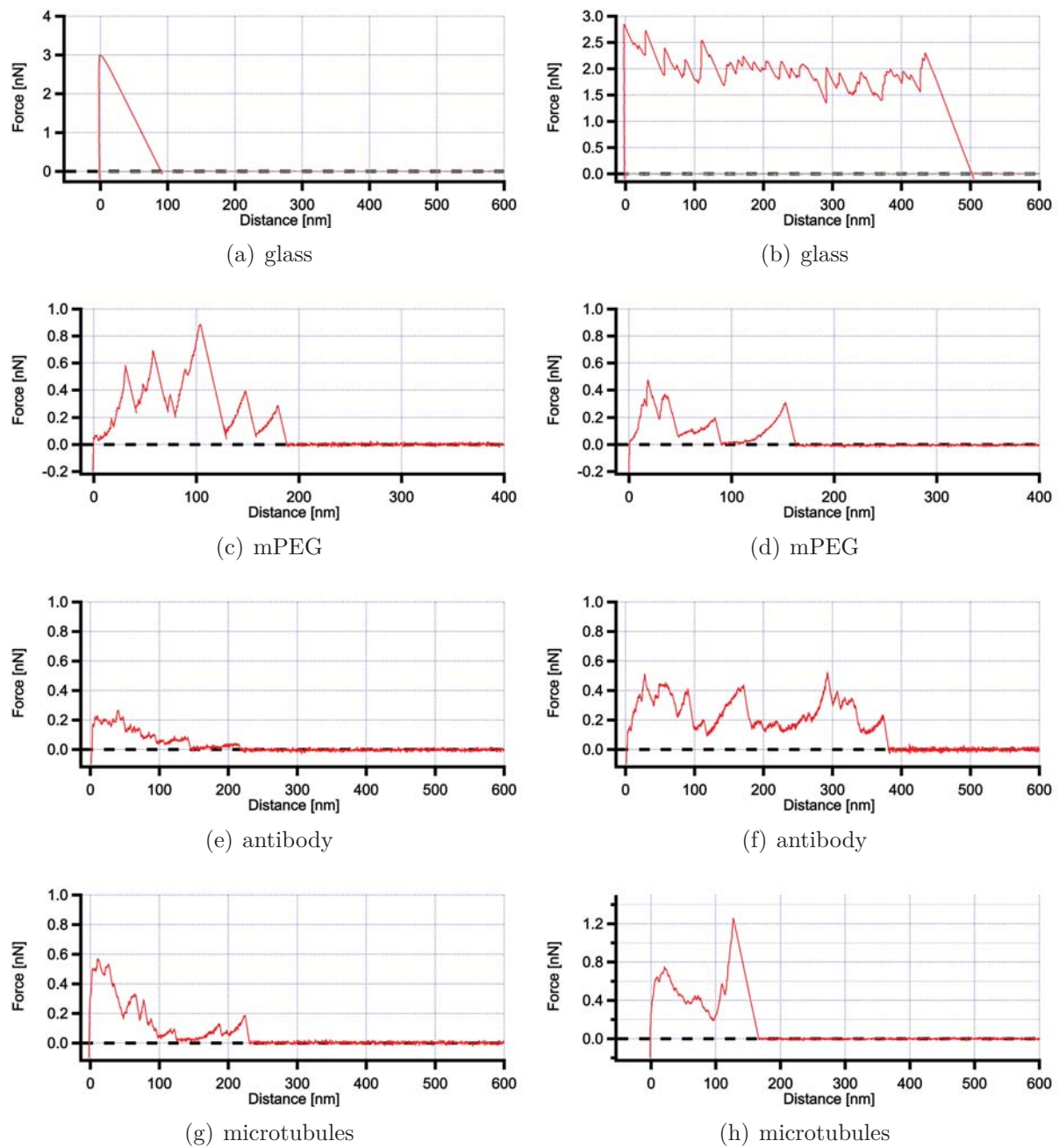
Figure 5.4: Representative force-distance curves, which were obtained from experiments using different surfaces. MAPs were attached to the cantilever tip in each measurement. Panels (a) and (b) were performed on pure glass, (c) and (d) on a surface covered with mPEG, (e) and (f) on an antibody coated surface, (g) and (h) with additional microtubules. The force generated by the interaction between MAPs and glass is significantly higher compared to the rest.
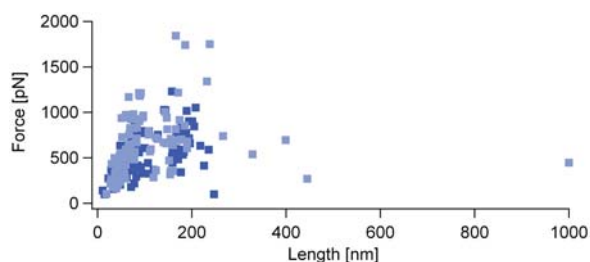
Figure 5.5: Force-length distribution of the interaction between MAPs and mPEG. Light blue and dark blue squares correspond to two measurements under the same conditions
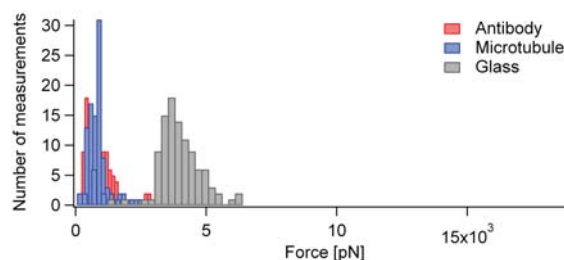
Figure 5.6: Distribution of forces generated by MAPs on glass (grey), mPEG (blue), and antibody (red)

overlay of measurements, depicted in figure (5.7(d)) displays that the interaction between MAPs and antibodies is not affected significantly by increasing salt concentration (figure 5.7(e)), whereas the interaction between MAPs and microtubules shows deviations. This can be seen more clearly in the histograms: figure (5.7(g)), showing the force between MAPs and antibodies, displays to significant change of the force obtained from the measurements using different salt concentrations, whereas figure (5.7(f)), showing the force between MAPs and microtubules, shows a shift of the interaction force. This leads to the conclusion that the interaction between MAPs and microtubules is based on ionic interaction.

As mentioned above, a high concentration of anti-β-tubulin antibody as well as a high concentration of microtubules are used to cover the surface. However, it is possible that some spots were not coated. Hence it would be of advantage if the position of a microtubule is known, i.e. by imaging it, before measuring the interaction force. To this end, microtubules, coated using the ratios mentioned above, were imaged in air. However, it was found that the number of microtubules bound was smaller than initially assumed (figure 5.8(a)) and that also aggregates of microtubules were present. Using the same conditions but with a different silane (Vectabond®), more microtubules were bound (figure 5.8(b)). The imaging in aqueous solution did not result in satisfying quality. This shows that the imaging of microtubules in aqueous solution is challenging, as also revealed in personal communications with Dr. Iwan Schaap.

(a) 0 mM potassium acetate

(b) 300 mM potassium acetate

(c) 600 mM potassium acetate

(d) Microtubules

(e) Antibody

(f) Force histogram: microtubules

(g) Force histogram: antibody
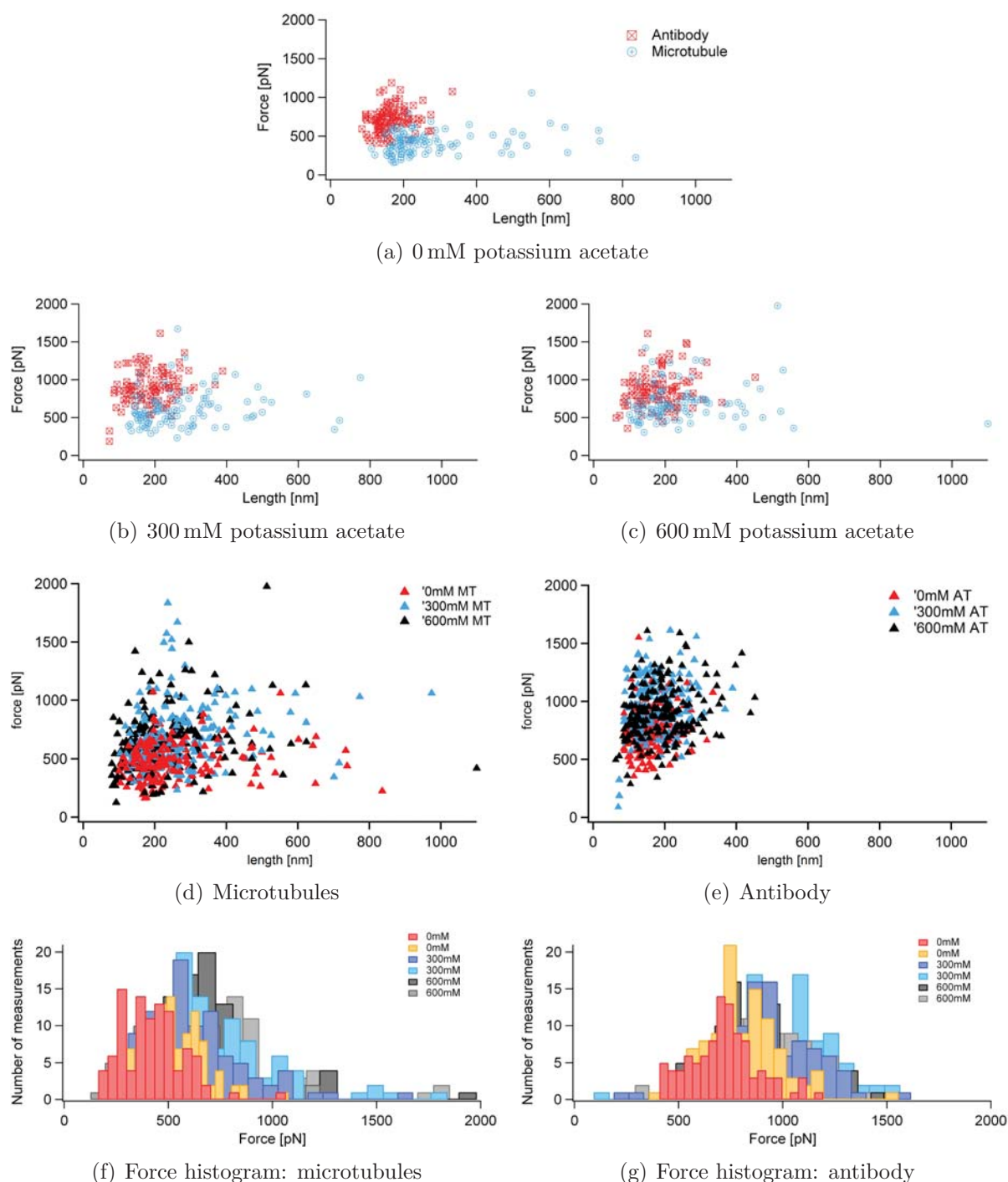
Figure 5.7: Effect of increasing potassium acetate concentration on the binding force between MAPs and microtubules, and MAPS and antibody respectively: panels (a), (b) and (c) show the force-distance distribution of the interaction between MAPs and microtubules (blue squares) and antibody (red circles) respectively. Panel (d) displays an overlay of the force-distance distributions of MAPs and microtubules under different salt concentrations, panel (e) shows the same for MAPs and antibodies. Panels (f) and (g) picture the force of MAPs – microtubule and MAPs – antibodies in histograms respectively, under different salt concentration with two series of measurements each.

(a) Dimethyldichlorosilane
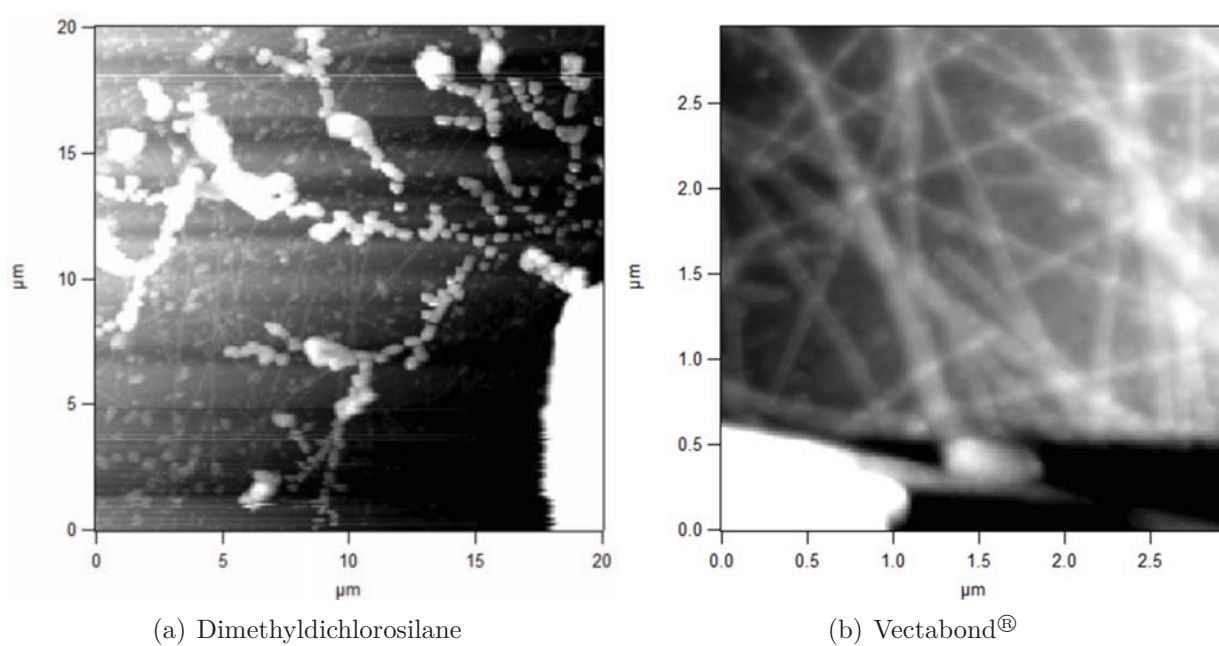
(b) Vectabond®

Figure 5.8: Microtubules bound to antibodies, which were bound to Dimethyldichlorosilane and Vectabond® respectively.

Chapter 6

Discussion and Outlook

In the work presented here, three main subjects were addressed: the influence of microtubule associated proteins (MAPs) on specific AAA ATPases, different possible assembly pathways of hexameric enzymes, and the inhibitory effect of mutant subunits on the catalytic activity of hexameric enzymes. For all three subjects the main focus was placed on the microtubule severing enzyme spastin.

6.1 Studies on MAPs

Effect on turnover rate of spastin

Measurements performed with a coupled enzymatic ATPase assay showed that a mixture of MAP2 and Map tau proteins alone does not induce an increase in the turnover rate of spastin. However, the addition of microtubules does increase the activity of spastin as shown by Eckert et al. (2012a). The addition of more MAPs with respect to a constant concentration of microtubules does not lead to measurable changes in the catalytic turnover rate of spastin as shown in figure (5.1). This indicates that MAPs do not have a significant effect on spastin's activity. This is in accordance with experiments on axons performed by Yu et al. (2008). Interestingly this group showed that katanin, another AAA ATPase severing microtubules, is negatively influenced by the presence of tau.

Hence it might be interesting to corroborate the effect of MAPs on the catalytic turnover rate of katanin above purified tubulin using the biochemical assay as well as by an optical severing assay using TIRFM. Furthermore these results indicate that spastin and katanin, even though belonging to the same family of AAA ATPase enzymes, seem to have different

biding sides or binding mechanisms to the microtubule. However, it might also be possible that the interaction force between MAPs and microtubules is low enough that spastin may push the binding MAPs away, which can be pictured by a chain lying on an uneven surface rather than a sticky tape glued to it.

Effect on gliding velocity of kinesin

To this end a gliding assay using kinesin 1, which can pull a cargo of up to 5-6 pN (Svoboda and Block, 1994), was performed. The measurement showed that the average gliding velocity of kinesin on microtubules is about $v_1 = 320\,\mathrm{nm\,s^{-1}}$. When microtubules were pre-incubated with MAPS, this velocity was reduced significantly as shown in figure (5.3). The reduction depended on two factors: the ratio of MAPs to microtubules and the time lapse, i.e. the time between the addition of microtubules and the start of observation. It was found that a higher concentration of MAPs led to a larger decrease of the gliding velocity.

Kinesin 1 is a highly processive motor and therefore the following explanations for this observation can be thought of: the binding of MAPs on the microtubule leads to an overall decrease of the gliding velocity to a value $v_2 < v_1$ as kinesin has to bypass the MAPs decorating the microtubule. These lateral movements cannot be tracked by measurements using TIRF and therefore result in a lower observed velocity.

Another possible explanation for the observed reduction of the average velocity is a stop and go mechanism: the kinesin walks on the microtubule until an obstacle is encountered and stops walking. As other kinesins are still attached to the microtubule and therefore keep pushing it forwards the barrier can be overcome and the microtubule is transported with the non-reduced velocity v_1 in between stops.

However, it seems that with increasing time the mean velocity of the microtubules transported by kinesin increases again. One explanation for this phenomenon could be that during the measurement the microtubule twists until that all MAPs are facing away from the kinesin leaving free microtubule surfaces for kinesin to bind. To investigate this more closely measurements over a longer period of time after initializing the experiment by the addition of microtubules with MAPs to kinesin should be performed. Furthermore, the time resolution of a TIRF microscope is not good enough to distinguish a stop and go process from a lateral movement. To get further insight into the gliding behavior of kinesin 1 on microtubules decorated with MAPs other techniques have to be employed. An optical trap might be the instrument of choice as it has the necessary spacial and temporal

sensitivity.

Interaction with microtubules

In order to get a deeper understanding of the interaction force between microtubules and MAPs, force-distance curves were obtained using AFM. MAPs were coupled covalently to the cantilever tip and microtubules were fixed on cover slips. Control measurements on glass, silane, and antibodies were performed. mPEG was used as a negative control. It could be shown that the interaction force between MAPs and glass is higher than the interaction force between MAPs and mPEG and antibodies respectively, see figure (5.6). Hence it is possible to examine if the spot on the surface, where the measurement is performed, is at least covered with antibodies and therefore possibly with microtubules. The force-distance correlation depicted in figure (5.7(a)) displays two populations which correspond to interactions between MAPs and antibodies and MAPs and microtubules respectively. With increasing salt concentrations the separation becomes less prominent but is still visible as shown in figures (5.7(b)) and (c). Furthermore it could be shown that the interaction between MAPs and microtubules is affected by increasing the salt concentration (figure 5.7(d)), whereas the interaction between MAPs and antibodies is not (figures 5.7(e), (g), and (g)). The interaction force is increased by salt concentrations, as shown in figure (5.7(f)). However, the interaction force between MAPs and mPEG lies in the same force regime as the force between MAPs and microtubules, which might result from hydrophobic effects. As this is of great importance a material has to be found with which MAPs interact less strongly. Furthermore if this material could be used to cover the glass slides in such a way that MAPs can only interact with either this negative surface or the microtubules, a clean measurement setup for the interaction force between MAPs and microtubule could be made.

Also a more detailed study on the effect of the various salt concentrations would be interesting, especially for further investigations with additional spastin, whose activity also depends on the salt concentration in the assay buffer. To this end it would be advantageous to find the potassium acetate concentration at which the interaction force is at its maximum, and then add spastin and vary the salt concentration in the severing buffer accordingly.

Proposed further experiments

For all measurements presented here a mixture of MAP2 and tau protein, which occur naturally in porcine brains, was used. However, the exact relative ratio of these two proteins is unknown. Furthermore it is known that these two microtubule associated proteins can behave differently in the interaction with microtubules and kinesins (Dehmelt and Halpain, 2004). The effect of MAPs (tau and MAP2) on kinesin was already investigated by various groups, e.g. by (von Massow et al., 1989, Dehmelt and Halpain, 2004, Marx et al., 2006). To this end different isoforms of these MAPs were expressed and purified. von Massow et al. (1989) showed that MAP2 inhibits kinesin only under certain conditions. If using the same conditions as chosen in the experiments performed in this work, i.e. binding MAP2 to microtubule, the motility was not affected. The tau protein on the other hand exhibits an inhibitory effect on kinesin, as shown by Dixit et al. (2008). As mentioned above a mixture of these two microtubule associated proteins occurs in nature. For further investigations in this direction it might be interesting to express both proteins individually and change the relative ratio of them in order to study their combined effect on kinesin in greater detail.

For experiments with the severing enzymes spastin and katanin, only the effect of the tau protein was investigated so far. Further experiments in this regard could entail studying the effect of MAP2, both on spastin and on katanin. Also a mixture of both MAPs could be of interest, as discussed for kinesin. Furthermore a microscopic severing assay should be performed, with MAPs and tau protein for spastin and katanin respectively. This is because it has been shown by Eckert et al. (2012a) that the inhibitory effect of mutant spastin is more prominent in severing assays than in coupled enzymatic ATPase assays. This might also be true for MAPs, if they show an effect on the activity of the severing enzymes.

Finally, MAP2 and tau could also bind differently to the microtubule and hence exhibit different interaction forces and lengths. To study this in more detail, experiments using AFM to obtain force-distance relations should be repeated with expressed and purified MAP2 and tau respectively. However, it should be ascertained that the surface is sufficiently covered with microtubules. This can be done by imaging the microtubule in buffer. This could not be achieved during the measurements performed so far. In personal communications Dr. Iwan Schaap revealed that imaging in aqueous solutions using AFM is very sensitive and hence extremely difficult to perform. Therefore it might be preferable to find an non-interacting material to cover the spots where no microtubules are present,

as mentioned above. Such a setup could be used to distinguish interactions of MAPs and microtubules from interactions with MAPs and background.

6.2 Assembly of hexamers

The main goal of this work was to elucidate the function and behavior of the microtubule severing enzyme spastin. To this end both the catalytic activity of wild type spastin alone and in the presence of mutant spastin subunits was studied using kinetic Monte Carlo simulations. It is known that mutant spastin has an inhibitory effect on the catalytic turnover rate of wild type enzyme (White et al., 2007, Eckert et al., 2012a). Spastin, and also katanin, belong to the family of AAA-ATPase proteins. From analogy considerations to other AAA-ATPase proteins like ClpB it is generally assumed that the catalytically active form of spastin is a hexamer. However, the formation process of the hexamer is still unknown. As the probability for the simultaneous reaction of six monomers into a hexamer is negligible, intermediates have to be formed. A dimeric population of spastin could be found in experiments, showing that the formation of hexamers includes at least the dimerization process (Eckert et al., 2012b).

Hence, two explicit models regarding the assembly pathway (which are termed the 1-2-3-6 and 1-2-4-6 assembly pathway respectively) were introduced in the course of this work. These pathways can also be applied to other hexameric enzymes, as also suggested by Chakraborty et al. (2012) for the AAA ATPase Rubisco activase. The oligomerization model introduced there involves dimeric and tetrameric intermediates on the pathway of the formation of hexamers, and corresponds to the 1-2-4-6 assembly pathway presented in this work. The ATP turnover rate as a function of the number of wild type subunits (k_obs) was simulated for both assembly pathways. It could be shown that the resulting k_obs follows a similar course in both pathways, as shown in figure (3.4). Furthermore, the turnover rate is proportional to the amount of monomers incorporated in hexamers. The dependency of k_obs on the total number of monomers resembles a Michaelis-Menten kinetic and hence was fitted by this function, given by equation (2.32). From this the half-maximal activation constant K_m was obtained. The value of K_m is lower in the case of the 1-2-3-6 assembly pathway ($K_\mathrm{m,1236} = 1008 \pm 25$ particles) compared to the value obtained from the 1-2-4-6 pathway ($K_\mathrm{m,1246} = 1645 \pm 38$ particles). From this follows that in the 1-2-3-6 assembly pathway less subunits are necessary to achieve the same catalytic turnover as in the 1-2-4-6 pathway. That in turn shows the significant role a large pool of

intermediate species plays in the hexamerization process: in the 1-2-3-6 assembly pathway the step following dimerization is the formation of trimers, which can occur only if sufficient monomers and dimers are present. Likewise for the tetramerization process of the 1-2-4-6 assembly pathway to occur, a large amount of dimers is needed.

At low enzyme concentrations many monomers are present in both proposed assembly pathways, as can be seen in figure (3.5). Dimers are formed by the oligomerization of two monomers, therefore some time has to pass until a pool of dimers is available. This step is valid for both assembly pathways. The crucial difference are the further oligomerization processes: the pool of trimers is produced faster than the pool of tetramers as the trimerization process depends on the pools of dimers and monomers, of which the latter are present from the start. Tetramerization, however, depends only on the pool of dimers. Hence a sufficiently large pool of dimers has to be created before tetramers can be formed. This can be seen in figures (3.6(a)) and (b): the population of monomers in the 1-2-3-6 assembly pathway is reduced faster than in the 1-2-4-6 pathway. This could be expected due to the dimerization and trimerization steps both reducing the pool of available monomers. In addition trimerization also reduces the amount of free dimers. Hence more dimers and monomers can be found in the 1-2-4-6 than in the 1-2-3-6 assembly pathway. However, at high enzyme concentrations the intermediates present in both assembly pathways converge to a comparable level, indicating that at high enzyme concentrations the turnover is independent of the assembly pathway. Furthermore, hexamerization in the 1-2-3-6 assembly pathway is also likely to occur faster as only trimers are needed, whereas in the 1-2-4-6 assembly pathway pools of both dimers and tetramers are required. These considerations explain the observation of the lower value of $K_{\mathrm{m,1236}}$ compared to $K_{\mathrm{m,1246}}$.

Dimerization

The effect of the individual forward rates (k_{12}, k_{23},...) respectively on the distribution of the intermediate species was investigated by increasing each rate individually by a factor of 100. The increase of the dimerization rate k_{12} led to a higher amount of dimers, as expected, and this in turn resulted in a reduction of free monomers as well as an increase of the amount of tri- and tetramers respectively. Remarkably, the formation of hexamers however was is not influenced significantly. Experiments showed that the catalytic turnover rate of wild type spastin, which is proportional to the disassembly rate of hexamers, is about 1 ATP per second, and the addition of microtubules increases this value to $4\,\mathrm{ATP\,s^{-1}}$ (Eckert et al., 2012a). Artificially engineered dimers, which consist of two monomer spastin subunits

parameter set	1-2-3-6		pseudo-mono-molecular	1-2-4-6	
	K_{m}	δK_{m}	K_{m}	K_{m}	δK_{m}
default	1008	25	990	1645	38
$100 \cdot k_{12}$	451	7	9.9	346	9
$100 \cdot k_{23(24)}$	557	17	504	1858	77
$100 \cdot k_{36(46)}$	458	9	990	1060	22
$100 \cdot k_{\mathrm{cat}}$	23846	160	991	35901	271

Table 6.1: Comparison of the Michaelis-Menten constant K_{m} obtained from the fitting of the oligomerization simulation and the one calculated by the pseudo-mono-molecular reaction. δK_{m} denotes the standard error of the fit.

connected by a coiled coil, also show a turnover rate of about $4\,\mathrm{ATP\,s^{-1}}$ (Eckert et al., 2012b). These results suggest that dimerization is an important step in the oligomerization process as said process is sped up considerably as soon as dimers are available. Furthermore it shows that the dimerization process works faster in the presence of microtubules.

This theory however could not be certified in simulation as the turnover rate is not increased significantly by raising the dimerization rate by a factor of 100. This leads to the conclusion that not only the dimerization rate but all oligomerization rates are favored by the presence of and interaction with microtubules. Increasing the other forward rates by a factor of 100 changed the distribution of the species of intermediates accordingly to the rates. The resulting distribution of intermediates was as expected, given the theory and model of the assembly pathways and their respective rates. However, K_{m} was changed by the increase of each forward rate, as shown in table (3.2).

Non-linear reactions

For a rough estimation of the value of K_{m}, all reactions were assumed to be pseudo-mono-molecular. The half-maximal turnover rate assuming pseudo-mono-molecular reactions, $K_{\mathrm{m,pmm}}$, is then given by equation (2.43), which is independent of the assembly pathway. The values of K_{m} are summarized in table (6.1). When comparing the fit parameter of the simulations using the default parameter set to the estimated value of the half-maximal turnover, $K_{\mathrm{m,1236}}$ is in very good agreement with $K_{\mathrm{m,pmm}}$, whereas $K_{\mathrm{m,1246}}$ is considerably higher. When increasing the forward rates by a factor 100 and comparing the resulting values of K_{m} the differences depend on which rate is altered: in the 1-2-3-6 assembly pathway a change in the trimerization rate k_{23} results in $K_{\mathrm{m,1236,100\cdot k_{23}}}$, which is close to

the pseudo-mono-molecular estimation of $K_{m,pmm,100 \cdot k_{23}}$. In the 1-2-4-6 assembly pathway only a change in the hexamerization rate k_{46} returns a value of $K_{m,1246,100 \cdot k_{46}}$ which is close to the estimated $K_{m,pmm,100 \cdot k_{46}}$. In both pathways a change in the dimerization rate results in a completely different value of $K_{m,1236,100 \cdot k_{12}}$, and $K_{m,1246,100 \cdot k_{12}}$ respectively compared to the the pseudo-mono-molecular reaction of $K_{m,pmm,100 \cdot k_{12}}$. Furthermore, the hexamerization rate of the 1-2-3-6 assembly pathway k_{36} and the tetramerization rate of the 1-2-4-6 pathway k_{24} lead to values of K_m which differ significantly from the value obtained from the pseudo-mono-molecular estimation ($K_{m,1236,100 \cdot k_{36}}$ and $K_{m,1246,100 \cdot k_{24}}$).

A schematic deviation between the fit values and the pseudo-mono-molecular estimation can be seen: if the reaction is linear (e.g. trimerization), the fitted and calculated values for K_m are in good accordance. However, if the reaction is non-linear (e.g. dimerization), a clear discrepancy between the fitted and the estimated value of K_m is found. This shows that the assumed simplification does not hold in the case of non-linear processes, and that the process of hexamerization is a highly complex and non-linear process. Furthermore, it explains the high value of $K_{m,1246}$: like the 1-2-3-6 assembly pathway, the 1-2-4-6 assembly pathway consists of two non-linear oligomerization processes but also needs the products of two *distinct* non-linear reactions (dimers and tetramers) to form a hexamer. Hence this pathway of hexamer formation needs more monomers to reach the same turnover rate as the 1-2-3-6 assembly pathway (K_m). In addition, this consideration explains the difference between the fitted and estimated K_m, as the pseudo-mono-molecular approximation neglects all non-linear reactions. This also shows why a detailed consideration of the assembly process, as done in this work, is necessary.

Proposed further experiments

Even though other assembly pathways are possible, the two presented here require the least amount of intermediate species. Hence the pools of the intermediates can be filled up faster than for example those of the hexamer formation pathway using a sequential addition of monomers. The goal of wild type simulations is to elucidate the assembly pathway of spastin. As the distribution of intermediates of spastin is unknown, one possibility to compare simulated and experimental data is analyzing of the catalytic turnover rate as a function of wild type monomers. As can be seen in figure (3.7) both assembly pathways reproduce the measurement very well. From these data no clear conclusions can be drawn. The coupled enzymatic ATPase assay cannot be exploit to a larger extend as more measurements at lower enzyme concentrations are needed. However, measurements at such low

concentrations display a poor signal-to-noise ratio, and hence are not optimal to answer the question of hexamerization.

It may be possible to answer this question using FCS: even though the data presented here indicate the present of intermediates, the distinction between the different species of intermediates is very difficult due to the small differences between the diffusion coefficients. Recently the intent of elucidating of the oligomerization process using FCS has raised more interest and first attempts to improve the FCS procedure in this regard have been made (Chakraborty et al., 2012).

A further possibility to reconnoiter intermediates present in hexamer formation is fluorescence cross-correlation spectroscopy (FCCS), which is a FCS set-up using two different fluorophores. Hence the enzyme can be labeled using two different fluorescent dyes. The cross-correlation of the autocorrelation functions of these two dyes would indicate an oligomer, which is at least a dimer.

Using the data acquired by FCS and FCCS a further analysis called PCH (photo counting histogram) can be applied, which does not use the diffusion coefficient but the fluorescence intensity to obtain information of the diffusing particles. With this technique species of similar diffusion times can be differentiated due to their different molecular brightness.

6.3 Studies on inhibitory effects

AAA-ATPase proteins can display a complex form of cooperativity as shown by Hattendorf and Lindquist (2002), Martin et al. (2005), Horwitz et al. (2007), Werbeck et al. (2009), Nishikori et al. (2011). In addition many allelic forms of human AAA ATPases exposing dominant negative pathogenic effects are known. These behaviors demonstrate the importance of the interaction between subunits incorporated within an oligomer, and the effect of defective (mutant) subunits on intact (wild type) subunits within mixed oligomers. The results presented in this thesis are the first systematic studies on the effects of mutant, inactive subunits on the turnover activity of wild type enzymes. Furthermore, by using kinetic Monte Carlo simulations different cooperative models, inhibition schemes, and their results were studied.

Typically cooperative effects can be seen in graphs displaying the catalytic rate against the substrate concentration. A sigmoidal shape of the function implies a positive cooperative interaction of subunits. However, all classical models used to explain cooperativity, e.g. the Monod-Wyman-Changeux model, assume an already formed and stable oligomer,

which has multiple binding sites for substrates, as in the case of hemoglobin or lacI protein (Monod et al., 1963, 1965).

A further, less conventional way of detecting cooperativity is to perform measurements of turnover rates of mixed oligomeric enzymes, i.e. oligomers incorporating mutant and wild type subunits. The effect of cooperativity can then be seen in plots of the catalytic turnover rate per wild type subunit versus the concentration of catalytically inactive mutants. If wild type subunits do not have any influence on each other and their catalytic behavior respectively (i.e. non-cooperative behavior), the addition of defective mutant subunits (to a constant concentration of wild type) is very likely to have no effect on the catalytic activity and the turnover rate would stay constant with increasing mutant concentration. Cooperative behavior, however, would result in a turnover rate which depends on the concentration of added mutants, while the concentration of wild type is kept constant. It has been shown that increasing the mutant concentration can lead to a decrease of the steady state catalytic turnover rate (Werbeck et al., 2008, Eckert et al., 2012a). Other scenarios, however, are also possible, as shown by Hoskins et al. (2009) where the maximal turnover rate is achieved at a ratio of wild type and mutant of 50:50.

Different attempts and models explaining cooperativity have been developed over the past decades, but they are all based on the binding of substrates and assume a ready and stable oligomer. Cooperativity based on the incorporation of mutant subunits and hence their possible inhibitory effect have not been elaborated yet. Published studies such as Martin et al. (2005), Werbeck et al. (2008) use coarse simplifications. An accurate formulation of the cooperative experiments using mutant subunits is difficult, mainly because of the two following reasons: firstly the unknown concentration of enzyme, both mutant and wild type, at equilibrium, and secondly the cooperative, and possible inhibitory, effect. As the oligomerization process includes non-linear reactions (e.g. dimerization of the same species), the determination of the concentration of free enzyme in equilibrium, given the initial free enzyme concentration, is not trivial as a set of coupled, non-linear equations needs to be solved. To calculate the distribution of mixed hexamers, the steady state concentration is frequently assumed to be the initial concentration (Werbeck et al., 2008, Hoskins et al., 2009, Franzmann et al., 2011, Stotz et al., 2011, Eckert et al., 2012a). With this simplification the probability of encountering an oligomer incorporating k mutant subunits is computed, using a binomial distribution function, which is given by equation (2.34). In addition the cooperative effect needs to be formulated explicitly. As in the case of spastin the addition of mutants results in a reduction and hence inhibition of the catalytic turnover

rate. Therefore an inhibition scheme has to be developed for the simulation. This has been performed in the course of this work.

Nearest-neighbor inhibition scheme

The first, and also easiest, attempt to describe the inhibitory effect of mutant spastin is based on the cooperative behavior of subunits is to take into account only the interaction between exactly two subunits within a hexamer. This ansatz is termed the nearest neighbor inhibition scheme. The principle is the following: one mutant subunit can only inhibit a wild type subunit if both are properly orientated relative to each other as indicated in figure (4.1). This assumption is a crude simplification as all other subunits of the hexamer are neglected: dimers are regarded as catalytically active, and incorporation into stable hexamers is assumed. Nevertheless, the nearest neighbor inhibition scheme fits the experimental data on the inhibitory effect of mutants very well, as can be seen in figure (4.2). From comparison to other AAA ATPases such as CLPX or Rubisco activase it can be deduced that spastin needs to form oligomers. It has been shown that the catalytically inactive spastin mutant E442Q can form hexameric structures (White et al., 2007, Roll-Mecak and Vale, 2008, Eckert, 2012). However, wild type spastin has so far not been observed in hexameric form.

The fact that the nearest-neighbor inhibition scheme is in good agreement with the experimental data leads to the following two possible explanations: firstly, a mixture of wild type and mutant subunits either leads to the formation of dimers only. Secondly and more likely, mutant and wild type subunits incorporate into a hexamer. If the assumption of dimers as catalytic form is true, the nearest-neighbor inhibition scheme gives an accurate explanation and also prediction of the inhibitory effect of mutant subunits on wild type subunits, as indicated by the fitting function. However, it is generally believed that spastin assembles into hexamers, as shown by the E442Q mutant. The simplified case that only two subunits are sufficient to dictate the activity of the whole hexamer is unlikely, because the formation of a hexamer needs more time than the formation of a dimer and is also more complex. In this case the fact that the nearest-neighbor inhibition scheme fits the data so well must be attributed to an insufficient knowledge of the fit parameters. Therefore a more complex scheme for the inhibitory effect of mutant on wild type subunits was formulated.

Simulation of inhibition

The different properties of mutant and wild type subunits are realized in the Gillespie algorithm using the following three steps: the incorporation into a hexamer, the cooperative effect on other subunits, and the catalytic turnover rate. An initial number of mutant and wild type monomers can assemble into hexamers as described above and in more detail in chapter (3.2). Mutants and wild type are allowed to have different forward and reverse rates, but due to structural considerations, the rates were set to be identical if the same binding partners take part at the oligomerization step (e.g. the trimerization rates: MM + WM = WM + WW but may differ from the dimerization rate M + W, see chapter 4). A hexamer can be degraded through two different pathways: disassembly with the reverse rate k_{6i}, where i depends on the assembly pathway, or hydrolysis with the rate k_{cat} and disassembly into six monomers. In order to consider the latter step three different inhibition schemes were introduced, which describe the cooperative effects of mutant and wild type subunits:

- inhibition scheme 1 assumes that one mutant subunit is sufficient to inhibit the turnover rate of all wild type subunits incorporated in the same hexamer,

- in inhibition scheme 2 one mutant subunit inhibits both of its direct neighbors, and

- in inhibition scheme 3 one mutant inhibits one wild type subunit (which, without loss of generality, is assumed to be the neighbor to the right, which is an extension of the nearest neighbor inhibition scheme).

Using these inhibition schemes the number of mutant, inhibited, and fully active wild type subunits can be determined, as listed in table (4.1). Each of these three species is assigned a turnover rate: the mutant is inactive and hence $k_{cat,m} = 0$. In case of wild type the fully active turnover rate $k_{cat,ww}$ is in general larger than the inhibited turnover rate of wild type $k_{cat,wm}$. With these requirements it could be shown that inhibition scheme 1 has the strongest effect on the resulting turnover rate, and inhibition scheme 3 the weakest. Also the strong variation of the forward and backward rates of oligomers incorporating mutants did not change the relative inhibitory effect of these three schemes. The strength of inhibition, which is indicated by the amount of mutant subunits necessary to achieve half-maximal inhibition, K_i, is affected by these variations. This is shown in figure (4.6). These observations are valid for both assembly pathways, where the 1-2-3-6 assembly pathway has a higher initial k_{obs} than the 1-2-4-6 pathway, as discussed above.

Simulation and experiment

To reconnoiter the inhibition pattern of spastin mutants on wild type enzyme the simulated and experimental data were compared by converting the concentration of the enzyme in experiments into the number of particles used in the simulations. In this instance the simulations using 5000 wild type particles and the default parameter set of reaction rates given in table (3.1) were used. It could be shown that simulated data using inhibition scheme 2 bear the strongest resemblance to the experimental data. However, the experimental data depend on the determination of the concentration of both wild type and mutant enzyme, where a deviation in the measurement of 20% for both species leads to a variation of the scaling factor of 0.67 to 1.5. But even within this large scaling range, inhibition scheme 1 and inhibition scheme 3 could not reproduce the experimental data. To this end a scaling factor of 0.25 and 4.0 were needed respectively. This means that in the case of spastin, inhibition scheme 1 has a too dominant effect on the turnover rate, whereas inhibition scheme 3 does not inhibit the turnover rate of wild type as strongly as is observed in experiments.

These considerations in turn show that one mutant subunit with a single point mutation does inhibit both of its direct neighbors, whereas all further wild type subunits remain unaffected. This suggests that either the subunit has to undergo a large conformational change in order to cooperate with other subunits, or that the effect of binding translates over a large region of the subunit. Models involving allosteric coupling in both directions of a mutant subunit have been put forth for the PAN ATPase by Smith et al. (2011). The inhibition scheme 2 could be modulated in such a way that not only the neighbors in the vicinity but also subunits further away are influenced from the mutant. Although for each hexamer species, i.e. different ratios and different relative configurations of wild type to mutant subunits as shown in figure (4.4), the inhibition of the whole hexamer would change, the overall turnover rate would not differ significantly from the values obtained from the inhibition scheme 2 used in this work. This is due to the calibration of the inhibition on incorporated wild type subunits and the different hexamer configurations. Furthermore, the nearest neighbor inhibition scheme presented in chapter (4.1) does not hold when hexamers are assumed to be the catalytically active form. It was further found that a conversion of the classical inhibition of substrate binding model of Monod, Wyman and Changeux (MWC-model) into inhibition scheme 1 fails to describe the experimental data. Hence a hexamer cannot be described by using a tensed and relaxed state as used in the MWC-model.

Fit functions

The cooperative behavior and allosteric dependencies of enzymes are complicated to formulate and need to be simulated. Assuming a one-to-one relation between fit function and inhibition scheme, the true inhibition scheme can be identified by fitting the experimental data. In this scenario the other fit functions corresponding to the wrong inhibition schemes would show systematic deviations from the data. In the literature the traditional fit function for the inhibitory effect of mutant on wild type enzyme bases on a binomial distribution as described by Werbeck et al. (2008), Hoskins et al. (2009), Stotz et al. (2011), Franzmann et al. (2011). However, a systematic deviance between data and fit is visible. Therefore an extended and improved fit formula based on a binomial distribution was developed in the course of this work, which includes both the different activity levels of incorporated subunits in the hexamer (mutant, inhibited and fully active wild type) and the possibility of different incorporation rates of wild types and mutants into a hexamer (factor d of equation 4.15). Another approach in the course of this was the development of a non-competitive inhibition model. It is an extension of textbook knowledge presented in Fersht (1985), where the different turnover rates were taken into account. This fitting model considers the binding of inhibitors as a pseudo-first-order reaction, which is however not legitimate for the oligomerization steps of the same species as they are second order reactions (Gutfreund, 1995).

The extended binomial fit function matches the trend of the simulated data qualitatively very well as shown in figures (4.8(a)) and (4.9(a)), but fails quantitatively as the fit parameter $k_{\mathrm{cat,ww}}$ is considerably smaller than the inserted $k_{\mathrm{cat,ww}} = 5.0\,\mathrm{s}^{-1}$ in the simulation (see table 4.3). When keeping this fit parameter fix at $5.0\,\mathrm{s}^{-1}$ (see table 4.5) the data can not be fitted qualitatively anymore. Even the fit of data of inhibition scheme 1 displays a systematic deviation, as can be seen in figures (4.10(a)) and (4.10(b)). Hence, no relation between the binomial fit and any inhibition scheme can be drawn.

Despite the simplification of pseudo-first-order reactions, the extended non-competitive fitting model represents the simulated data of most simulations reasonably well, both qualitatively as shown in figures (4.8(b)) and (4.9(b)) and quantitatively (see table 4.4). These simulations were performed using different parameter sets of forward and reverse rates. The fit parameter $k_{\mathrm{cat,ww}}$ returns a value close to the inserted $k_{\mathrm{cat,ww}} = 5.0\,\mathrm{s}^{-1}$, and the fit parameter $k_{\mathrm{cat,wm}}$ was usually within a factor of two of the value inserted into the simulation, except for extreme conditions for incorporation and turnover rates of mutant constructs (fast reverse rates of mutant-x oligomers with x either mutant or wild type, and

$k_{\text{cat,ww}} = 0.005\,\text{s}^{-1}$ respectively). As the standard deviations of the fit parameters were quite large, the fit parameter $k_{\text{cat,ww}}$ was held fix at $k_{\text{cat,ww}} = 5.0\,\text{s}^{-1}$. The resulting fit parameter $k_{\text{cat,wm}}$ still returned values within a factor of two with the same exceptions, but the standard deviation was reduced significantly (see table 4.6).

The fitted values of the half-maximal activation constant K_{m} with its uncertainty region encompasses the value of K_{m} obtained from simulations using wild type subunits only. However, the non-competitive fit function matches data obtained from all three inhibition schemes.

Naively the best agreement between fit function and inhibition scheme would be expected for a correlation between inhibition scheme 1 and the binomial fit, and between inhibition scheme 3 and the non-competitive fitting model, as they are based on similar assumptions. This could not be concluded from the simulations and their respective fits as the analysis was not clearly distinguishable. As no one to one correlation between fit function and inhibition scheme could be derived, kinetic simulations need to be performed in future work in order to elucidate which inhibition scheme the cooperativity of wild type and mutant subunits obeys.

6.4 Conclusion on simulations

In conclusion, the work presented here shows that using wild type only simulations the assembly models assuming a avalanche-like hexamerization process, that is the 1-2-3-6 and 1-2-4-6 assembly pathway, describe the observed dependence of activity of spastin on its concentration. In addition in this work the first systematical description of the possible inhibition patterns of mutant subunits on wild type subunits of AAA ATPases were developed. Herein the focus was directed at the microtubule severing enzyme spastin. Furthermore, these predictions of negative cooperativity were tested using simulations based on the Gillespie algorithm. In addition, two textbook fit functions were refined to match the inhibition data, both simulated and experimental. Experimental data could only be fitted with satisfying accuracy using the non-competitive inhibition model, whereas no clear one to one correlation between inhibition scheme and fitting model could be found. This indicates the difficulty of predicting the inhibitory pattern of an enzyme on a molecular level. Furthermore, statements on concerted, probabilistic, and sequential mechanisms of AAA ATPases as introduced by Martin et al. (2005) are uncertain as they are only based on the fit function, showing systematic deviations from the data. Even though no overall

formula, as e.g. the Hill equation or the non-competitive formula by Fersht, could be derived to elucidate the inhibitory mechanism, a groundwork for further systematic studies on cooperativity was set in the course of this work.

Further investigations are necessary to reconnoiter the enzyme spastin in more detail. As the simulations depend strongly on rates, the experimental determination of forward, reverse, and also turnover rates is essential. One possibility to derive the forward and reverse rates would be given by stop flow measurements, which however require a large amount of the enzyme. Also knowledge of the exact molecular interaction between mutant and wild type spastin during hydrolysis would be beneficial in order to corroborate if a sequential or a synchronous hydrolysis process occurs (e.g. a time delay between hydrolysis and conformational change). This is because the simulations in this work assume simultaneous hydrolysis of six ATP molecules. As the simulations further assumes ATP to be at saturating concentrations, a beneficial addition to the simulation would be to include the dependency of the rates on the ATP concentration. In this case all forward, backward, and turnover rates depend on the ATP concentration, and one would have to determine these values in experiments before such simulations could be carried out. However, the benefit of such an effort would be a more detailed description of the enzyme. Furthermore, it is known that the catalytic activity of spastin in enhanced by the presence of microtubules, yet the exact effect of microtubules on spastin is still unknown. Hence all rates need to be determined in presence and absence of microtubules.

Appendix A

List of publications

P1 Le Doan Tuong-Van, Eckert Thomas, Woehlke Günther. Computer Simulation of Assembly and Co-operativity of Hexameric AAA ATPases. Accepted by PlosOne.

P2 Eckert Thomas, Le Doan Tuong-Van, Link Susanne, Friedmann Lena, Woehlke Günther. Spastin's Microtubule-Binding Properties and Comparison to Katanin. PLOS ONE, 7, 12:e50161, 2012.

P3 Eckert Thomas, Link Susanne and Le Doan Tuong-Van, Sobczak Jean Phillipe, Gieseke Anja, Richter Klaus, Woehlke Günther. Subunit Interactions and cooperativity in the microtubule-severing AAA ATPase spastin. The Journal of Biological Chemistry, 287, 31:26278–26290, 2012.

Appendix B

Sequences

B.1   Human Spastin delta227

Spastin with BamHI restriction site at the beginning and NotI at the end of the sequence:

GSKKCKMSGAVPKRKDPLTHTSNSLPRSKTVMKTGSAGLSGHHRAPSYSGLSMV
SGVKQGSGPAPTTHKGTPKTNRTNKPSTPTTATRKKKDLKNFRNVDSNLANLIM
NEIVDNGTAVKFDDIAGQDLAKQALQEIVILPSLRPELFTGLRAPARGLLLFGP
PGNGKTMLAKAVAAESNATFFNISAASLTSKYVGEGEKLVRALFAVARELQPSI
IFIDEVDSLLCERREGEHDASRRLKTEFLIEFDGVQSAGDDRVLVMGATNRPQE
LDEAVLRRFIKRVYVSLPNEETRLLLLKNLLCKQGSPLTQKELAQLARMTDGYS
GSDLTALAKDAALGPIRELKPEQVKNMSASEMRNIRLSDFTESLKKIKRSVSPQ
TLEAYIRWNKDFGDTTV-AA

B.2   Chimeric kinesin, human tail, cys light

MSAEREIPAEDSIKVVCRFRPLNDSEEKAGSKFVVKFPNNVEENSISIAGKVYL
FDKVFKPNASQEKVYNEAAKSIVTDVLAGYNGTIFAYGQTSSGKTHTMEGVIGD
SVKQGIIPRIVNDIFNHIYAMEVNLEFHIKVSYYEIYMDKIRDLLDVSKVNLSV
HEDKNRVPYVKGATERFVSSPEDVFEVIEEGKSNRHIAVTNMNEHSSRSHSVFL
INVKQENLENQKKLSGKLYLVDLAGSEKVSKTGAEGTVLDEAKNINKSLSALGN
VISALADGNKTHIPYRDSKLTRILQESLGGNARTTIVICCSPASFNESETKSTL
DFGRRAKTVKNVVSVNEELTAEEWKRRYEKEKEKNARLKGKVEKLEIELARWRA
GETVKAEEQINMEDLALGAFTVDKDITLTNDKPATAIGVIGNFTDAERRKCEEE
IAKLYKQLDDKDEEINQQSQLVEKLKTQMLDQEELLASTRRDQDNMQAELNRLQ

AENDASKEEVKEVLQALEELAVNYDQKSQEVEDKTKEYELLSDELNQKSATLAS
IDAELQKLKEMHANSSSVDKLAAALEHHHHHH

Bibliography

E. A. Abbondanzieri and X. Zhuang. Molecular biology: Concealed enzyme coordination. *Nature*, 457(7228):392–393, 2009.

G. S. Adair, A. V. Bock, and H. Field Jr. The hemoglobin system. *Journal of biological chemistry*, 63(2):529–545, 1925.

S. Adio, M. Bloemink, M. Hartel, S. Leier, M. A. Geeves, and G. Woehlke. Kinetic and mechanistic basis of the nonprocessive kinesin-3 motor nckin3. *Journal of Biological Chemistry*, 281(49):37782–37793, 2006.

I. Azmi, B. Davies, C. Dimaano, J. Payne, D. Eckert, M. Babst, and D. J. Katzmann. Recycling of ESCRTs by the AAA-ATPase Vps4 is regulated by a conserved VSL region in Vta1. *Journal of Cell Biology*, 172(5):705–717, 2006.

C. Beetz, M. Brodhun, K. Moutzouris, M. Kiehntopf, A. Berndt, D. Lehnert, T. Deufel, M. Bastmeyer, and J. Schickel. Identification of nuclear localisation sequences in spastin (SPG4) using a novel Tetra-GFP reporter system. *Biochemical and Biophysical Research Communications*, 318(4):1079–1084, 2004.

J. M. Berg, L. Stryer, and J. L. Tymoczko. *Biochemie.* Elsevier, Spektrum, Akad. Verl., Heidelberg [u.a.], 6 edition, 2007.

G. Binnig, C. F. Quate, and C. Gerber. Atomic force microscope. *Physical Review Letters*, 56(9):930–933, 1986.

C. Blackstone, C. J. O'Kane, and E. Reid. Hereditary spastic paraplegias: membrane traffic and the motor pathway. *Nature Reviews Neuroscience*, 12(1):31–42, 2011.

M. A. Blair, M. E. Riddle, J. F. Wells, B. A. Breviu, and P. Hedera. Infantile Onset of Hereditary Spastic Paraplegia Poorly Predicts the Genotype. *Pediatric Neurology*, 36 (6):382–386, 2007.

M. R. Block, B. S. Glick, C. A. Wilcox, F. T. Wieland, and J. E. Rothman. Purification of an N-ethylmaleimide-sensitive protein catalyzing vesicular transport. *Proceedings of the National Academy of Sciences U.S.A.*, 85(21):7852–7856, 1988.

B. Bösl, V. Grimminger, and S. Walter. The molecular chaperone Hsp104–a molecular machine for protein disaggregation. *Journal of Structural Biology*, 156(1):139–148, 2006.

M. Chakraborty, A. M. Kuriata, J. Nathan Henderson, M. E. Salvucci, R. M. Wachter, and M. Levitus. Protein oligomerization monitored by fluorescence fluctuation spectroscopy: self-assembly of rubisco activase. *Biophysical Journal*, 103(5):949–958, 2012.

F. D. Ciccarelli, C. Proukakis, H. Patel, H. Cross, S. Azam, M. A. Patton, P. Bork, and A. H. Crosby. The identification of a conserved domain in both spartin and spastin, mutated in hereditary spastic paraplegia. *Genomics*, 81(4):437–441, 2003.

P. Claudiani, E. Riano, A. Errico, G. Andolfi, and E. I. Rugarli. Spastin subcellular localization is regulated through usage of different translation start sites and active export from the nucleus. *Experimental Cell Research*, 309(2):358–369, 2005.

C. Conde and A. Caceres. Microtubule assembly, organization and dynamics in axons and dendrites. *Nature Reviews Neuroscience*, 10(5):319–332, 2009.

I. Corthesy-Theulaz, A. Pauloin, and S. R. Rfeffer. Cytoplasmic dynein participates in the centrosomal localization of the Golgi complex. *Journal of Cell Biology*, 118(6): 1333–1345, 1992.

C. Crimella, C. Baschirotto, A. Arnoldi, A. Tonelli, E. Tenderini, G. Airoldi, A. Martinuzzi, A. Trabacca, L. Losito, M. Scarlato, S. Benedetti, E. Scarpini, G. Spinicci, N. Bresolin, and M. T. Bassi. Mutations in the motor and stalk domains of KIF5A in spastic paraplegia type 10 and in axonal Charcot–Marie–Tooth type 2. *Clinical Genetics*, 2011.

A. H. Crosby and C. Proukakis. Is the transportation highway the right road for hereditary spastic paraplegia? *The American Journal of Human Genetics*, 71(5):1009–1016, 2002.

L. Dehmelt and S. Halpain. The map2/tau family of microtubule-associated proteins. *Genome Biology*, 6(1):204, 2004.

B. DeLaBarre, J. C. Christianson, R. R. Kopito, and A. T. Brunger. Central Pore Residues Mediate the p97/VCP Activity Required for 5ERAD6. *Molecular Cell*, 22(4):451–462, 2006.

A. Desai and T. J. Mitchison. Microtubule polymerization dynamics. *Annual Review of Cell and Developmental Biology*, 13:83–117, 1997.

R. Dixit, J. L. Ross, Y. E. Goldman, and E. L. F. Holzbaur. Differential Regulation of Dynein and Kinesin Motor Proteins by Tau. *Science*, 319(5866):1086–1089, 2008.

M. R. D'Orsogna, G. Lakatos, and T. Chou. Stochastic self-assembly of incommensurate clusters. *Journal of Chemical Physics*, 136(8):084110, 2012.

U. R. E. M. Mandelkow, M. Herrmann. Tubulin domains probed by limited proteolysis and subunit specific antibodies., 1985.

B. Ebbing, K. Mann, A. Starosta, J. Jaud, L. Schöls, R. Schüle, and G. Woehlke. Effect of spastic paraplegia mutations in kif5a kinesin on transport activity. *Human Molecular Genetics*, 17(9):1245–1252, 2008.

T. Eckert, S. Link, D. T. V. Le, J. P. Sobczak, A. Gieseke, K. Richter, and G. Woehlke. Subunit interactions and cooperativity in the microtubule-severing aaa atpase spastin. *Journal of Biological Chemistry*, 287(31):26278–26290, 2012a.

T. Eckert. *Kinetische und strukturelle Untersuchung der beiden Mikrotubuli-schneidenden Enzyme Spastin und Katanin.* PhD thesis, Technische Universität München, 2012.

T. Eckert, D. T.-V. Le, S. Link, L. Friedmann, and G. Woehlke. Spastin's microtubule-binding properties and comparison to katanin. *PLoS ONE*, 7(12):e50161, 2012b.

E. L. Elson and D. Magde. Fluorescence correlation spectroscopy. i. conceptual basis and theory. *Biopolymers*, 13:1 – 27, 1974.

R. Erdmann, F. F. Wiebel, A. Flessau, J. Rytka, A. Beyer, K.-U. Fröhlich, and W.-H. Kunau. PAS1, a yeast gene required for peroxisome biogenesis, encodes a member of a novel family of putative ATPases. *Cell*, 64(3):499–510, 1991.

H. P. Erickson and E. T. O'Brien. Microtubule Dynamic Instability and GTP Hydrolysis. *Annual Review of Biophysics and Biomolecular Structure*, 21(1):145–166, 1992.

A. Errico, P. Claudiani, M. D'Addio, and E. I. Rugarli. Spastin interacts with the centrosomal protein NA14, and is enriched in the spindle pole, the midbody and the distal axon. *Human Molecular Genetics*, 13(18):2121–2132, 2004.

K. Evans, C. Keller, K. Pavur, K. Glasgow, B. Conn, and B. Lauring. Interaction of two hereditary spastic paraplegia gene products, spastin and atlastin, suggests a common pathway for axonal maintenance. *Proceedings of the National Academy of Sciences of the United States of America*, 103(28):10666–10671, 2006.

K. J. Evans, E. R. Gomes, S. M. Reisenweber, G. G. Gundersen, and B. P. Lauring. Linking axonal degeneration to microtubule remodeling by Spastin-mediated microtubule severing. *Journal of Cell Biology*, 168(4):599–606, 2005.

A. R. Fersht. Fidelity of DNA replication in vitro. *Advances in Experimental Medicine and Biology*, 179:525–533, 1984.

A. Fersht. *Enzyme structure and mechanism.* W.H. Freeman, New York, 2 edition, 1985.

J. K. Fink, T. Heiman-Patterson, T. Bird, F. Cambi, M. P. Dube, D. A. Figlewicz, J. K. Fink, J. L. Haines, T. Heiman-Patterson, A. Hentati, M. A. Pericak-Vance, W. Raskind, G. A. Rouleau, and T. Siddique. Hereditary spastic paraplegia: advances in genetic research. Hereditary Spastic Paraplegia Working group. *Neurology*, 46(6):1507–1514, 1996.

K. N. Fish. *Total Internal Reflection Fluorescence (TIRF) Microscopy.* John Wiley & Sons, Inc., 2001.

E. L. Florin, V. T. Moy, and H. E. Gaub. Adhesion forces between individual ligand-receptor pairs. *Science*, 264(5157):415–417, 1994.

N. Fonknechten, D. Mavel, P. Byrne, C. S. Davoine, C. Cruaud, D. Bonsch, D. Samson, P. Coutinho, M. Hutchinson, P. McMonagle, J. M. Burgunder, A. Tartaglione, O. Heinzlef, I. Feki, T. Deufel, N. Parfrey, A. Brice, B. Fontaine, J. F. Prud'homme, J. Weissenbach, A. Durr, and J. Hazan. Spectrum of SPG4 mutations in autosomal dominant spastic paraplegia. *Human molecular genetics*, 9(4):637–644, 2000.

W. Fontana. Gillespie's method, briefly., 2007.

T. M. Franzmann, A. Czekalla, and S. G. Walter. Regulatory Circuits of the AAA+ Disaggregase Hsp104. *Journal of biological chemistry*, 286(20):17992–18001, 2011.

D. T. Gillespie. A general method for numerically simulating the stochastic time evolution of coupled chemical reactions. *Journal of Computational Physics*, 22(4):403 – 434, 1976.

D. T. Gillespie. Exact stochastic simulation of coupled chemical reactions. *Journal of Physical Chemistry*, 81(25):2340–2361, 1977.

P. Goloubinoff, A. Mogk, A. P. Zvi, T. Tomoyasu, and B. Bukau. Sequential mechanism of solubilization and refolding of stable protein aggregates by a bichaperone network. *Proceedings of the National Academy of Sciences U.S.A.*, 96(24):13732–13737, 1999.

H. Gutfreund. *Kinetics for the Life Sciences.* Cambridge University Press, Cambridge, 1st ed. edition, 1995.

P. I. Hanson and S. W. Whiteheart. AAA+ proteins: have engine, will work. *Nature Reviews Molecular Cell Biology*, 6(7):519–529, 2005.

J. J. Hartman and R. D. Vale. Microtubule disassembly by ATP-dependent oligomerization of the AAA enzyme katanin. *Science*, 286(5440):782–785, 1999.

J. J. Hartman, J. Mahr, K. McNally, K. Okawa, A. Iwamatsu, S. Thomas, S. Cheesman, J. Heuser, R. D. Vale, and F. J. McNally. Katanin, a microtubule-severing protein, is a novel AAA ATPase that targets to the centrosome using a WD40-containing subunit. *Cell*, 93(2):277–287, 1998.

D. A. Hattendorf and S. L. Lindquist. Cooperative kinetics of both Hsp104 ATPase domains and interdomain communication revealed by AAA sensor-1 mutants. *The EMBO journal*, 21(1-2):12–21, 2002.

J. Hazan, N. Fonknechten, D. Mavel, C. Paternotte, D. Samson, F. Artiguenave, C.-S. Davoine, C. Cruaud, A. Durr, P. Wincker, P. Brottier, L. Cattolico, V. Barbe, J.-M. Burgunder, J.-F. Prud'homme, A. Brice, B. Fontaine, R. Heilig, and J. Weissenbach. Spastin, a new AAA protein, is altered in the most frequent form of autosomal dominant spastic paraplegia. *Nature Genetics*, 23(3):296–303, 1999.

G. L. Hersch, R. E. Burton, D. N. Bolon, T. A. Baker, and R. T. Sauer. Asymmetric Interactions of ATP with the AAA+ ClpX6 Unfoldase: Allosteric Control of a Protein Machine. *Cell*, 121(7):1017–1027, 2005.

T. L. Hill. Effect of Nearest Neighbor Substrate Interactions on the Rate of Enzyme and Catalytic Reactions. *Journal of the American Chemical Society*, 74(18):4710–4711, 1952.

S. Hodson, J. J. T. Marshall, and S. G. Burston. Mapping the road to recovery: The ClpB/Hsp104 molecular chaperone. *Journal Of Structural Biology*, 179(2):161–171, 2012.

A. A. Horwitz, A. Navon, M. Groll, D. M. Smith, C. Reis, and A. L. Goldberg. ATP-induced structural transitions in PAN, the proteasome-regulatory ATPase complex in Archaea. *Journal of biological chemistry*, 282(31):22921–22929, 2007.

J. R. Hoskins, M. Pak, M. R. Maurizi, and S. Wickner. The role of the ClpA chaperone in proteolysis by ClpAP. *Proceedings of the National Academy of Sciences U.S.A.*, 95(21): 12135–12140, 1998.

J. R. Hoskins, S. M. Doyle, and S. Wickner. Coupling ATP utilization to protein remodeling by ClpB, a hexameric AAA+ protein. *Proceedings of the National Academy of Sciences of the United States of America*, 106(52):22233–22238, December 2009.

T. G. Huang and D. D. Hackney. Drosophila kinesin minimal motor domain expressed in escherichia coli. purification and kinetic characterization. *Journal of Biological Chemistry*, 269(23):16493–16501, 1994.

A. A. Hyman. Preparation of marked microtubules for the assay of the polarity of microtubule-based motors by fluorescence. *Journal of Cell Science*, 14:125–127, 1991.

L. M. Iyer, D. D. Leipe, E. V. Koonin, and L. Aravind. Evolutionary history and higher order classification of AAA+ 5ATPases6. *Journal of Structural Biology*, 146(1–2):11–31, 2004.

R. Jahn, T. Lang, and T. C Südhof. Membrane Fusion. *Cell*, 112(4):519–533, 2003.

W. Jiang, M. F. Stock, X. Li, and D. D. Hackney. Influence of the kinesin neck domain on dimerization and ATPase kinetics. *Journal of biological chemistry*, 272(12):7626–7632, 1997.

S. A. Joshi, G. L. Hersch, T. A. Baker, and R. T. Sauer. Communication between ClpX and ClpP during substrate processing and degradation. *Nature Structural & Molecular Biology*, 11(5):404–411, 2004.

K. N. Karle, D. Möckel, E. Reid, and L. Schöls. Axonal transport deficit in a KIF5A (-/-) mouse model. *Neurogenetics*, 13(2):169–179, 2012.

S. Kienle, S. Liese, N. Schwierz, R. R. Netz, and T. Hugel. The effect of temperature on single-polypeptide adsorption. *ChemPhysChem*, 13(4):982–989, 2012.

Y. I. Kim, R. E. Burton, B. M. Burton, R. T. Sauer, and T. A. Baker. Dynamics of substrate denaturation and translocation by the ClpXP degradation machine. *Molecular Cell*, 5 (4):639–648, 2000.

S. Klebe, H. Azzedine, A. Durr, P. Bastien, N. Bouslam, N. Elleuch, S. Forlani, C. Charon, M. Koenig, J. Melki, A. Brice, and G. Stevanin. Autosomal recessive spastic paraplegia (SPG30) with mild ataxia and sensory neuropathy maps to chromosome 2q37.3. *Brain*, 129(Pt 6):1456–1462, 2006.

D. E. Koshland, G. Némethy, and D. Filmer. Comparison of experimental binding data and theoretical models in proteins containing subunits. *Biochemical Journal*, 5(1):365–385, 1966.

M. Latterich and S. Patel. The 5AAA6 team: related 5ATPases6 with diverse functions. *Trends in Cell Biology*, 8(2):65–71, 1998.

C. J. Lawrence, R. K. Dawe, K. R. Christie, D. W. Cleveland, S. C. Dawson, S. A. Endow, L. S. Goldstein, H. V. Goodson, N. Hirokawa, J. Howard, R. L. Malmberg, J. R. McIntosh, H. Miki, T. J. Mitchison, Y. Okada, A. S. Reddy, W. M. Saxton, M. Schliwa, J. M. Scholey, R. D. Vale, C. E. Walczak, and L. Wordeman. A standardized kinesin nomenclature. *Journal of Cell Biology*, 167(1):19–22, 2004.

Y. Y. Li, E. Yeh, T. Hays, and K. Bloom. Disruption of mitotic spindle orientation in a yeast dynein mutant. *Proceedings of the National Academy of Sciences of the United States of America*, 90(21):10096–10100, 1993.

A. Lupas and J. Martin. AAA proteins. *Current Opinion in Structural Biology*, 12(6): 746–753, 2002.

D. Magde, E. L. Elson, and W. W. Webb. Thermodynamic Fluctuations in a Reaction System - Measurement by Fluorescence Correlation Spectroscopy. *Physical Review Letters*, 29(11):705–708, 1972.

D. Magde, E. L. Elson, and W. W. Webb. Fluorescence Correlation Spectroscopy. II. An Experimental Realization. *Biopolymers*, 13:29–61, 1974.

E. Mandelkow and E.-M. Mandelkow. Microtubules and microtubule-associated proteins. *Current Opinion in Cell Biology*, 7(1):72 – 81, 1995.

A. Mannan, J. Boehm, S. Sauter, A. Rauber, P. Byrne, J. Neesen, and W. Engel. Spastin, the most commonly mutated protein in hereditary spastic paraplegia interacts with Reticulon 1 an endoplasmic reticulum protein. *Neurogenetics*, 7(2):93–103, 2006.

A. Martin, T. A. Baker, and R. T. Sauer. Rebuilt AAA + motors reveal operating principles for ATP-fuelled machines. *Nature*, 437(7062):1115–1120, 2005.

A. Marx, J. Müller, E.-M. Mandelkow, A. HOENGER, and E. Mandelkow. Interaction of kinesin motors, microtubules, and MAPs. *Journal of Muscle Research & Cell Motility*, 27(2):125–137, 2006.

C. McDermott. Hereditary spastic paraparesis: a review of new developments. *Journal of Neurology, Neurosurgery & Psychiatry*, 69(2):150–160, 2000.

F. J. McNally and R. D. Vale. Identification of katanin, an ATPase that severs and disassembles stable microtubules. *Cell*, 75(3):419–429, 1993.

K. McNally, A. Audhya, K. Oegema, and F. J. McNally. Katanin controls mitotic and meiotic spindle length. *Journal of Cell Biology*, 175(6):881–891, 2006.

T. Mitchison and M. Kirschner. Dynamic instability of microtubule growth. *Nature*, 312 (5991):237–242, 1984.

A. Molon, S. Di Giovanni, Y. W. Chen, P. M. Clarkson, C. Angelini, E. Pegoraro, and E. P. Hoffman. Large-scale disruption of microtubule pathways in morphologically normal human spastin muscle. *Neurology*, 62(7):1097–1104, 2004.

J. Monod, J. P. Changeux, and F. Jacob. Allosteric proteins and cellular control systems. *Journal of Molecular Biology*, 6:306–329, 1963.

J. Monod, J. Wyman, and J. P. Changeux. On the nature of allosteric transitions: A plausible model. *Journal of Molecular Biology*, 12:88–118, 1965.

S. Nishikori, M. Esaki, K. Yamanaka, S. Sugimoto, and T. Ogura. Positive Cooperativity of the p97 AAA ATPase Is Critical for Essential Functions. *Journal of biological chemistry*, 286(18):15815–15820, 2011.

E. Nogales, S. G. Wolf, and K. H. Downing. Structure of the alpha beta tubulin dimer by electron crystallography [see comments] [published erratum appears in Nature 1998 May 14;393(6681):191]. *Nature*, 391(6663):199–203, 1998.

T. Ogura, S. W. Whiteheart, and A. J. Wilkinson. Conserved arginine residues implicated in ATP hydrolysis, nucleotide-sensing, and inter-subunit interactions in AAA and AAA+ ATPases. *Journal Of Structural Biology*, 146(1-2):106–112, 2004.

T. Pastinen. Genome-wide allele-specific analysis: insights into regulatory variation. *Nature Revieves Genetics*, 11(8):533–538, 2010.

L. Pauling. The Oxygen Equilibrium of Hemoglobin and Its Structural Interpretation. *Proceedings of the National Academy of Sciences U.S.A.*, 21(4):186–191, 1935.

E. P. Petrov and P. Schwille. Translational Diffusion in Lipid Membranes beyond the Saffman-Delbrück Approximation. *Biophysical Journal*, pages L41–L43, 2008.

T. Pirzer and T. Hugel. Atomic force microscopy spring constant determination in viscous liquids. *Review of Scientific Instruments*, 80(3):035110, 2009.

E. Reid. The hereditary spastic paraplegias. *Journal of Neurology*, 246(11):995–1003, 1999.

E. Reid, J. Connell, T. L. Edwards, S. Duley, S. E. Brown, and C. M. Sanderson. The hereditary spastic paraplegia protein spastin interacts with the ESCRT-III complex-associated endosomal protein CHMP1B. *Human molecular genetics*, 14(1):19–38, 2005.

S. Rice, A. W. Lin, D. Safer, C. L. Hart, N. Naber, B. O. Carragher, S. M. Cain, E. Pechatnikova, E. M. Wilson-Kubalek, M. Whittaker, E. Pate, R. Cooke, E. W. Taylor, R. Milligan, and R. D. Vale. A structural change in the kinesin motor protein that drives motility. *Nature*, 402(6763):778–784, 1999.

A. Roll-Mecak and F. J. McNally. Microtubule-severing enzymes. *Current Opinion in Cell Biology*, 22(1):96–103, 2010.

A. Roll-Mecak and R. D. Vale. Structural basis of microtubule severing by the hereditary spastic paraplegia protein spastin. *Nature*, 451(7176):363–367, 2008.

H. R. Saibil, W. A. Fenton, D. K. Clare, and A. L. Horwich. Structure and Allostery of the Chaperonin GroEL. *Journal of Molecular Biology*, 425(9):1476–1487, 2013.

S. Salinas, R. E. Carazo-Salas, C. Proukakis, J. M. Cooper, A. E. Weston, G. Schiavo, and T. T. Warner. Human spastin has multiple microtubule-related functions. *Journal of Neurochemistry*, 95(5):1411–1420, 2005.

S. Salinas, R. E. Carazo-Salas, C. Proukakis, G. Schiavo, and T. T. Warner. Spastin and microtubules: Functions in health and disease. *Journal of Neuroscience Research*, 2007.

C. M. Sanderson, J. W. Connell, T. L. Edwards, N. A. Bright, S. Duley, A. Thompson, J. P. Luzio, and E. Reid. Spastin and atlastin, two proteins mutated in autosomal-dominant hereditary spastic paraplegia, are binding partners. *Human Molecular Genetics*, 15(2): 307–318, 2006.

T. A. Schroer, E. R. Steuer, and M. P. Sheetz. Cytoplasmic dynein is a minus end-directed motor for membranous organelles. *Cell*, 56(6):937–946, 1989.

P. Schwille and E. Haustein. Fluorescence Correlation Spectroscopy - An Introduction to its Concepts and Applications. Technical report, 2006.

D. M. Smith, N. Benaroudj, and A. Goldberg. Proteasomes and their associated ATPases: a destructive combination. *Journal of Structural Biology*, 156(1):72–83, 2006.

D. M. Smith, H. Fraga, C. Reis, G. Kafri, and A. L. Goldberg. ATP Binds to Proteasomal ATPases in Pairs with Distinct Functional Effects, Implying an Ordered Reaction Cycle. *Cell*, 144(4):526–538, 2011.

G. R. Smith, C.-M. Bruno, Z. Xiaodong, and A. B. Paul. A link between sequence conservation and domain motion within the AAA+ family. *Journal of Structural Biology*, 146 (1–2):189–204, 2004.

J. Snider, G. Thibault, and W. A. Houry. The AAA+ superfamily of functionally diverse proteins. *Genome Biology*, 9(4):216, 2008.

J. M. Solowska, G. Morfini, A. Falnikar, B. T. Himes, S. T. Brady, D. Huang, and P. W. Baas. Quantitative and Functional Analyses of Spastin in the Nervous System: Implications for Hereditary Spastic Paraplegia. *Journal of Neuroscience*, 28(9):2147–2157, 2008.

V. Stoppin-Mellet, J. Gaillard, and M. Vantard. Functional evidence for in vitro microtubule severing by the plant katanin homologue. *Biochemical Journal*, 365(Pt 2): 337–342, 2002.

M. Stotz, O. Mueller-Cajar, S. Ciniawsky, P. Wendler, F. U. Hartl, A. Bracher, and M. Hayer-Hartl. Structure of green-type Rubisco activase from tobacco. *Nature Structural & Molecular Biology*, 18(12):1366–1370, 2011.

A. Strümpell. Beiträge zur Pathologie des Rückenmarks. *Archiv für Psychiatrie und Nervenkrankheiten*, 10(3):676–717, 1880.

I. K. Svenson, A. E. Ashley-Koch, P. C. Gaskell, T. J. Riney, W. J. K. Cumming, H. M. Kingston, E. L. Hogan, R.-M. N. Boustany, J. M. Vance, M. A. Nance, M. A. Pericak-Vance, and D. A. Marchuk. Identification and Expression Analysis of Spastin Gene Mutations in Hereditary Spastic Paraplegia. *The American Journal of Human Genetics*, 68(5):1077–1085, 2001.

K. Svoboda and S. M. Block. Force and velocity measured for single kinesin molecules. *Cell*, 77(5):773–784, 1994.

J. Timmer. Von der Mathematischen Biologie zur Systembiologie, Script zur Vorlesung, 2012.

C. Ungermann, B. J. Nichols, H. R. Pelham, and W. Wickner. A vacuolar v-t-SNARE complex, the predominant form in vivo and on isolated vacuoles, is disassembled and activated for docking and fusion. *Journal of Cell Biology*, 140(1):61–69, 1998.

R. D. Vale. AAA Proteins: Lords of the Ring. *Journal of Cell Biology*, 150(1):13F–20, 2000.

D. Voet and J. G. Voet. *Biochemistry*. Wiley, 2010.

A. von Massow, E. M. Mandelkow, and E. Mandelkow. Interaction between kinesin, microtubules, and microtubule-associated protein 2. *Cell Motility and the Cytoskeleton*, 14 (4):562–571, 1989.

M. Vukajlovic. *Regulation of the subunit assembly and the catalytic activity in heteromeric kinesin-2 from Caenorhabditis elegans.* PhD thesis, Ludwig Maximillians Universität München, 2012.

N. D. Werbeck, S. Schlee, and J. Reinstein. Coupling and Dynamics of Subunits in the Hexameric AAA+ Chaperone ClpB. *Journal of Molecular Biology*, 378(1):178–190, 2008.

N. D. Werbeck, J. N. Kellner, T. R. M. Barends, and J. Reinstein. Nucleotide Binding and Allosteric Modulation of the Second AAA+ Domain of ClpB Probed by Transient Kinetic Studies. *Biochemistry*, 48(30):7240–7250, 2009.

S. R. White, K. J. Evans, J. Lary, J. L. Cole, and B. Lauring. Recognition of C-terminal amino acids in tubulin by pore loops in Spastin is important for microtubule severing. *Journal of Cell Biology*, 176(7):995–1005, 2007.

S. R. White and B. Lauring. AAA+ ATPases: Achieving Diversity of Function with Conserved Machinery. *Traffic*, 8(12):1657–1667, 2007.

S. W. Whiteheart and E. A. Matveeva. Multiple binding proteins suggest diverse functions for the N-ethylmaleimide sensitive factor. *Journal of Structural Biology*, 146(1–2):32–43, 2004.

O. Yifrach and A. Horovitz. Nested cooperativity in the ATPase activity of the oligomeric chaperonin GroEL. *Biochemistry*, 34(16):5303–5308, 1995.

W. Yu, L. Qiang, J. M. Solowska, A. Karabay, S. Korulu, and P. W. Baas. The Microtubule-severing Proteins Spastin and Katanin Participate Differently in the Formation of Axonal Branches. *Molecular Biology of the Cell*, 19(4):1485–1498, 2008.

R. Yvinec, M. R. D'Orsogna, and T. Chou. First passage times in homogeneous nucleation and self-assembly. *Journal of Chemical Physics*, 137(24):244107, 2012.

X. Zhang and D. B. Wigley. The 'glutamate switch' provides a link between ATPase activity and ligand binding in AAA+ proteins. *Nature Structural & Molecular Biology*, 15(11):1223–1227, 2008.

M. Zolkiewski. A camel passes through the eye of a needle: protein unfolding activity of Clp ATPases. *Molecular Microbiology*, 61(5):1094–1100, 2006.

Danksagung

Hiermit möchte ich mich bei allen denjenigen bedanken, die direkt oder indirekt an dieser Disseratation mitgeholfen haben! Insbesondere gilt mein Dank:

Günther Woehlke, für die Möglichkeit, dieses interessante und vielseitige Thema zu untersuchen, sowie für hilfreiche und interessanten Diskussionen;

Thorsten Hugel, für den Posten des Zweitgutachters;

Matthias Rief, für die Bereitstellung eines hervorragend ausgestatteten Labors;

Monika Rusp, Daniela Scheikl, Karin Vogt und Gabriele Chmel, für die Hilfe und Arbeit im Laboralltag: die Engel des Labors;

Sandra Kienle, für die gemeinsammen Messungen am AFM;

Tobias Stögbauer und Tobias Preiß, für die Einarbeitung und Beantwortung sämtliche Fragen über FCS;

meine Kollegen, für eine schöne Zeit am Lehrstuhl und die ganzen leckeren Kuchen; insbesondere Anja Gieseke für die Beantwortung sämtlicher Fragen, die Diskussionen, das Zuhören sowie viele Stunden im Studio; Fabian Ziegler und Johannes Stigler für Hilfe bezüglich IGOR; Felix Keber und Gabriel Zoldak für aufschlussreiche Diskussionen; Daniela Bauer, Martina Lindauer und Joanna Deek für ihren Beistand und lustige Abende

meine Freunde, für Spannung, Spaß und Schokolade;

meine Familie, für ihre Unterstützung und Ratschläge in jeder Lebenslage;

Tobias Stögbauer, für den grenzlosen Optimismus und Zusammenhalt in guten wie in schlechten Tagen.

Lebenslauf

Doan Tuong-Van Le

20.04.1983	Geburt in München
1989 – 1993	Besuch der Volkschule (Grundschule) München
1993 – 2002	Besuch des Institutes der englischen Fräulein,
	Maria Ward Gymnasium in Nymphenburg, München
01.10.2002 – 30.05.2008	Studiengang Diplomphysik an der LMU
25.01.2006 – 31.07.2006	ERASMUS Auslandssemester an der Universität Nottingham
30.04.2007-30.05.2008	Diplomarbeit am Max-Planck-Institut
	für extraterrestrische Physik (MPE)
seit 16.02.2009	Promotion am Lehrstuhl E22 bei PD Dr. Günther Woehlke